Development of near infrared optical tomography for thyroid cancer diagnosis

Development of near infrared optical tomography for thyroid cancer diagnosis

Tetsuya Mimura

Cooperative Major in Medical Photonics,
Shizuoka University
&
Hamamatsu University School of Medicine

March 2021

Abstract

The incidence of thyroid cancer has been increasing worldwide during the past decades. Thyroid cancer is usually diagnosed by ultrasound imaging and fine-needle aspiration biopsy. However, diagnosis of follicular thyroid carcinoma (FTC), one type of thyroid cancers that can mutate into more aggressive variants, is difficult even after total thyroidectomy. Near infrared optical tomography (NIROT) is a potential approach to diagnosis of FTC because it can measure tumor hypoxia. Since, however, anatomical features of the human neck are complex, image reconstruction of the thyroid is challenging: the thyroid is located in a narrow region between the skin and trachea. In this study, we attempted to get around this issue by extracting the minimum volume of the human neck that is required for the image reconstruction, with the void region of the trachea excluded, and creating a finite element grid. First, we evaluated our image reconstruction algorithm in phantom experiments. And then, conducting time-domain optical measurements of a healthy human neck, we reconstructed the spatial distribution of absorption coefficients and three-dimensional tissue oxygen saturation maps of the whole of the thyroid.

This study was approved by the ethical committee of Hamamatsu University School of Medicine (No. 15-082). A multichannel time-domain measurement instrument (TRS-80, Hamamatsu Photonics K.K., Hamamatsu, Japan) was used to measure the phantom and the human subject. TRS-80 emits the ultrafast pulsed near infrared lights at 763 nm, 801 nm, and 836 nm, and detects the transmitted lights through a measuring object that are transferred to the time-correlated single photon counting unit through eight high-speed photomultipliers.

The polyurethan-based rectangular phantom (40 × 40 × 70 mm) including a cylindrical absorber with a diameter of 5 mm and a height of 70 mm was used for the evaluation of the algorithm. The subject was a healthy woman who was informed of the aim and procedures of this study. To confirm the tracheal and thyroid positions, a cervical magnetic resonance imaging scan was performed. The magnetic resonance (MR) images were also used to make an optical fiber holder. A total of 15 holes in the holder were arranged at an interval of 1.5 cm and seven source and eight detector fibers were inserted into the holes alternately so that the whole thyroid was illuminated. Forty-nine time-of-flight distributions of photons with the sufficient signal to noise ratio were used for the image reconstruction. Using the MR images, we created the grids with the void region of the trachea excluded. As a comparison, we made another grid by disregarding the presence of the trachea. We obtained the tomographic images of the absorption coefficients by minimizing the least square method with Tikhonov regularization by the nonlinear conjugate gradient method. During the iteration process, the reduced scattering coefficient value was fixed.

In the phantom experiment, we confirmed that the high absorption region was successfully reconstructed. Then, we performed the image reconstruction of the human neck and superimposed these images on the MR images. High absorption regions corresponding approximately to the thyroid were reconstructed with the grid with excluding the trachea, although the position slightly shifted to the skin. We calculated tissue oxygen saturation from the absorption coefficient values at the three wavelengths. The tissue oxygen saturation of the thyroid was around 90%, while that in the background tissues, mainly muscles, was around 65%. In contrast, with the grid that disregards the presence of the trachea, the shape of the thyroid was not correctly reconstructed, although the existence of the thyroid may be read from the reconstructed images.

This is the first study reporting the reconstruction of the spatial distribution of absorption coefficients and tissue oxygen saturation in the human whole thyroid with NIROT. It has been shown that the whole shape of the thyroid can be reconstructed if the grid for the

calculations excludes the trachea void region. However, it is expected that reconstructed images will be improved if the reentrant light, which propagates through the trachea, is taken into account. In this study, the thyroid was reconstructed at a position closer to the skin than its actual position. This is attributable to the fact that we did not employ the spatially variant regularization despite decreases in measurement sensitivity along the depth direction. The values of the reconstructed absorption coefficients were much larger than the background values. The quantitative accuracy of the present study is still insufficient because the reduced scattering coefficient was not updated during the iterations. However, tissue oxygen saturation maps indicate that the thyroid is distinguishable from the background tissues. The present study has the three main limitations described above, but it has paved the way to functional optical imaging of the human thyroid.

This study presents three-dimensional *in situ* imaging of absorption coefficient and tissue oxygen saturation in the human thyroid by NIROT. The key ingredient is the use of a trachea-tissue boundary grid. It can be expected that NIROT has the potential to visualize the tissue hypoxia of the thyroid cancer.

Table of Contents

List of Figures

List of Tables

List of Acronyms

2D 2-dimensional.

3D 3-dimensional.

CAD Computer-aided design.

CCA Common carotid artery.

CT Computed tomography.

cyt. ox. Cytochrome c oxidase.

D Depth.

deoxy-Hb Deoxygenated hemoglobin.

DICOM Digital imaging and communications in medicine.

DOS Diffuse optical spectroscopy.

ES Esophagus.

FDG Fluorodeoxyglucose.

FEM Finite element method.

FTC Follicular thyroid carcinoma.

H Height.

Hb Hemoglobin.

HIF Hypoxia-inducible factor.

IJV Internal jugular vein.

IRF Instrumental response function.

LHS Left-hand side.

LPS Left, Posterior, Superior.

MMP Metalloproteinase.

MR Magnetic resonance.

MRI Magnetic resonance imaging.

MU Muscle.

NA Numerical aperture.

NIROT Near infrared optical tomography.

oxy-Hb Oxygenated hemoglobin.

PAI Photoacoustic imaging.

PET Positron emission tomography.

PMT Photomultiplier tube.

PTC Papillary thyroid carcinoma.

RHS Right-hand side.

SEER Surveillance epidemiology and end results.

SK Skin.

SNR Signal-to-noise ratio.

STL Standard triangulated language.

StO_2 Tissue oxygen saturation.

TD-DE Time-dependent diffusion equation.

TH Thyroid.

TOF Time-of-flight.

TR Trachea.

W Width.

Chapter 1

Introduction

The incidence of thyroid cancer has been increasing in many parts of the world during the past decades although thyroid cancer is still among the less common cancers [1], [2]. The etiology of the increasing incidence is not established. An analysis of data from the Surveillance Epidemiology and End Results (SEER) database has indicated that the increase was due to improved detection and not to any rise in occurrence [3]. However, the worldwide increase is hardly explained simply by noting earlier discovery [1] and there is increasing interest in the diagnosis and treatment of thyroid cancers. There are four main types of thyroid cancer. Papillary thyroid carcinoma (PTC) and follicular thyroid carcinoma (FTC) are categorized among the differentiated thyroid cancers which are not usually aggressive. The PTC is by far the most common form and is usually slow-growing, but can mutate into more aggressive variants. Thyroid cancer is often diagnosed after nodules in the thyroid are discovered as a lump in the neck or by routine image examination, such as an ultrasound scan performed on the carotid arteries [4].

Other than FTC, which is more aggressive than PTC, thyroid cancers can be diagnosed by ultrasound scanning and fineneedle aspiration biopsies. Since the FTC lacks the nuclear atypia seen in PTC and is encapsulated like a benign tumor (i.e., follicular adenoma), a diagnosis of FTC is based on histologic demonstration of capsular and/or vascular invasion

after a total thyroidectomy [5]. However, it is difficult to diagnose capsular invasion because of a lack of consensus on the histologic interpretation of findings: some argue that penetration into the tumor capsule by lesional cells is indicative of malignancy, while others argue that infiltration of tumor cells into the surrounding thyroid parenchyma through the entire thickness of the capsule is capsular invasion [5], [6]. Thus, non-invasive and more sensitive diagnostic approaches to FTC would be helpful.

Using X-ray CT (computed tomography) and MRI (magnetic resonance imaging) is common diagnostic imaging techniques. Since, however, the ability to characterize thyroid nodules and detect small carcinomas is inferior to ultrasound scanning, X-ray CT and MRI are mainly used to evaluate extrathyroidal carcinoma extensions [7]. With 18FDG PET/CT (fluorine-18 fluorodeoxyglucose positron emission tomography/ computed tomography) it is possible to detect solid tumors, but not thyroid cancers as there is uptake of 18FDG in chronic thyroiditis [8]. Thyroid cancer is accompanied by functional changes, including angiogenesis [9] and its related molecular responses [10], [11], as well as structural changes. Optical imaging with near infrared light, including photoacoustic imaging (PAI), diffuse optical spectroscopy (DOS) and near infrared optical tomography (NIROT), can non-invasively evaluate hemodynamic and metabolic changes associated with thyroid cancer, and offers the potential for a diagnostic approach to FTC.

To date, PAI has been applied to the detection of angiogenesis in thyroid cancer. Yang et al. demonstrated that PAI detected small blood vessels that color Doppler flow imaging could not, whereas it has also been reported that acoustic reflection at large impedance-mismatched boundaries at the trachea caused artifacts in PAI images [12]. This approach could be useful in diagnosing PTC but not for FTC because FTC is not accompanied by angiogenesis [9]. It has also been suggested that two members of the matrix metalloproteinase family (MMP-2, MMP-9) are biomarkers for FTC [10]. Using an MMP-activatable photoacoustic probe, Levi et al. demonstrated that molecular PAI offers great promise for the diagnosis of FTC, but clinical application appears difficult [13]. Lindner et al. em-

ployed custom time-resolved spectroscopy and a diffuse correlation spectroscopic system to the measurements of total hemoglobin (Hb) concentrations, tissue oxygen saturation (StO_2), and blood flow indexes in the thyroid and also in muscles [14]. Several studies have suggested that hypoxia contributes to the progression of thyroid cancer especially via the hypoxia-inducible factor-1α (HIF-1α) [11], [15], and a lower StO_2 has the potential to be an indicator of malignancy. However, with the Lindner et al. DOS system it is difficult to measure the thyroid separately from muscles, while it would be possible with NIROT.

NIROT is an imaging modality that reconstructs absorption (μ_a) and reduced scattering (μ_s') coefficients from boundary measurements [16]. From the reconstructed μ_a, the Hb concentration and StO_2 can be calculated. The μ_s' reflects morphological and structural changes, such as cell swelling caused by cell injuries, whereas it is unlikely that μ_s' is altered by capsular and/or vascular invasion by FTC. Cytochrome c oxidase (cyt. ox.) in mitochondria is also a biological chromophore that can be measured by NIROT. The redox state of cyt. ox. is dependent on the intracellular oxygen concentration and its reduction occurs under severe hypoxic conditions [17]. From this, it may be expected that NIROT can detect FTC by measuring the StO_2 and cyt. ox. in the thyroid.

To the best of our knowledge, NIROT images of the human thyroid have not been reported except for those in our simulation study [18]. This may be attributed to the fact that the human neck is a heterogeneous medium; it is composed of the trachea, the thyroid, the vertebrae, large blood vessels, muscles, adipose tissue, and others. The thyroid is located in a narrow region between the skin and trachea, and NIROT image interpretation of the thyroid is not straightforward. In this study, we attempted to get around this issue by extracting the minimum volume of the human neck that is required for the image reconstruction, with the void region of the trachea excluded, and creating a finite element grid. Toward a clinical study, we conducted NIROT measurements of a healthy human thyroid and reconstructed the spatial distribution of μ_a to create a 3-dimensional (3D) image of the whole of the thyroid. Then, using the μ_a values at three wavelengths, StO_2 maps were created.

Chapter 2

Methods

2.1 Time-domain near-infrared spectroscopy system

2.1.1 TRS-80 system

A multichannel time-domain measurement instrument (TRS-80, Hamamatsu Photonics K.K., Hamamatsu, Japan) was used to measure the human neck (Figure 2.1). This instrument was developed from TRS-20SH, which has a single channel. See [19] for details of the TRS-20SH. Briefly, the TRS-80 consists of three pulsed laser diodes at wavelengths of 763 nm, 801 nm, and 836 nm (the pulse width is less than 100 ps for each wavelength) with a repetition rate of 5 MHz. All laser diodes are pigtailed and coupled into one optical fiber by the fiber coupler. The fiber is coupled to eight source fibers (core diameter 200 μm, (numerical aperture (NA) = 0.25) via the optical switch (switching time, about 1 s) and the tip of each source fiber is attached to a measurement target (average power 200 μW). Transmitted light through the target is detected by eight fiber bundles (diameter 3 mm, NA = 0.29) and transferred to eight high-speed photomultiplier tubes (PMTs) (H7422P-50 SEL, Hamamatsu Photonics K.K., Hamamatsu, Japan) for single photon detection. The electrical output of a PMT is transmitted to the time correlated single photon counting unit. It takes

1 s to obtain the time-of-flight (TOF) distribution of photons (time step size 10 ps) in the time range from 0 to 10.24 ns for each wavelength. The TOF distributions with adequate signal-to-noise ratios (SNRs) are acquired by summation of signals for 10 s. The criterion of adequate SNR is that the maximum count of TOF distribution is greater than 2000 and the dark count is less than 10. The average of the full width half maximum of the instrumental response function (IRF) is 390 ps. The TRS-80 is portable and available for use at the bedside. In this study, the measurement of the neck was conducted by a TRS-80 at the bedside while the subject lay on the bed.

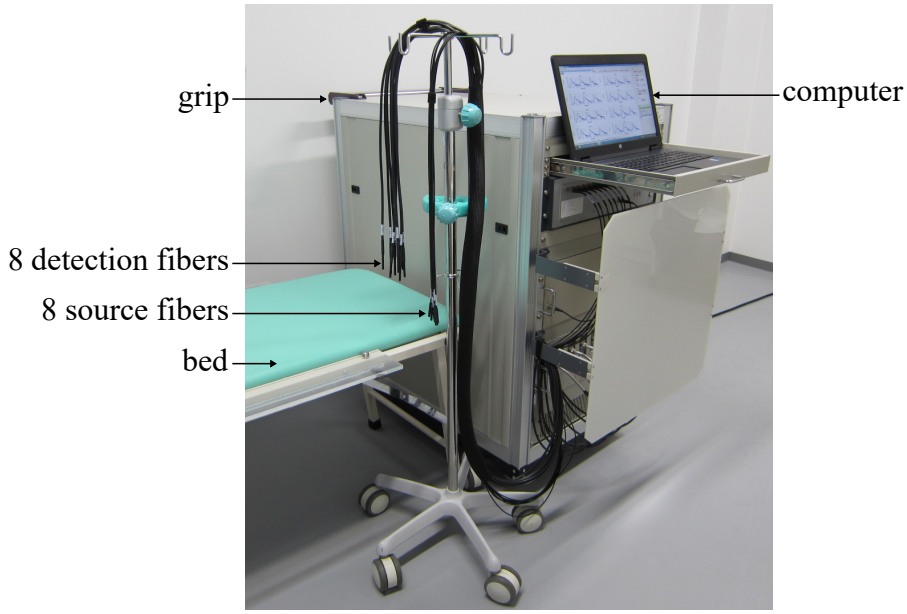

Figure 2.1. Photograph of TRS-80, which performs the optical measurement at the bedside. The dimensions are 0.57 (W) × 0.81 (D) × 1.1 (H) m. TRS-80 has eight source fibers, eight detection fibers, a computer, and a grip.

2.1.2 Instrumental response function

We measured the IRFs in all combinations of the source and detection fibers by using an 8ch IRF module which enables us to obtain eight IRFs for one source fiber simultaneously. The 8ch IRF module (10 (W) × 7.6 (D) × 10 cm (H)) has one source fiber port on one side and eight detection fiber ports on the other side (Figure 2.2). A thin diffuser is placed inside each port. The detection fiber ports are arranged at regular intervals on the circumference

of a circle (a diameter of 30 mm) of which center is opposite to the source fiber port. The space between the source fiber and the detection fibers is filled with air, and the distance between every source-detection pair is 7.5 cm. Figures 2.3-2.5 show the IRF. The average of the full width half maximum of the IRF is 390 ps.

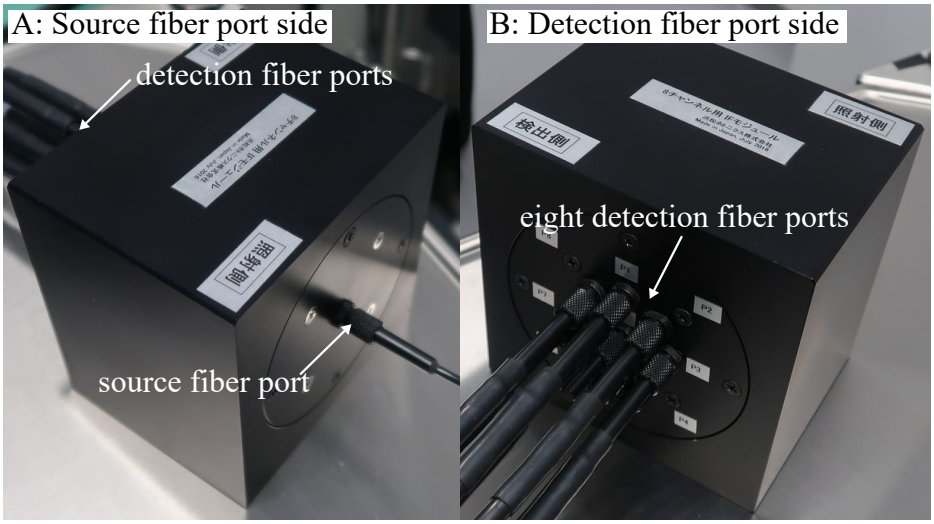

Figure 2.2. Photograph of 8ch instrumental response function (IRF) module in (A): source fiber port side, (B): detection fiber port side.

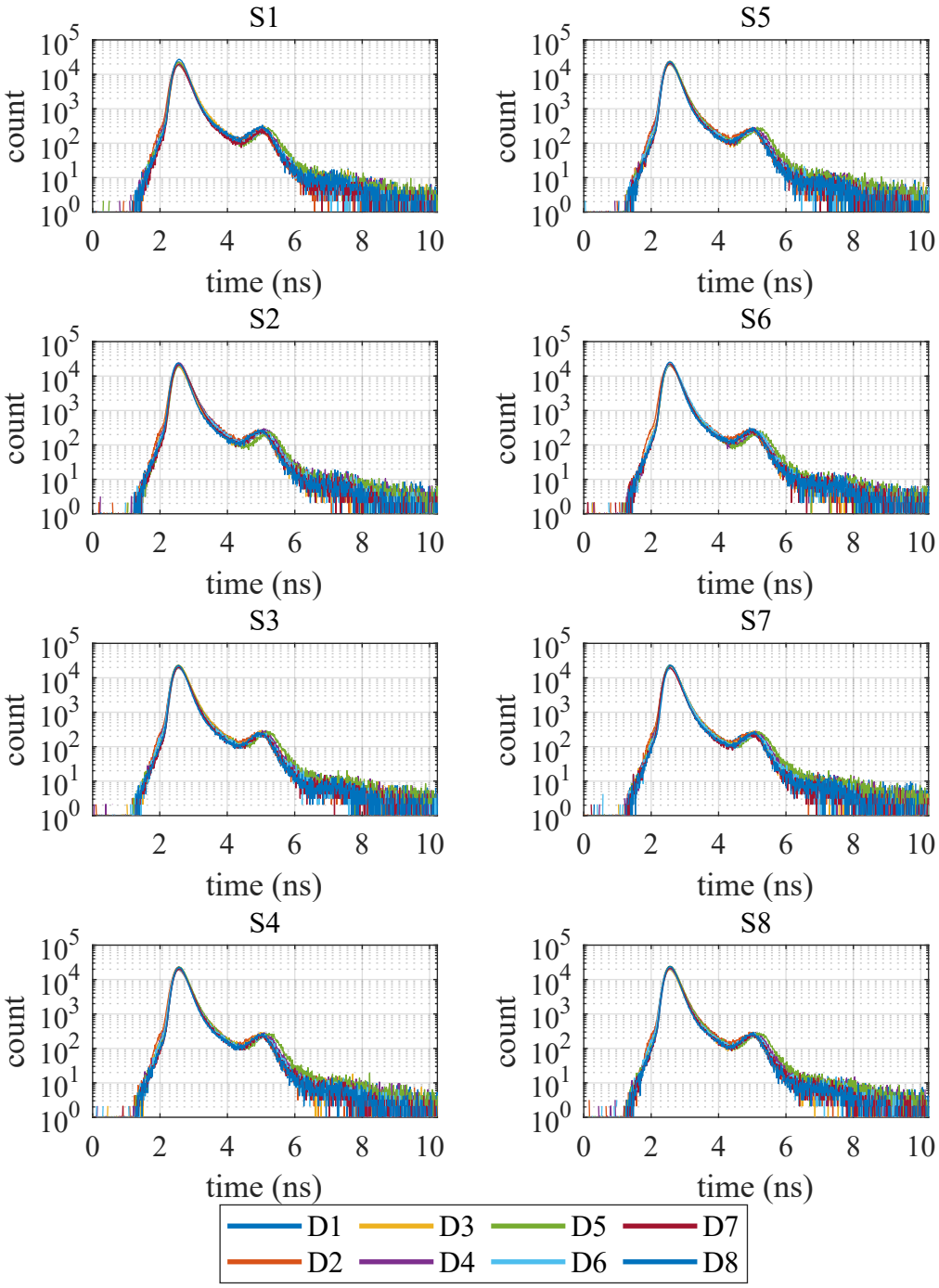

Figure 2.3. Instrumental response functions at 763 nm of TRS-80. Vertical axis denotes photon-count number along logarithmic scale. S# denotes the number of the source fiber. D# denotes the number of the detection fiber.

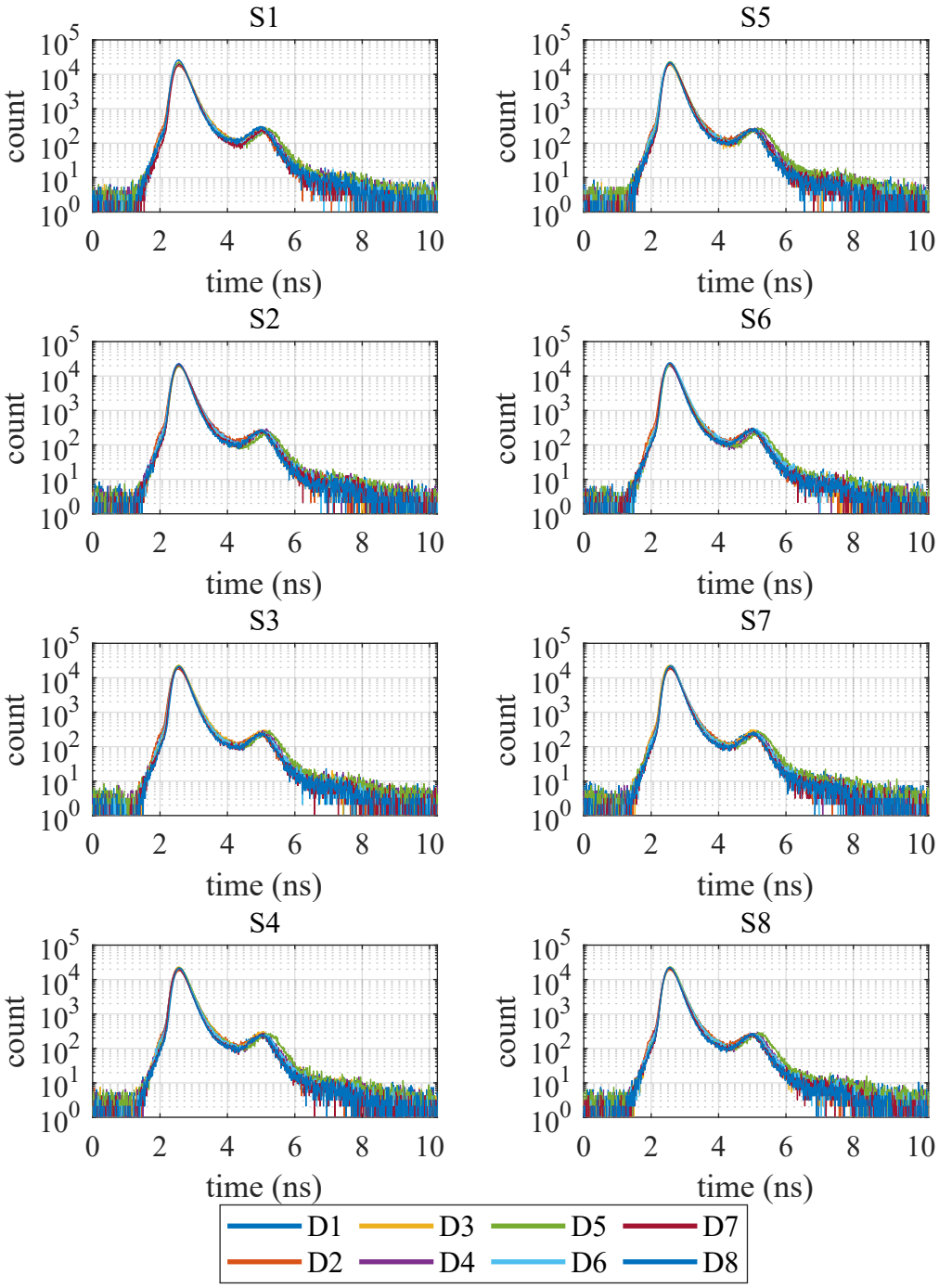

Figure 2.4. Instrumental response functions at 801 nm of TRS-80. Vertical axis denotes photon-count number along logarithmic scale. S# denotes the number of the source fiber. D# denotes the number of the detection fiber.

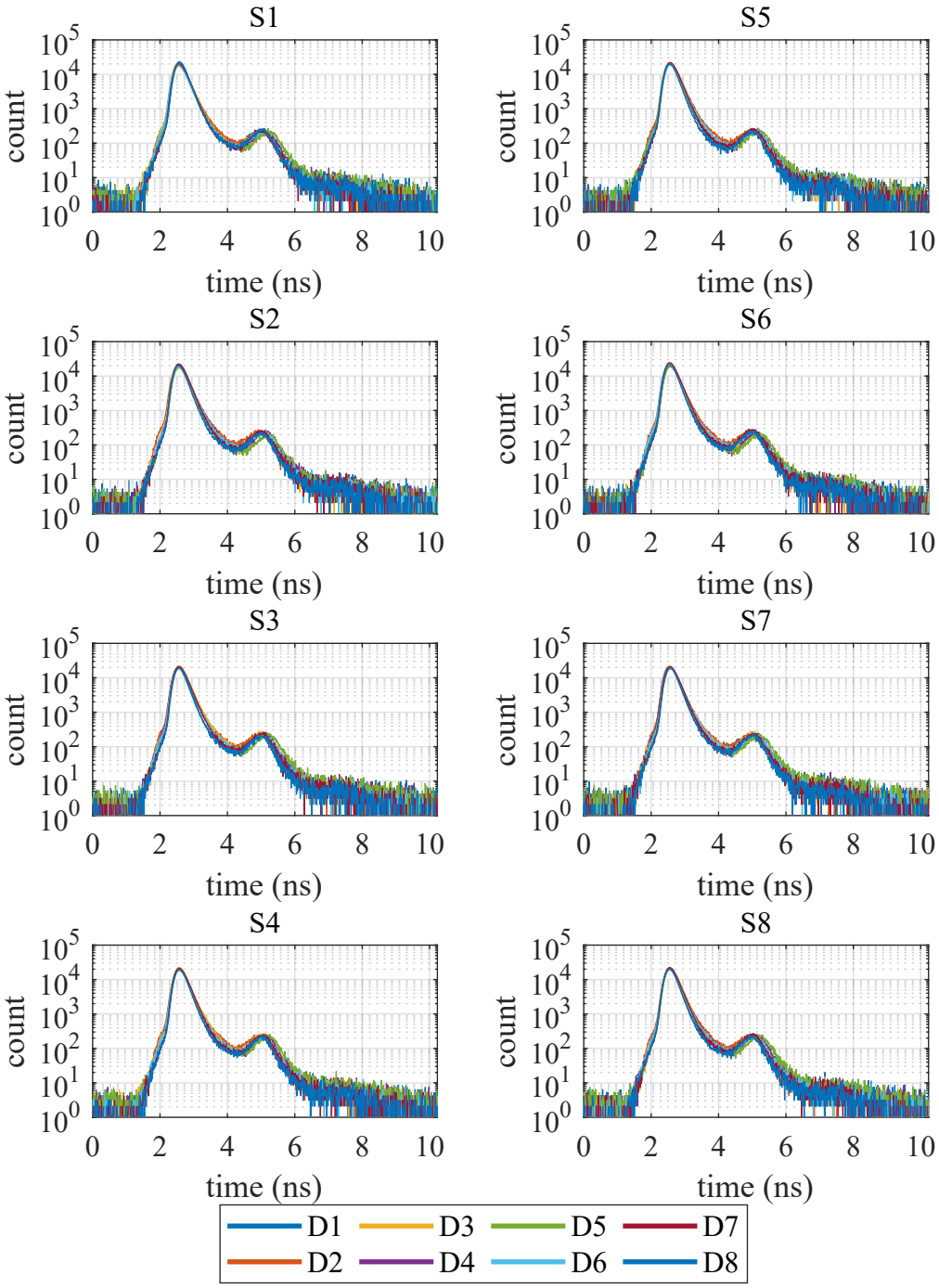

Figure 2.5. Instrumental response functions at 836 nm of TRS-80. Vertical axis denotes photon-count number along logarithmic scale. S# denotes the number of the source fiber. D# denotes the number of the detection fiber.

2.2 Light transport model in tissue

2.2.1 The time-dependent diffusion equation

In this study, the light transport in the tissue is described by the time-dependent diffusion equation (TD-DE), which is the diffusion approximation of the radiative transport equation. Appendix A.2–A.6 shows the detail. The TD-DE form is

$$\left[\frac{1}{c}\frac{\partial}{\partial t} - \nabla \cdot \kappa(\mathbf{r})\nabla + \mu_{\mathrm{a}}(\mathbf{r})\right]\phi_i(\mathbf{r},t) = q_i(\mathbf{r},t), \qquad \mathbf{r} \in \Omega, 0 < t < T, \tag{2.1}$$

with Robin boundary condition (derived in Appendix A.7)

$$\phi_i(\mathbf{r},t) + \zeta(c)\,\kappa(\mathbf{r})\,\hat{\mathbf{n}} \cdot \nabla\phi_i(\mathbf{r},t) = 0, \qquad \mathbf{r} \in \partial\Omega, 0 < t < T, \tag{2.2}$$

which describes the change in the fluence rate ϕ at time t and position vector $\mathbf{r}$ within a domain Ω, bounded by a surface $\partial\Omega$. Here, T is the maximum time, $c = c_0/n$ is the speed of light in the medium with refractive index n, and c_0 is the speed of light in a vacuum. μ_{a} and μ'_{s} are the absorption and reduced scattering coefficients (Appendix A.1 shows the detail.), respectively, and $\kappa(\mathbf{r}) = \left\{3\left[\mu_{\mathrm{a}}(\mathbf{r}) + \mu'_{\mathrm{s}}(\mathbf{r})\right]\right\}^{-1}$ is the diffusion coefficient; ζ is refractive-index mismatch parameter at the surface $\partial\Omega$ (Appendix A.7 shows the detail.); $q_i(\mathbf{r},t) = \delta(\mathbf{r} - \mathbf{r}_{\mathrm{S}i})\,\delta(t)$ is the ith isotropic source term at source position $\mathbf{r}_{\mathrm{S}i} \in \partial\Omega, (i = 1, \cdots, N_{\mathrm{S}})$; $\hat{\mathbf{n}}$ is the outer normal vector of $\partial\Omega$. The measured quantity is the flux $\Gamma_{i,j}(t)$ at the detection position $\mathbf{r}_{\mathrm{D}j} \in \partial\Omega, (j = 1, \cdots, N_{\mathrm{D}})$. The relation between ϕ and Γ is given by Fick's law (Appendix A.8 shows the detail.),

$$\Gamma_{i,j}(t) = -\kappa\left(\mathbf{r}_{\mathrm{D}j}\right)\hat{\mathbf{n}}\left(\mathbf{r}_{\mathrm{D}j}\right) \cdot \nabla\phi_i\left(\mathbf{r}_{\mathrm{D}j}, t\right). \tag{2.3}$$

2.2.2 Normalized first-order moment of the time-dependent diffusion equation

To solve inverse problem in Section 2.3, we used the normalized first-order moment of the flux

$$\begin{aligned} g_{i,j} &= \frac{\int_0^\infty t\Gamma_{i,j}(t)\,dt}{\int_0^\infty \Gamma_{i,j}(t)\,dt}, \\ &= \frac{-c\kappa\left(\mathbf{r}_{\mathrm{D}j}\right)\hat{\mathbf{n}}\left(\mathbf{r}_{\mathrm{D}j}\right)\cdot\nabla M_i}{-c\kappa\left(\mathbf{r}_{\mathrm{D}j}\right)\hat{\mathbf{n}}\left(\mathbf{r}_{\mathrm{D}j}\right)\cdot\nabla E_i}, \end{aligned} \tag{2.4}$$

where

$$M_i = \int_0^\infty t\phi_i(\mathbf{r},t)\,dt, \tag{2.5}$$

$$E_i = \int_0^\infty \phi_i(\mathbf{r},t)\,dt, \tag{2.6}$$

to remove unknown constants in the measured TOF distribution. It takes a great deal of computational time to solve Equation (2.1), and as a result we obtained $g_{i,j}$ by solutions of two time-independent diffusion equations [20]. One is the zeroth moment of TD-DE, which is obtained by substituting Equation (2.6) for the time integral of Equation (2.1), and the form is

$$\begin{cases} -\nabla\cdot\kappa(\mathbf{r})\nabla E_i(\mathbf{r}) + \mu_{\mathrm{a}}(\mathbf{r})E_i(\mathbf{r}) = \delta(\mathbf{r}-\mathbf{r}_{\mathrm{S}i}), & \mathbf{r}\in\Omega, \\ E_i(\mathbf{r}) + \zeta(c)\kappa(\mathbf{r})\hat{\mathbf{n}}\cdot\nabla E_i(\mathbf{r}) = 0, & \mathbf{r}\in\partial\Omega. \end{cases} \tag{2.7}$$

The other is the first moment of TD-DE, which is obtained by substituting Equation (2.5) for the time integral of Equation (2.1) multiplied by time, and the form is

$$\begin{cases} -\nabla\cdot\kappa(\mathbf{r})\nabla M_i(\mathbf{r}) + \mu_{\mathrm{a}}(\mathbf{r})M_i(\mathbf{r}) = E_i(\mathbf{r}), & \mathbf{r}\in\Omega, \\ M_i(\mathbf{r}) + \zeta(c)\kappa(\mathbf{r})\hat{\mathbf{n}}\cdot\nabla M_i(\mathbf{r}) = 0, & \mathbf{r}\in\partial\Omega. \end{cases} \tag{2.8}$$

2.2.3 Finite element method

To find the optimum solution of the time-independent diffusion equation, we used the finite element method (FEM). With $\phi_i^{\mathrm{h}}(\mathbf{r},t)$ as the solution to Equation (2.1)

$$\phi_i(\mathbf{r},t) \approx \phi_i^{\mathrm{h}}(\mathbf{r},t) = \sum_{l=1}^{N_{\mathrm{N}}} \Phi_{l,i}(t)\, u_l(\mathbf{r}), \tag{2.9}$$

where $u_l(\mathbf{r}), (l = 1, \cdots, N_{\mathrm{N}})$ is the basis function and N_{N} is the number of nodes in the grid. We introduce a vector $\mathbf{\Phi}_i(t) = (\cdots \Phi_{l,i}(t) \cdots)^T$ of nodal coefficients. To discretize the TD-DE in Equation (2.1), we used a Galerkin approach [20]. The form is

$$\left[\frac{\partial}{\partial t} B + \zeta(c)\, A + K(\kappa) + C(\mu_{\mathrm{a}})\right] \mathbf{\Phi}_i(t) = \mathbf{q}_i, \tag{2.10}$$

where the individual integrals are given by

$$\begin{aligned}
B_{m,n} &= \frac{1}{c}\int_{\Omega} u_m(\mathbf{r})\, u_n(\mathbf{r})\, d\mathbf{r},\\
A_{m,n} &= \int_{\partial\Omega} u_m(\mathbf{r})\, u_n(\mathbf{r})\, d\mathbf{r},\\
K(\kappa)_{m,n} &= \int_{\Omega} \kappa^{\mathrm{h}}(\mathbf{r})\, \nabla u_m(\mathbf{r}) \cdot \nabla u_n(\mathbf{r})\, d\mathbf{r},\\
C(\mu_{\mathrm{a}})_{m,n} &= \int_{\Omega} \mu_{\mathrm{a}}^{\mathrm{h}}(\mathbf{r})\, u_m(\mathbf{r})\, u_n(\mathbf{r})\, d\mathbf{r},\\
\{q_i\}_m &= \int_{\Omega} u_m(\mathbf{r})\, \delta(\mathbf{r}-\mathbf{r}_i)\, d\mathbf{r}.
\end{aligned} \tag{2.11}$$

The optical properties can be expressed as

$$\mu_{\mathrm{a}}^{\mathrm{h}}(\mathbf{r}) = \sum_{l=1}^{N_{\mathrm{N}}} \mu_l u_l(\mathbf{r}), \tag{2.12}$$

$$\kappa^{\mathrm{h}}(\mathbf{r}) = \sum_{l=1}^{N_{\mathrm{N}}} \mu_{l+N_{\mathrm{N}}} u_l(\mathbf{r}), \tag{2.13}$$

where we will use vector $\boldsymbol{\mu} = \left(\mu_1, \ldots, \mu_{2N_\mathrm{N}}\right)$. Then we have

$$C\left(\mu_\mathrm{a}\right) = \sum_{l=1}^{N_\mathrm{N}} \mu_l V_l, \tag{2.14}$$

$$K\left(\kappa\right) = \sum_{l=1}^{N_\mathrm{N}} \mu_{l+N_\mathrm{N}} V_{l+N_\mathrm{N}}, \tag{2.15}$$

where

$$\left\{V_l\right\}_{m,n} = \int_\Omega u_l\left(\mathbf{r}\right) u_m\left(\mathbf{r}\right) u_n\left(\mathbf{r}\right) d\mathbf{r}, \tag{2.16}$$

$$\left\{V_{l+N_\mathrm{N}}\right\}_{m,n} = \int_\Omega u_l\left(\mathbf{r}\right) \nabla u_m\left(\mathbf{r}\right) \cdot \nabla u_n\left(\mathbf{r}\right) d\mathbf{r}. \tag{2.17}$$

The flux is expressed as

$$\Gamma_{i,j}\left(t\right) \approx \sum_{l=1}^{N_\mathrm{N}} P_{l,j} \Phi_{l,i}\left(t\right), \tag{2.18}$$

where

$$P_{l,j} = -c\kappa\left(\mathbf{r}_{\mathrm{D}j}\right) \chi_l\left(\mathbf{r}_{\mathrm{D}j}\right) \hat{\mathbf{n}}\left(\mathbf{r}_{\mathrm{D}j}\right) \cdot \nabla u_l\left(\mathbf{r}_{\mathrm{D}j}\right). \tag{2.19}$$

Here, $\chi_l\left(\mathbf{r}_{\mathrm{D}j}\right) = 1$ when the element τ_l belongs to $\mathbf{r}_{\mathrm{D}j} \in \partial\Omega$ and $\chi_l = 0$ otherwise.

The zeroth-order and the first-order moments of time-independent diffusion equations in Equations (2.7), (2.8) were discretized in the same manner as deriving Equation (2.10). The forms are

$$\left[\zeta\left(c\right) A + K\left(\kappa\right) + C\left(\mu_\mathrm{a}\right)\right] \mathbf{E}_i = \mathbf{q}_i, \tag{2.20}$$

$$\left[\zeta\left(c\right) A + K\left(\kappa\right) + C\left(\mu_\mathrm{a}\right)\right] \mathbf{M}_i = B\mathbf{E}_i, \tag{2.21}$$

where

$$\mathbf{E}_i = \int_0^\infty \mathbf{\Phi}_i\,(t)\,dt, \tag{2.22}$$

$$\mathbf{M}_i = \int_0^\infty t\mathbf{\Phi}_i\,(t)\,dt. \tag{2.23}$$

Then, Equation (2.4) is expressed as

$$g_{i,j} \approx g_{i,j}^{\mathrm{h}} = \frac{\mathbf{P}_j \cdot \mathbf{M}_i}{\mathbf{P}_j \cdot \mathbf{E}_i}, \tag{2.24}$$

where $\mathbf{P}_j = \left(\cdots P_{l,j} \cdots\right)^T$.

2.3 Image reconstruction

2.3.1 Objective function

We solved the inverse problem by minimizing the objective function given by

$$\Psi\,(\boldsymbol{\mu}) = \frac{1}{2}\sum_{i=1}^{N_{\mathrm{S}}}\sum_{j=1}^{N_{\mathrm{D}}} H_{i,j}\left[y_{i,j} - f_{i,j}\,(\boldsymbol{\mu})\right]^2 + \tau\sum_{l=1}^{N_{\mathrm{R}}}\left(\mu_l - \mu_{0,l}\right)^2, \tag{2.25}$$

which is the least square method for the measured result $y_{i,j}$ and the calculated result $f_{i,j}$; N_{S} and N_{D} are the numbers of the source and detection fibers used in measurements, respectively; $H_{i,j} = 1$ if $y_{i,j}$ have sufficient SNR, $H_{i,j} = 0$ if $y_{i,j}$ have insufficient SNR. The data type of the objective function is the normalized first-order moment. We used Tikhonov regularization and τ is the hyper parameter; N_{R} is the number of points of the reconstruction grid used to solve the inverse problem; l is the number of node. $\mu_0$is the initial absorption coefficient at the start of the reconstruction.

The measured TOF distribution ($Y_{i,j}$) contains unknown constants from the measurement setup. To remove these constants, we used the normalized first-order moment ($y_{i,j}$). The

form is

$$y_{i,j} = \frac{\int_0^T tY_{i,j}(t)\,dt}{\int_0^T Y_{i,j}(t)\,dt}. \tag{2.26}$$

And the calculated result $f_{i,j}$ corresponding to $y_{i,j}$ can be computed as

$$f_{i,j}(\boldsymbol{\mu}) = \frac{\int_0^\infty tF_{i,j}(\boldsymbol{\mu}, t)\,dt}{\int_0^\infty F_{i,j}(\boldsymbol{\mu}, t)\,dt}, \tag{2.27}$$

where $F_{i,j}$ is the convolution of the IRF $D_{i,j}$and the flux $\Gamma_{i,j}$. The form is

$$F_{i,j}(\boldsymbol{\mu}, t) = \int_0^t D_{i,j}(s)\,\Gamma_{i,j}(t-s)\,ds. \tag{2.28}$$

If we substitute Equation (2.28) into Equation (2.27) [21], we obtain

$$\begin{aligned} f_{i,j}(\boldsymbol{\mu}) &= \frac{\int_0^\infty tD_{i,j}(t)\,dt}{\int_0^\infty D_{i,j}(t)\,dt} + \frac{\int_0^\infty t\Gamma_{i,j}(t)\,dt}{\int_0^\infty \Gamma_{i,j}(t)\,dt}, \\ &\approx \frac{\int_0^\infty tD_{i,j}(t)\,dt}{\int_0^\infty D_{i,j}(t)\,dt} + g_{i,j}^{\mathrm{h}}. \end{aligned} \tag{2.29}$$

2.3.2 Nonlinear conjugate gradient method

To find the optimum solution of the Equation (2.25), we used the nonlinear conjugate gradient method with the Polak–Ribière method [22], [23] in Algorithm 1, which is implemented in TOAST++ [24].

Algorithm 1 The algorithm of nonlinear conjugate gradient method

Define termination criterion ε_{c}
Given $\boldsymbol{\mu}_0 = \left(\mu_{0,1} \ldots \mu_{0,N_{\mathrm{R}}} \ldots \mu_{0,2N_{\mathrm{R}}}\right)^T$
Evaluate $\Psi_0 = \Psi(\boldsymbol{\mu}_0), \quad \nabla\Psi_0 = \left(\frac{\partial\Psi_0}{\partial\mu_{0,1}} \cdots \frac{\partial\Psi_0}{\partial\mu_{0,N_{\mathrm{R}}}}\right)^T$
Set $\mathbf{d}_0 = -\nabla\Psi_0$, $k = 0$
while $\Psi_k - \Psi_{k-1} < \varepsilon_{\mathrm{c}}$ **do**
  Find α_k that minimizes $\Psi\left(\boldsymbol{\mu}_k + \alpha_k \mathbf{d}_k\right)$
  $\boldsymbol{\mu}_{k+1} = \boldsymbol{\mu}_k + \alpha_k \mathbf{d}_k$
  Compute $\nabla\Psi_{k+1}$
  $\beta_{k+1} = \frac{\nabla\Psi_{k+1}^T(\nabla\Psi_{k+1} - \nabla\Psi_k)}{\|\nabla\Psi_k\|^2}$
  $\mathbf{d}_{k+1} = -\nabla\Psi_{k+1} + \beta_{k+1}\mathbf{d}_k$
  $k = k + 1$
end while

The gradient of the objective function $\nabla\Psi$ was obtained with the following adjoint method. The gradient of the objective function is given as

$$\frac{\partial\Psi}{\partial\mu_l} = \sum_{i=1}^{N_{\mathrm{S}}}\sum_{j=1}^{N_{\mathrm{D}}} H_{i,j}\left[y_{i,j} - f_{i,j}\left(\boldsymbol{\mu}\right)\right]\left[-\frac{\partial f_{i,j}\left(\boldsymbol{\mu}\right)}{\partial\mu_l}\right] + 2\tau\left(\mu_l - \mu_{0,l}\right), \tag{2.30}$$

where

$$\begin{aligned} -\frac{\partial f_{i,j}\left(\boldsymbol{\mu}\right)}{\partial\mu_l} &= \frac{\partial}{\partial\mu_l}\frac{\mathbf{P}_j \cdot \mathbf{M}_i}{\mathbf{P}_j \cdot \mathbf{E}_i}, \\ &= \frac{\mathbf{P}_j \cdot \mathbf{M}_i}{\left(\mathbf{P}_j \cdot \mathbf{E}_i\right)^2}\frac{\partial\mathbf{P}_j \cdot \mathbf{E}_i}{\partial\mu_l} - \frac{1}{\mathbf{P}_j \cdot \mathbf{E}_i}\frac{\partial\mathbf{P}_j \cdot \mathbf{M}_i}{\partial\mu_l}. \end{aligned} \tag{2.31}$$

Let us introduce the Green matrix G as

$$\left[\zeta\left(c\right)A + K\left(\kappa\right) + C\left(\mu_{\mathrm{a}}\right)\right]G = I_{\mathrm{mat}}, \tag{2.32}$$

where I_{mat} is the identity matrix. The reciprocal relation of the Green's function for the

diffusion equation implies that G is symmetric. For a given source vector $\mathbf{Q}$, let us consider

$$\left[\zeta\left(c\right)A + K\left(\kappa\right) + C\left(\mu_{\mathrm{a}}\right)\right]\mathbf{\Phi} = \mathbf{Q}. \tag{2.33}$$

We note that

$$\left[\zeta\left(c\right)A + K\left(\kappa\right) + C\left(\mu_{\mathrm{a}}\right)\right]\frac{\partial\mathbf{\Phi}}{\partial\mu_l} = \frac{\partial\mathbf{Q}}{\partial\mu_l} - V_l\mathbf{\Phi}. \tag{2.34}$$

Hence, we obtain for some vector $\mathbf{p}$,

$$\mathbf{p}\cdot\frac{\partial\mathbf{\Phi}}{\partial\mu_l} = \mathbf{p}^T G\left(\frac{\partial\mathbf{Q}}{\partial\mu_l} - V_l\mathbf{\Phi}\right) = \left(\frac{\partial\mathbf{Q}^T}{\partial\mu_l} - \mathbf{\Phi}^T V_l\right)G\mathbf{p}. \tag{2.35}$$

We define

$$\mathbf{\Phi}_{\mathrm{adj}}\left(\mathbf{p}\right) = G\mathbf{p}. \tag{2.36}$$

Then we have

$$\mathbf{p}\cdot\frac{\partial\mathbf{\Phi}}{\partial\mu_l} = \mathbf{\Phi}_{\mathrm{adj}}\left(\mathbf{p}\right)^T\left(\frac{\partial\mathbf{Q}}{\partial\mu_l} - V_l\mathbf{\Phi}\right). \tag{2.37}$$

The vector $\mathbf{\Phi}_{\mathrm{adj}}\left(\mathbf{p}\right)$ satisfies the adjoint equation given by

$$\left[\zeta\left(c\right)A + K\left(\kappa\right) + C\left(\mu_{\mathrm{a}}\right)\right]\mathbf{\Phi}_{\mathrm{adj}}\left(\mathbf{p}\right) = \mathbf{p}. \tag{2.38}$$

We first set $\mathbf{Q} = \mathbf{q}_i$ and $\mathbf{p} = \mathbf{P}_j$, and we obtain

$$\mathbf{P}_j\cdot\frac{\partial\mathbf{E}_i}{\partial\mu_l} = -\mathbf{\Phi}_{\mathrm{adj}}\left(\mathbf{P}_j\right)^T V_l\mathbf{E}_i. \tag{2.39}$$

Next, we set $\mathbf{Q} = \mathbf{q}_i$ and $\mathbf{p} = B\mathbf{\Phi}_{\mathrm{adj}}\left(\mathbf{P}_j\right)$, and we have

$$B\mathbf{\Phi}_{\mathrm{adj}}\left(\mathbf{P}_j\right)\cdot\frac{\partial\mathbf{E}_i}{\partial\mu_l} = -\mathbf{\Phi}_{\mathrm{adj}}\left[B\mathbf{\Phi}_{\mathrm{adj}}\left(\mathbf{P}_j\right)\right]^T V_l\mathbf{E}_i. \tag{2.40}$$

Finally, let us set $\mathbf{Q} = B\mathbf{E}_i$ and $\mathbf{p} = \mathbf{P}_j$. We obtain

$$\begin{aligned}\mathbf{P}_j \cdot \frac{\partial \mathbf{M}_i}{\partial \mu_l} &= -\mathbf{\Phi}_{\mathrm{adj}} \left(\mathbf{P}_j\right)^T \left(B\frac{\partial \mathbf{E}_i}{\partial \mu_l} - V_l \mathbf{M}_i\right), \\ &= -\mathbf{\Phi}_{\mathrm{adj}} \left[B\mathbf{\Phi}_{\mathrm{adj}} \left(\mathbf{P}_j\right)\right]^T V_l \mathbf{E}_i - \mathbf{\Phi}_{\mathrm{adj}} \left(\mathbf{P}_j\right)^T V_l \mathbf{M}_i.\end{aligned} \tag{2.41}$$

Therefore, the gradient of objective function $\nabla \Psi$ is obtained by Equations (2.30), (2.31), (2.39), (2.41).

Chapter 3

Verification of the NIROT image reconstruction algorithm by using the solid phantoms

3.1 Materials and methods

3.1.1 Phantoms

To validate the image reconstruction algorithm in Section 2.3, we used two solid phantoms (BIOMIMIC^{TM} OPTICAL PHANTOMS, INO, Québec, QC, Canada) [25], [26], of which μ_a and μ_s' are are similar to those of biological tissues. One is homogeneous phantom and the other is a heterogeneous phantom (Figure 3.1). These two phantoms are polyurethane-based phantoms and include carbon black (absorber) and titanium oxide (scatterer). Table 3.1 shows optical properties (the absorption coefficient, the reduced scattering coefficient and refractive index) of the phantoms and the inclusions. The homogeneous and heterogeneous phantoms are a cuboid (40 (W) $\times$ 40 (D) $\times$ 70 mm (H)). The heterogeneous phantom includes two kinds of cylindrical inclusions with a diameter of 5 mm and a height of 70 mm

(Incl.A and Incl.B). These two inclusions are epoxy resin based phantoms and include the absorber (gardenia dye green , Kyoritsu-foods, Taito, Japan) and titanium oxide (scatterer). The optical properties of Incl.A are almost the same as those of the background, while the absorption coefficient of Incl.B is approximately three times higher than that of the background (Table 3.1)

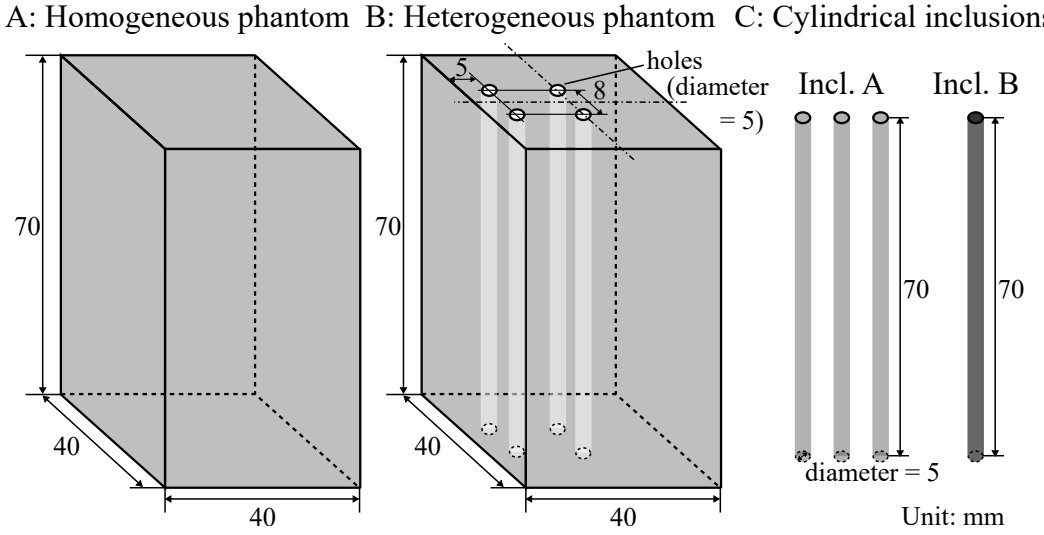

Figure 3.1. Overview of the solid phantoms. (A): Homogeneous phantom. (B): Heterogeneous phantom. (C): Two kinds of cylindrical inclusions.

Table 3.1: Optical properties at 800 nm of the phantoms and the inclusions.

Phantoms and inclusions	Absorption coefficient (μ_a) (mm^{-1})	Reduced scattering coefficient (μ_s') (mm^{-1})	Refractive index (n)
Homogeneous phantom	0.021	0.853	1.52
Heterogeneous phantom	0.021	0.853	1.52
Incl.A	0.019	0.86	1.58
Incl.B	0.0637	0.86	1.58

3.1.2 Time-domain near-infrared measurement

Firstly, we measured the IRFs at 36 source detection fiber pairs (six source fibers × six detection fibers). All the IRFs were almost the same as those shown in Figures 2.3-2.5.

Then, the homogeneous phantom was measured with TRS-80. The source and detection fibers were placed on three sides of the phantom at the height of 35 mm with a fiber holder (Figure 3.2A). The fiber arrangements are shown in Figure 3.2B.

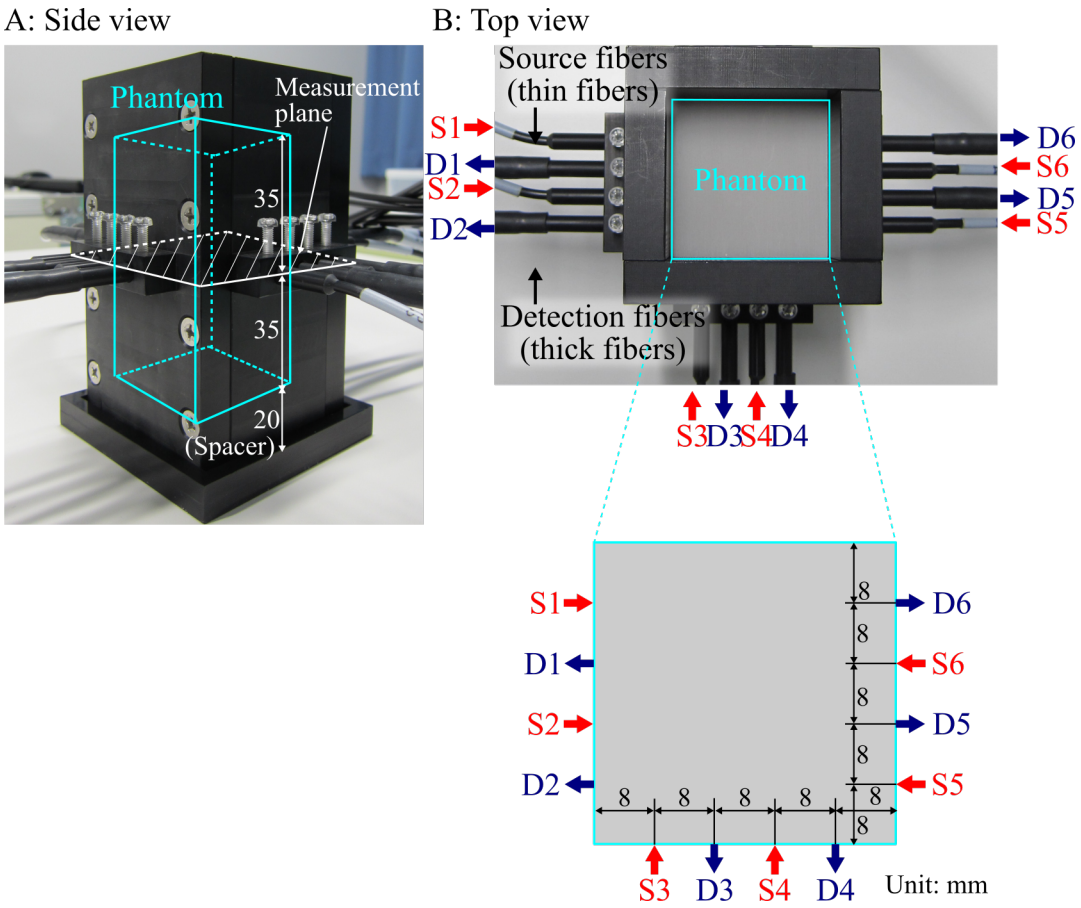

Figure 3.2. Photograph of the homogeneous phantom measurement. (A): Side view (B): Top view S# denotes the number of the source fiber. D# denotes the number of the detection fiber.

The heterogeneous phantom with three Incl.As and one Incl.B was measured in the same manner as the homogeneous phantom (Figure 3.3).

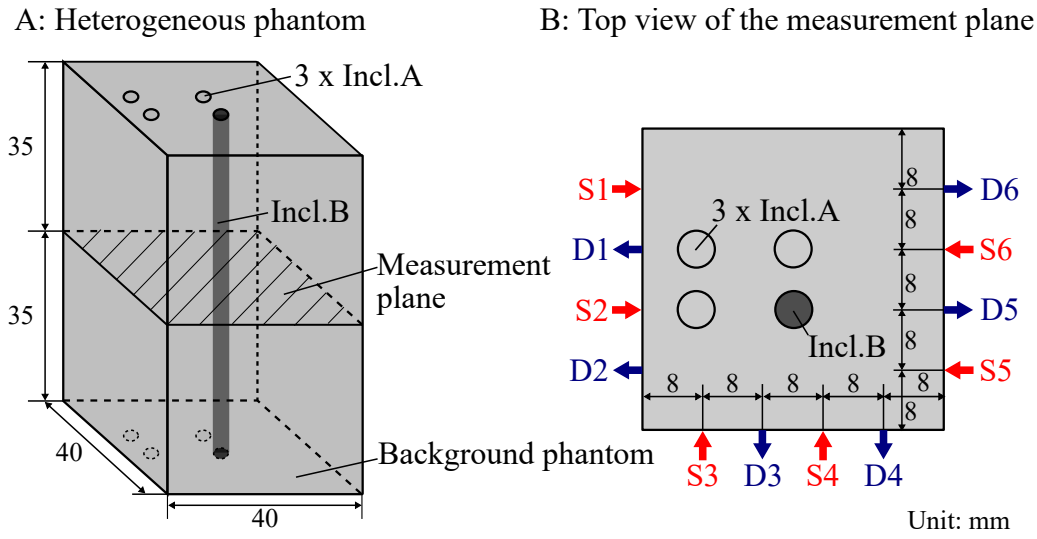

Figure 3.3. The heterogeneous phantom and the arrangement of the source and detection fibers. (A): The heterogeneous phantom, which includes three Incl.As and a Incl.B (B): Top view of the fiber arrangement. S# denotes the number of the source fiber. D# denotes the number of the detection fiber.

The both measurements were performed for 10 s at each source fiber and the total measurement time is about 90 s. The SNRs of all the 36 (six source fibers × six detection fibers) TOF distributions in the heterogeneous phantom at 801 nm were sufficient (Figure 3.4) as well as those of the TOF distributions in the homogeneous phantom (Figure 3.5).

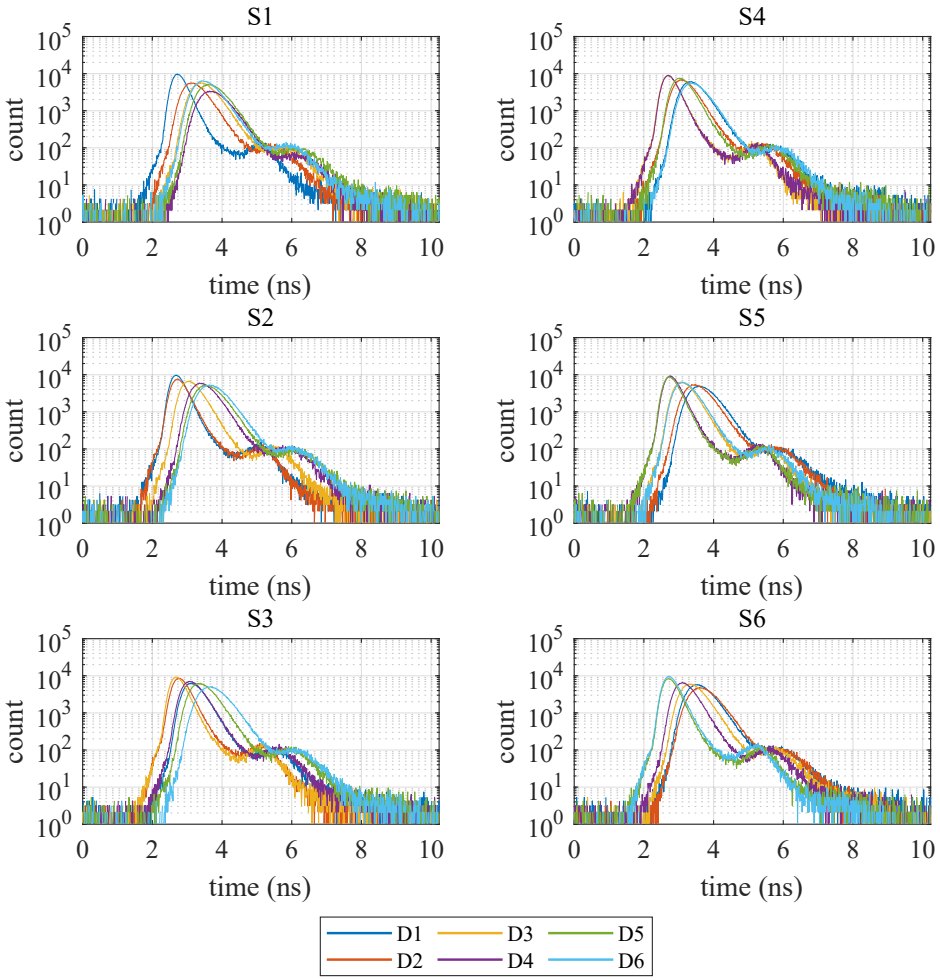

Figure 3.4. Time-of-flight distributions in the heterogeneous phantom at 801 nm. S# denotes the number of the source fiber. D# denotes the number of the detection fiber.

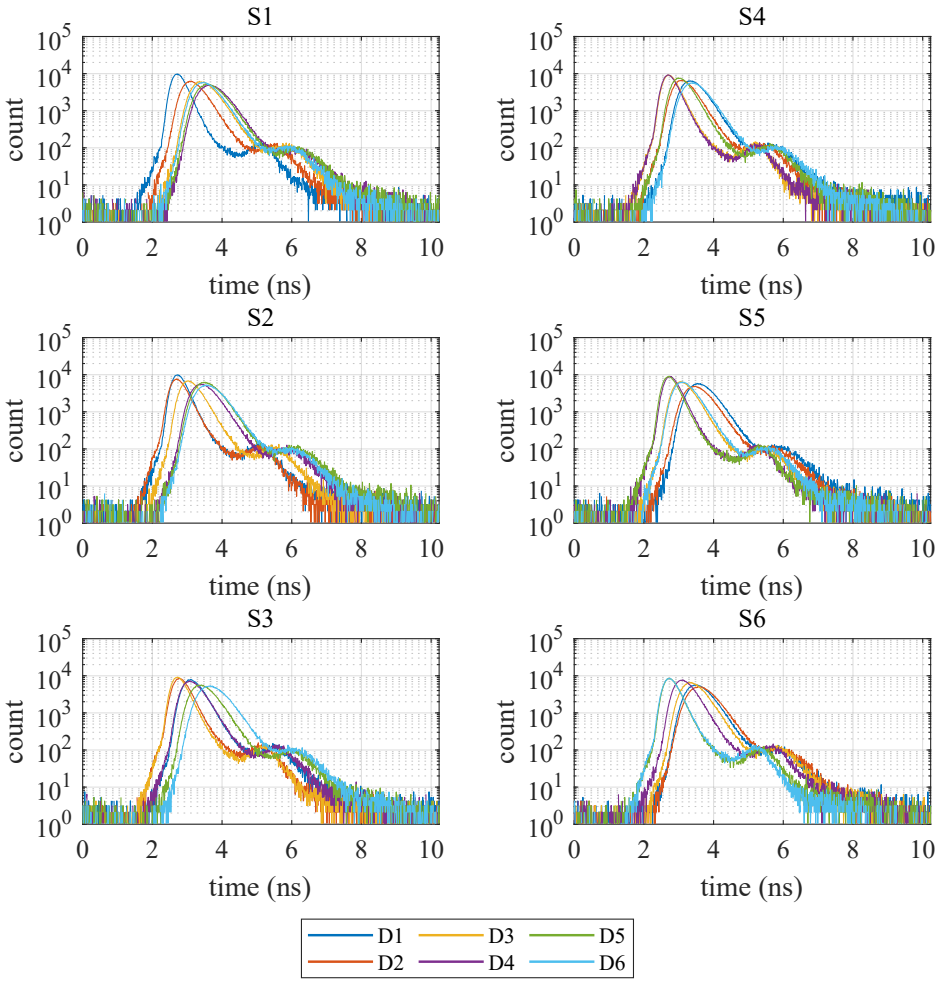

Figure 3.5. Time-of-flight distributions in the homogeneous phantom at 801 nm. S# denotes the number of the source fiber. D# denotes the number of the detection fiber.

3.1.3 Generation of the finite element grid

Figure 3.6 shows the grid to solve the TD-DE with FEM, which was generated by Gmsh [27]. The numbers of the FEM grids were about $40 \times 40 \times 40$ and the dimensions were $40 \times 40 \times 40$ mm. The grid is consisted of the tetrahedron meshes of the 1 mm side length. Although the height of the grid was smaller than the actual height 70 mm, it hardly influenced on the tomographic images. For the image reconstruction (inverse solution), the number of the grids were reduced to $32 \times 32 \times 32$ grids. The interpolated 3D mesh was automatically generated by TOAST++ [24].

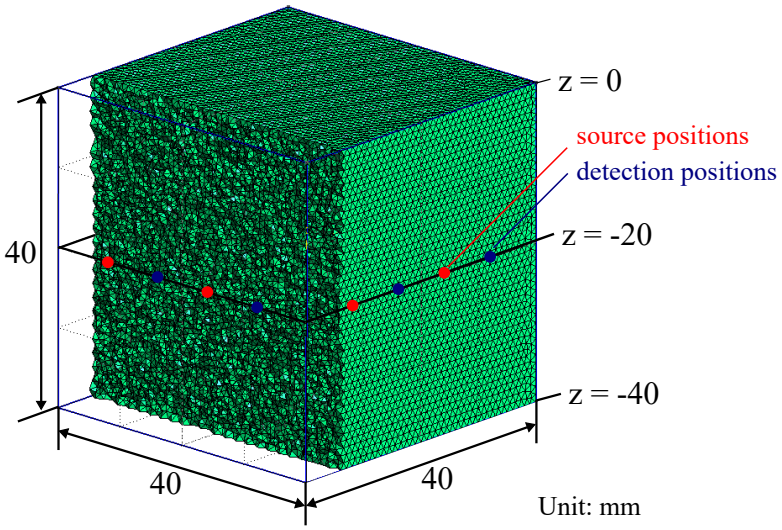

Figure 3.6. 3D grid for the phantom image reconstruction. The dimensions are 40 × 40 × 40 mm. The grid is composed of many triangle grids, which the side length is about 1 mm. The red and blue filled circles show the source and detection positions in the numerical calculation, respectively. The positions correspond to the actual source and detection positions of the measurement.

3.1.4 Image reconstruction of the phantoms

We excluded 11 TOF distributions of measured by adjacent source-detector pairs (source-detector distance of 8 mm or 11 mm) for image reconstruction because the diffusion approximation is generally invalid in the vicinity of light source (within about 10 mm) . Therefore, in Equation (2.25), we set $H_{i,j} = 0$ when (i, j) = (1, 1), (2, 1), (2, 2), (3, 2), (3, 3), (4, 3), (4, 4), (5, 4), (5, 5), (6, 5), and (6, 6), and $H_{i,j} = 1$ when otherwise.

In the initial condition, we set the hyper parameter $\tau = 0.0001$ and assumed that the phantom was optically homogeneous even for the heterogeneous phantom. The initial absorption and reduced scattering coefficients were are set as 0.02 mm^{-1} and 0.853 mm^{-1}, respectively, which were the same as those of the homogeneous phantom shown in Table 3.1. The refractive index was 1.52.

3.2 Tomographic images of the phantoms

3.2.1 Tomographic images of the homogeneous phantom

Figure 3.7 shows the objective function (Equation (2.25)) values (Ψ) with respect to the number of iterations. The Ψ values gradually decreased and converged to a constant value as the number of iterations increased.

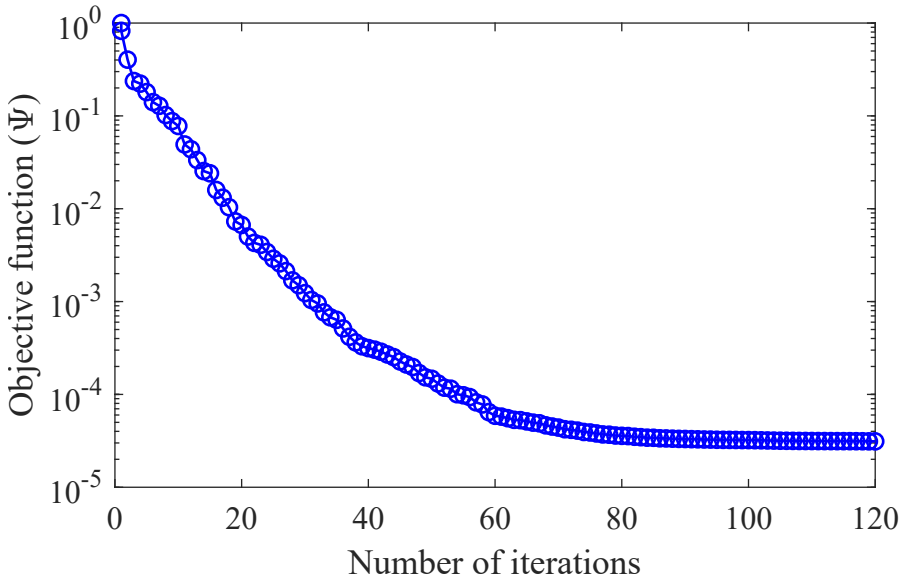

Figure 3.7. The objective function values with respect to the number of iterations in the homogeneous phantom.

Figure 3.8 shows the cross section (z = -20, Figure 3.6) of the tomographic images at 115th iteration. The high absorption region was reconstructed in near the source-detection fibers.

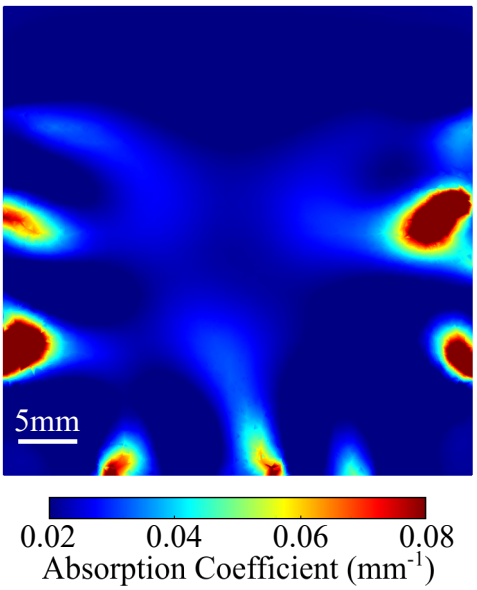

Figure 3.8. Cross section (z = -20) of the tomographic images of absorption coefficient at 801 nm of the homogeneous phantom.

3.2.2 Tomographic images of the heterogeneous phantom

Figure 3.9 shows the objective function (Equation (2.25)) values (Ψ) with respect to the number of iterations. The Ψ values gradually decreased and converged to a constant value as the number of iterations increased.

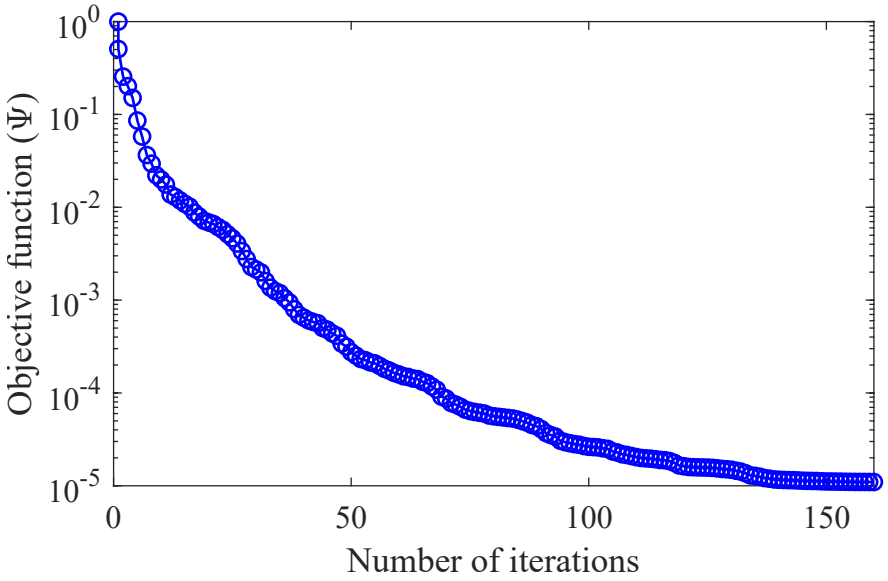

Figure 3.9. The objective function values with respect to the number of iterations in the heterogeneous phantom.

Figure 3.10 shows the cross section (z = -20, Figure 3.6) of the tomographic images at 158th iteration. The high absorption region was reconstructed at the position of Incl.B, while high absorption areas were also reconstructed near the boundaries like the image reconstruction of the homogeneous phantom.

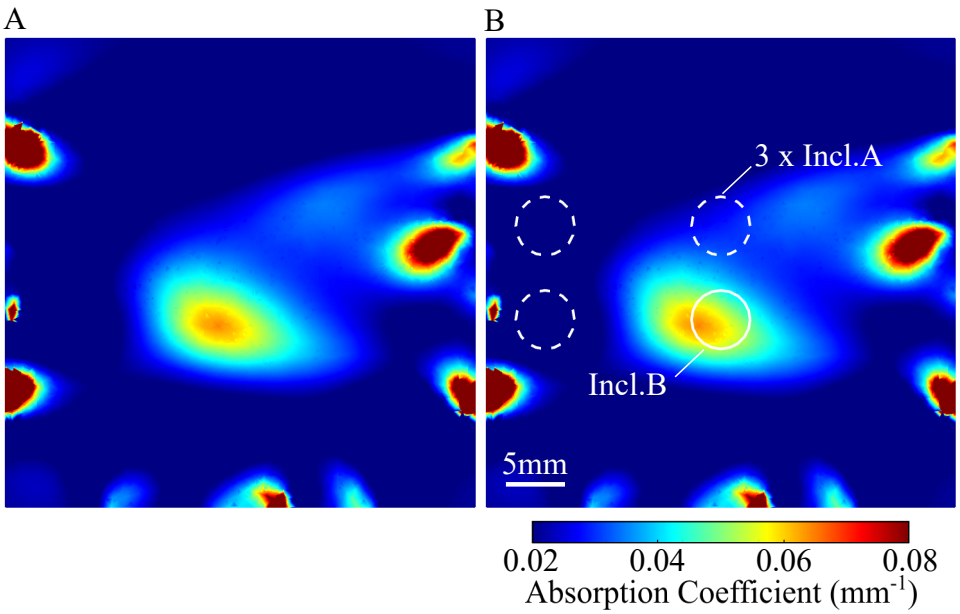

Figure 3.10. Cross section (z = -20) of the tomographic images of absorption coefficients at 801 nm of the heterogeneous phantom. (A): Cross section (z = -20). (B): Cross section (z = -20). Incl.A and Incl.B are denoted by white dashed line and white line, respectively.

To reduce decrease the artifact caused by of the source-detection fibers, subtraction of images of the homogeneous phantom from those of the heterogeneous images was performed. Figure 3.11 shows the subtraction image. The maximum value of the absorption coefficient was 0.0402 mm^{-1} and the location with this value was within the Inc.B

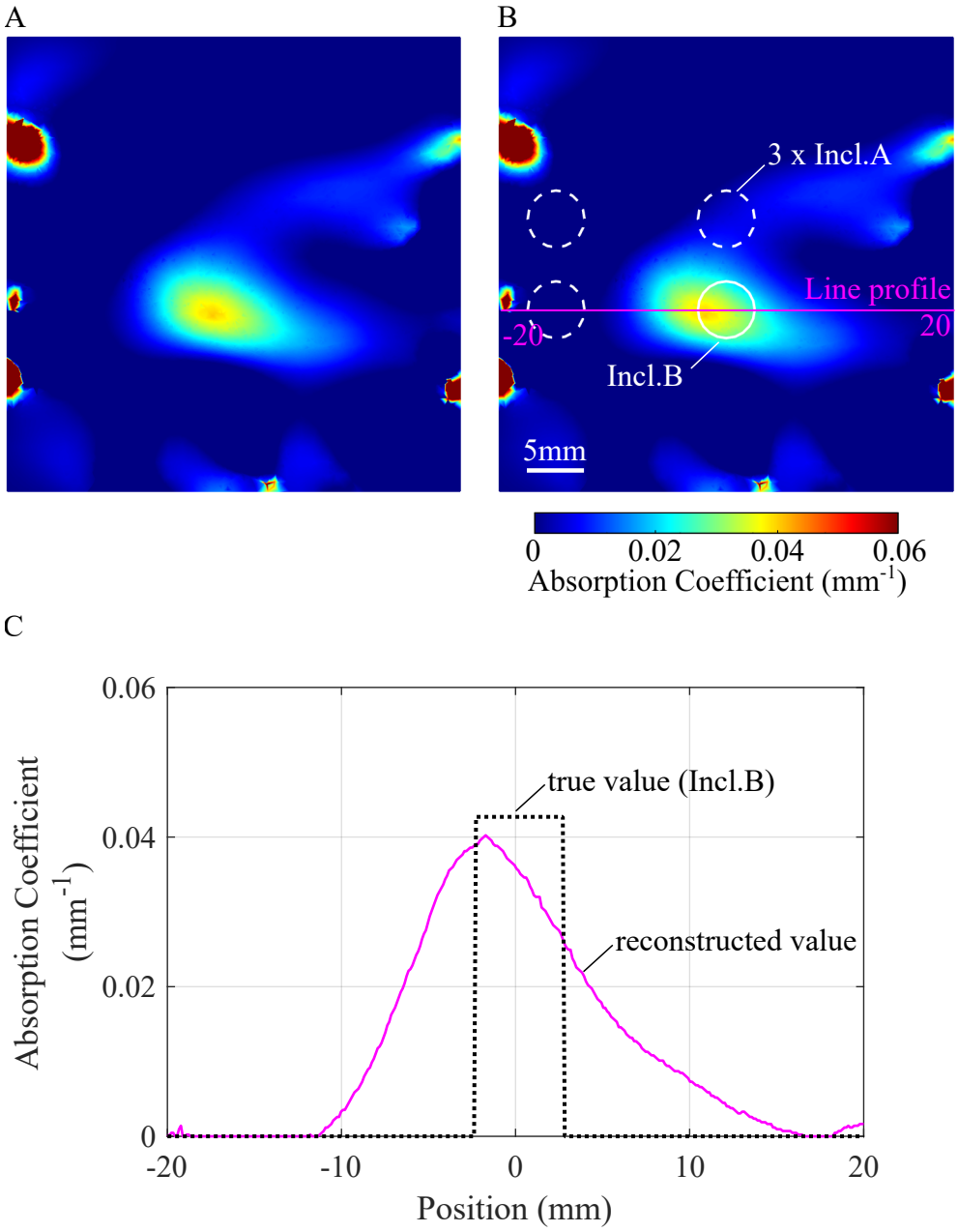

Figure 3.11. Cross section (z = -20) of the subtraction image of absorption coefficients at 801 nm (heterogeneous - homogeneous). (A): Cross section (z = -20). (B): Cross section (z = -20). Incl.A and Incl.B are denoted by white dashed line and white line, respectively. The position of the line profile is denoted by the magenta line. (C): Line profile. The true values of the absorption coefficient of Incl.B and the reconstructed values are denoted by the black dashed line and the magenta line, respectively.

3.3 Discussion

The maximum value of the reconstructed absorption coefficient at 801 nm was nearly equal to the true value, although the absorption distribution was broader and the position was slightly shifted by less than 3 mm, which is smaller than the diameter of Incl.B. Although it takes much more time for calculation, the spatial accuracy can be improved by using multiple data types of the TOF distribution, such as a combination of moments and Laplace transforms [26] and the whole TOF distribution [28].

Figure 3.11 remained the artifact near the boundary in the subtraction image. Since the conditions of the fiber contact were not necessarily the same between the homogeneous and the heterogeneous measurements. Such a little difference likely made the artifact.

In this phantom study, we have confirmed the validity of our image reconstruction algorithm.

Chapter 4

Near infrared optical tomography in the neck

4.1 Subject and methods

4.1.1 Experimental procedures

Figure 4.1 shows the flow chart of the experimental procedures. Firstly, magnetic resonance imaging (MRI) scan was conducted on a subject to confirm the tracheal and thyroid positions. Then, the MR images segmentation was performed to identify the neck, trachea, and thyroid. Based on the segmented images, a fiber holder was made and the finite element grids were generated. Then, using the holder, TRS-80 performed the optical measurement of the neck and obtained the TOF distributions. Finally, using the grids and the TOF distributions, image reconstruction was performed and obtained tomographic images of absorption coefficients and tissue oxygen saturation.

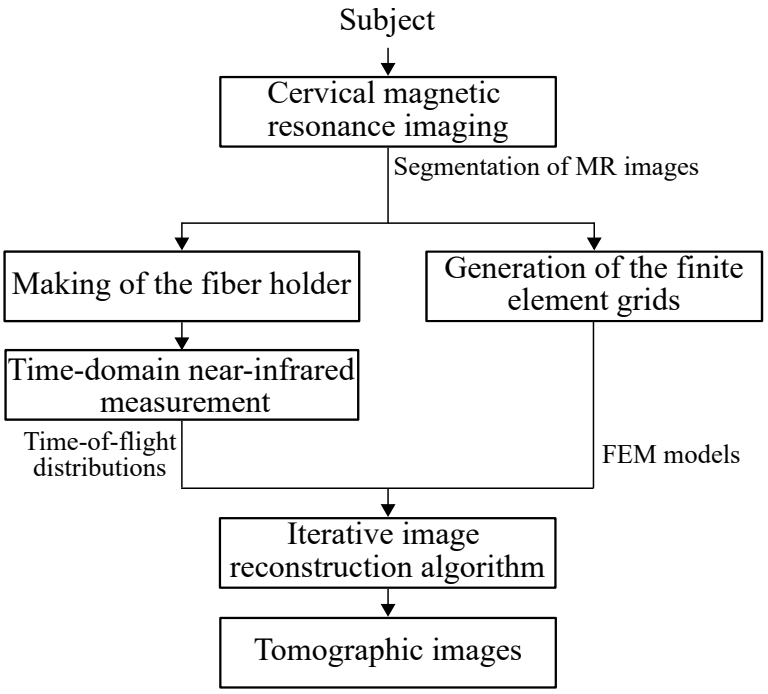

Figure 4.1. Flow chart of the experimental procedures for the neck image reconstruction

4.1.2 Subject and magnetic resonance imaging

The subject is a healthy woman who was informed of the aim and procedures of this study. This study was approved by the ethical committee of Hamamatsu University School of Medicine (No. 15-082). To confirm the tracheal and thyroid positions, a cervical magnetic resonance imaging (MRI) scan was performed (Discovery MR750, GE Healthcare, Waukesha, WI, USA). For MRI scan, a vacuum cushion for radiotherapy was used to fix the neck position since the same neck position must be reproduced in the optical measurement in Section 4.1.5. Figure 4.2 shows the portions of the T2-weighted MR images.

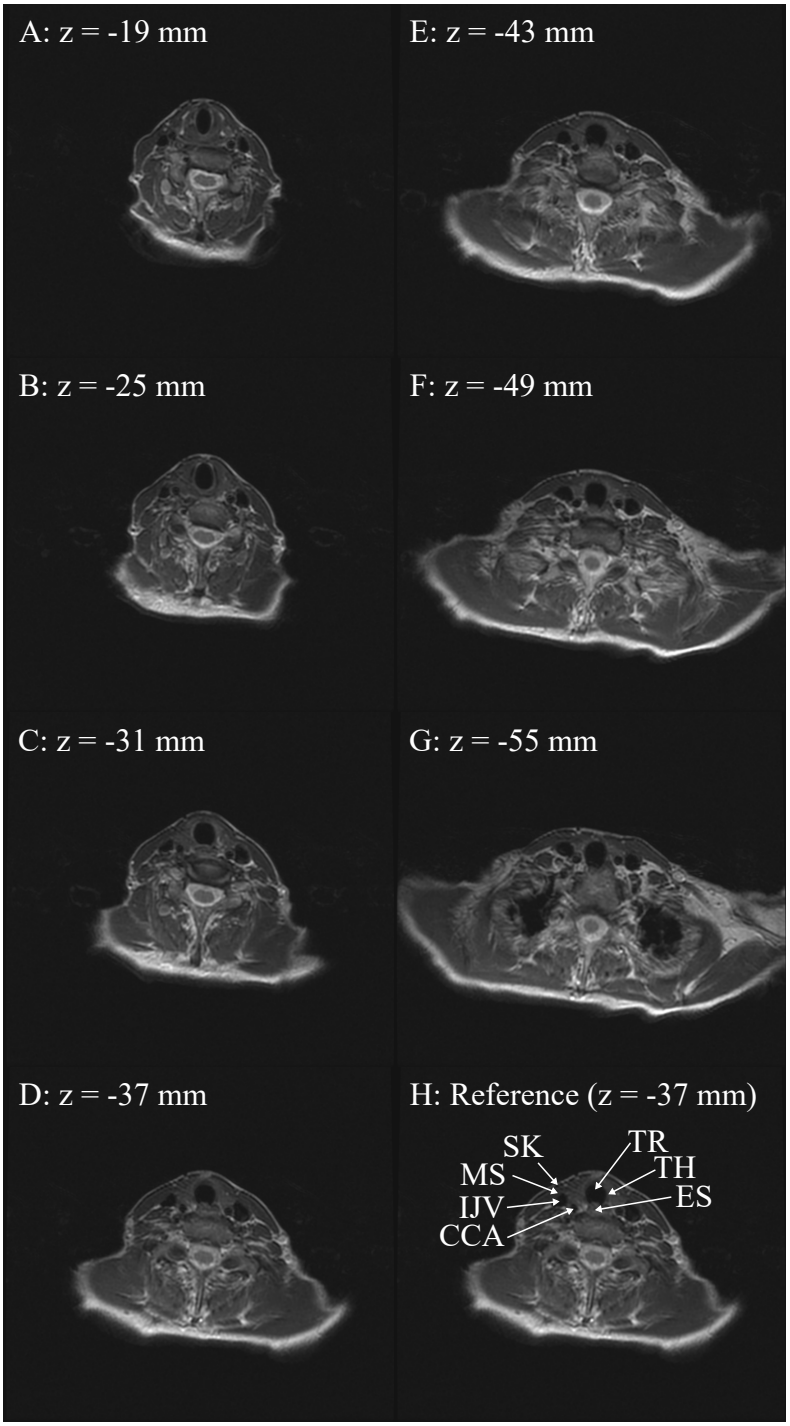

Figure 4.2. T2-weighted cervical magnetic resonance images of the subject (axial slices). (A): z = −19 mm. (B): z = −25 mm. (C): z = −31 mm. (D): z = −37 mm. (E): z = −43 mm. (F): z = −49 mm. (G): z = −55 mm. (H): Reference (z=−37 mm). SK, skin; MS, muscle; IJV, internal juglar vein; CCA, common carotid artery; TR, Trachea; TH thyroid; ES, esophagus.

Then the MR images were processed with the open source software platform for medical

image processing (3D-Slicer, version 4.10.2) [29] to generate the 3D surface geometry of the neck. First, the T2-weighted MR image was saved as the DICOM standard, which contains multiple slices and all pixels of each of the slices related to the real position and scale. Then 3D-Slicer loaded the DICOM file of the MR images, and contours of the neck, thyroid, and trachea were delineated by the Segment Editor module. Figure 4.3 shows the segmented images of the neck, thyroid, and trachea, respectively. Finally, the Segmentations module exported the 3D surface geometry of their objects (Figure 4.3) in an Standard Triangulated Language (STL) file format at LPS (Left, Posterior, Superior) coordinate system. All STL files contain real-scale anatomical structures of the neck using the coordinates of the MR image. These segmented images were also used to make a fiber holder in Section 4.1.3 and grids for the FEM in Section 4.1.4.

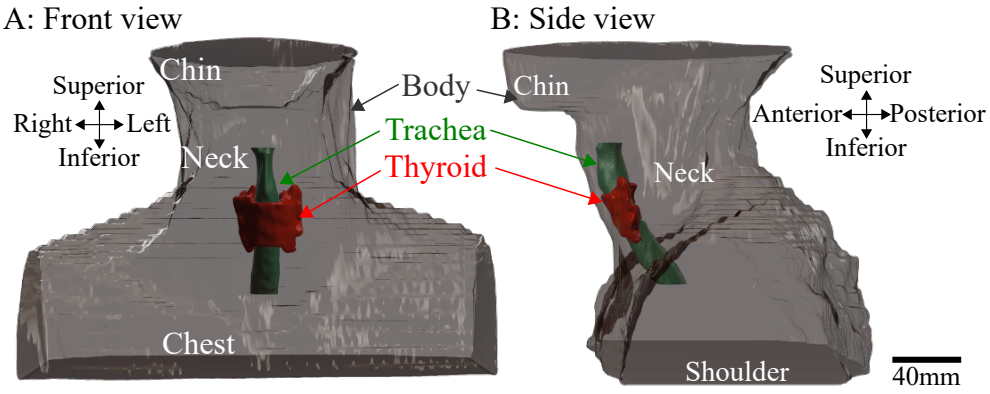

Figure 4.3. Segmented images in the neck, the thyroid, and the trachea. (A): Front view. (B): Side view.

4.1.3 Making a fiber holder

Based on the segmented images of the neck and thyroid in Figure 4.3, a fiber holder was made by the 3D-computer-aided design (CAD) software (Fusion360, Autodesk, San Rafael, CA, USA). Figure 4.4 shows the holder, in which 25 holes are aligned. The center hole corresponds to the middle of the isthmus in Figure 4.4C and others were aligned in 5 rows and 5 columns. Since the thyroid is a superficial organ and the minimum distance between

the skin and the thyroid was about 1 cm in this subject, 1.5 cm was used as the shortest source-detector distance. The black natural rubber (KSNR-10054T, HIKARI CO., LTD., Osaka, Japan) inside the holder (Figure 4.4B) is used to absorb light at the interface between air and the skin so that the Robin boundary condition is applied to numerical modeling of light propagation. In addition, it plays the role of a cushion between the rigid holder and the neck.To fix optical fibers inserted in the holes tightly, we made the fiber retention mechanism by screw on the holes in Figure 4.4D. After the designs, the holder was manufactured by 3D printer (Agilista, Keyence, Osaka, Japan).

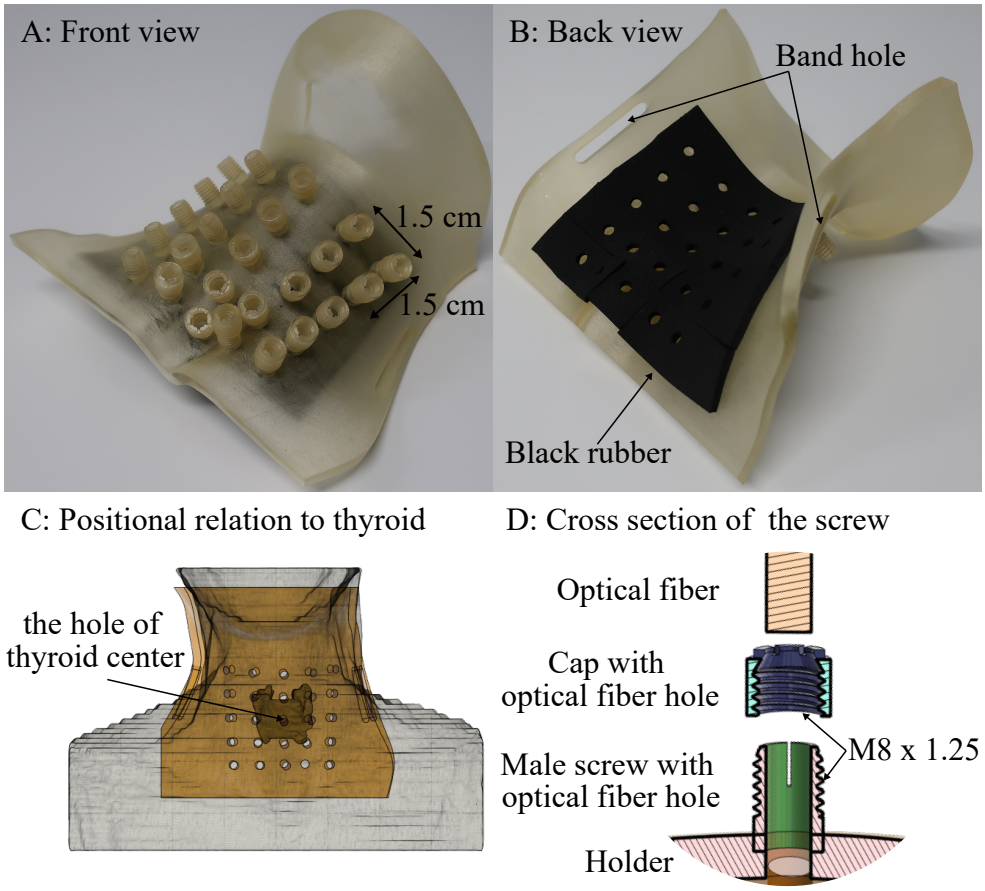

Figure 4.4. Pictures and structure of the fiber holder. (A): Front view. (B): Back view. (C): Positional relationship the fiber holder to thyroid. (D): Cross section of the screw, which is denoted in (A) with black line.

4.1.4 Generation of the finite element grids

The NIROT images suffer from a void region if no care is taken for the grid used for the finite element method [30], [31]. To create a grid excluding the void region of the trachea, we made use of MR neck images.

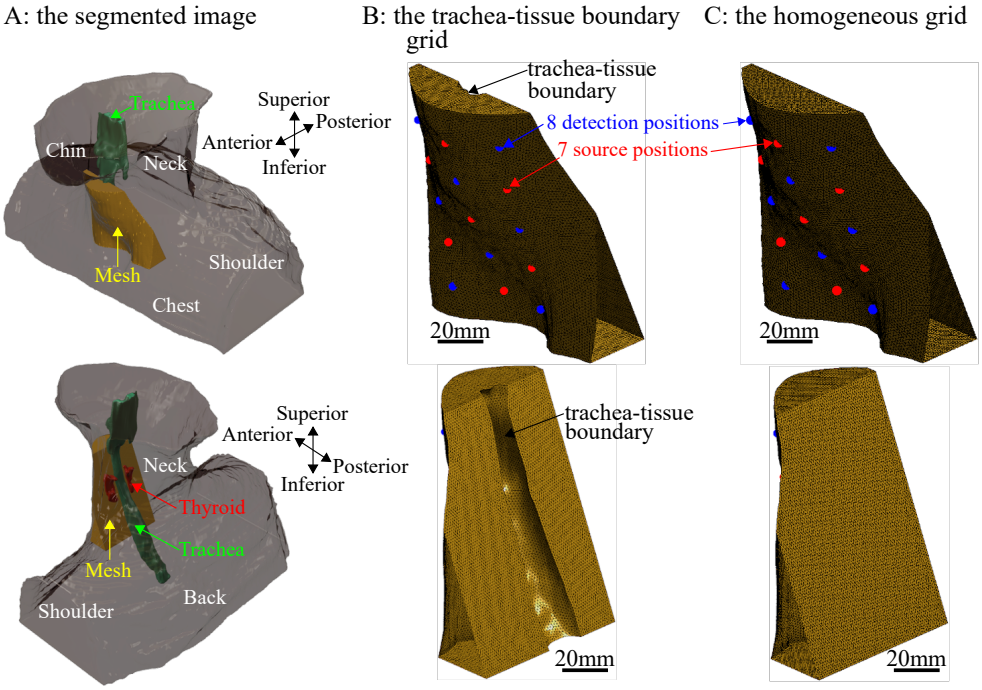

Figure 4.5. Front (top) and back views (bottom) of the segmented model and grids used for image reconstruction. (A) Segmented model from the MR image: the neck and body (gray), the trachea (green), the thyroid (red), and the approximate location of the grid (yellow). (B) The trachea-tissue boundary grid. The source positions (red) and detection positions (blue) are also shown. (C) The homogeneous grid. The source positions (red) and detection positions (blue) are also shown.

The 3D-CAD software imported the STL files and extracted the minimum volume that is required for the image reconstruction. Since the number of photons quickly decays when near-infrared light propagates in the neck, there is no need for making the grid using the entire volume. Here, light propagation around the thyroid was numerically studied and this rapid decay was observed [32]. The upper and lower boundaries of the volume were set as horizontal sections 10 mm above the top row and 10 mm below the bottom row of the optical fibers, respectively. The sides of the volume were sagittal sections 10 mm away

from the left and right columns of the optical fibers. The posterior limit was a plane that divided the void region approximately into halves. This grid is termed the trachea-tissue boundary grid in the following. The processed surface geometry is shown in Figure 4.5B. As a comparison, we made another grid by disregarding the presence of the trachea. This grid is termed as the homogeneous grid in the following (Figure 4.5C).

As a last step, the processed STL files were imported into the Gmsh version 4.6.0 [27] to create 3D volume grids for use with the finite element method. The Gmsh generates a very nearly uniform volume of tetrahedral grids where nodes of the surface are not necessarily identical to the nodes from the STL file. The side length of a tetrahedron was about 1 mm. In this way, uniform grids of tetrahedrons were used for the NIROT. The trachea-tissue boundary grid (Figure 4.5B) has 53,611 nodes and 264,526 elements, and the homogeneous grid (Figure 4.5C) has 57,433 nodes and 291,968 elements.

In the image reconstruction, the interpolated 3D grids were used. The interpolated 3D mesh is the same dimensions as the 3D grids and are automatically interpolated to 32 $\times$ 32 $\times$ 32 grids by TOAST++ [24]. The interpolated grids consist of rectangular voxels converted from the FEM grid and one voxel size is 1.9 (W) $\times$ 1.6 (D) $\times$ 2.5 mm (H). The value of N_R is 8,014 in the trachea-tissue boundary grid (Figure 4.5B), and N_R is 8,992 in the homogeneous grid (Figure 4.5C);

4.1.5 Time-domain near-infrared measurement

We firstly measured the IRF in all combinations of the source and detection fibers. All the IRFs were almost the same as those shown in Figures 2.3-2.5 and have sufficient SNR.

Next, we measured the human neck. Since the thyroid is a superficial organ and the minimum distance between the skin and the thyroid was about 1 cm in this subject, 1.5 cm was used as the shortest source–detector distance. A total of 15 holes in the holder were arranged at an interval of 1.5 cm and 7 source and 8 detector fibers were inserted into the

holes alternately so that the whole thyroid was illuminated (Figure 4.6). As a result, 56 datasets (7 × 8) were obtained. Each fiber was placed perpendicular to the skin surface. Optical fibers were fixed firmly to the holder by the screw cap on each hole of the holder. Moreover, the empty holes were filled with black polyoxymethylene cylinders. This fiber arrangement enables us to detect light passing through the thyroid and reduce influences of any strong absorption occurring in the internal jugular vein (IJV) and the common carotid artery (CCA), which are far from the optical fibers. The holder with the optical fibers was attached to the neck of the subject using the triumphal-arch shaped support. The subject was lying down on the vacuum cushion be able to reproduce the neck position as for the MRI scan.

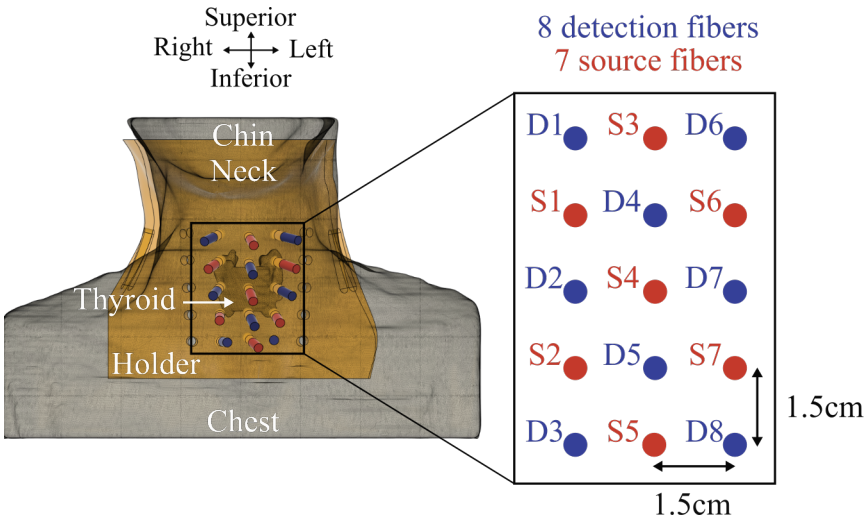

Figure 4.6. Measurement positions of the neck. The gray and yellow objects are the segmented image of the neck and the fiber holder, respectively. The source and detection positions are shown by the red and blue cylindrical rods on the fiber holder, and the red and blue filled circle, respectively. S# and D# denotes the number of the source and detection fiber. The distance between their position is 1.5 cm.

Finally, we performed the optical measurement of the neck and showed the measurement settings in Figure 4.7. First, TRS-80 emitted the near infrared pulsed lights at 763 nm, 801 nm, 836 nm at S1, which is the source position on the neck in Figure 4.6. And TRS-80 detected the lights transmitted through the neck at all eight detection positions (from D1 to D8 in Figure 4.6) simultaneously. The acquired time of each source position was

10 s. Next, TRS-80 emitted the lights at S2, and detected for 10 s in the same manner. TRS-80 repeated the measurement from S1 to S7. The total measurement time was about 120 s including the switching time of the optical switch and the time for adjusting the attenuators. Consequently, forty-nine TOF distributions with the average photon counting rate of more than 115,000 count/s and the maximum count over 2,000 were used for image reconstruction. The remaining seven TOF distributions measured at seven source-detector pairs (S2-D1, S2-D6, S3-D3, S3-D8, S5-D1, S5-D6, and S7-D6) were excluded from the image reconstruction because of insufficient SNR.

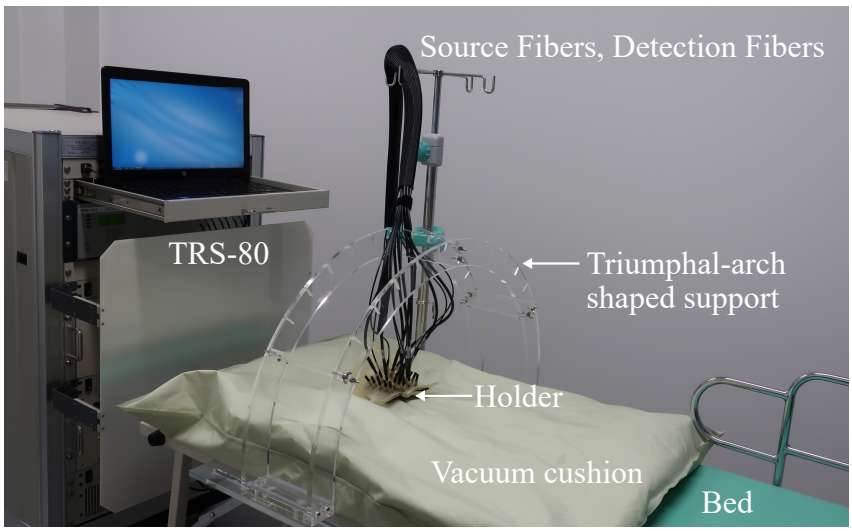

Figure 4.7. Measurement setting in the neck measurement.

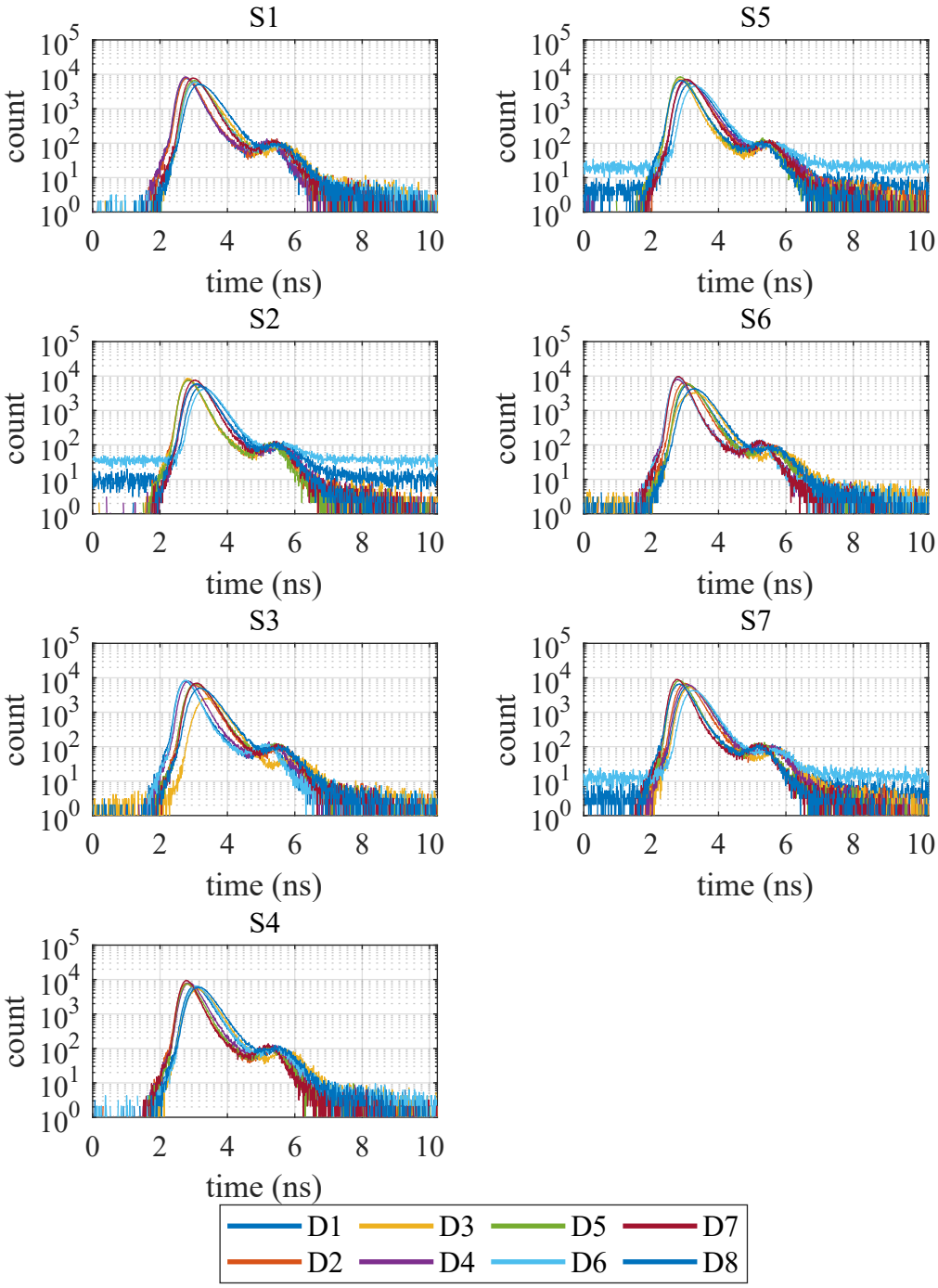

Figure 4.8. Time-of-flight distributions in the neck at 763 nm. S# and D# denotes the number of the source and detection fiber, respectively.

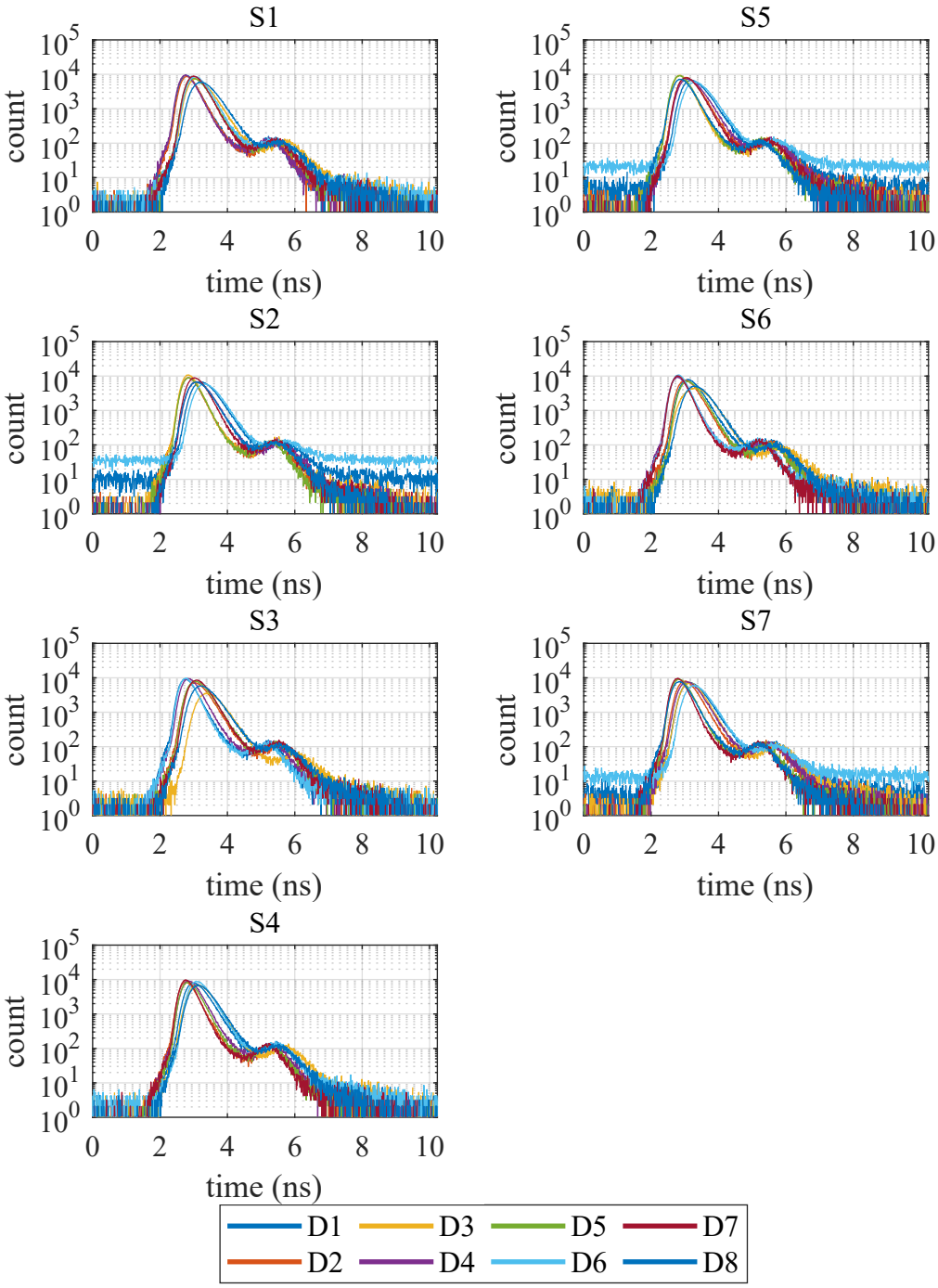

Figure 4.9. Time-of-flight distributions in the neck at 801 nm. S# and D# denotes the number of the source and detection fiber, respectively.

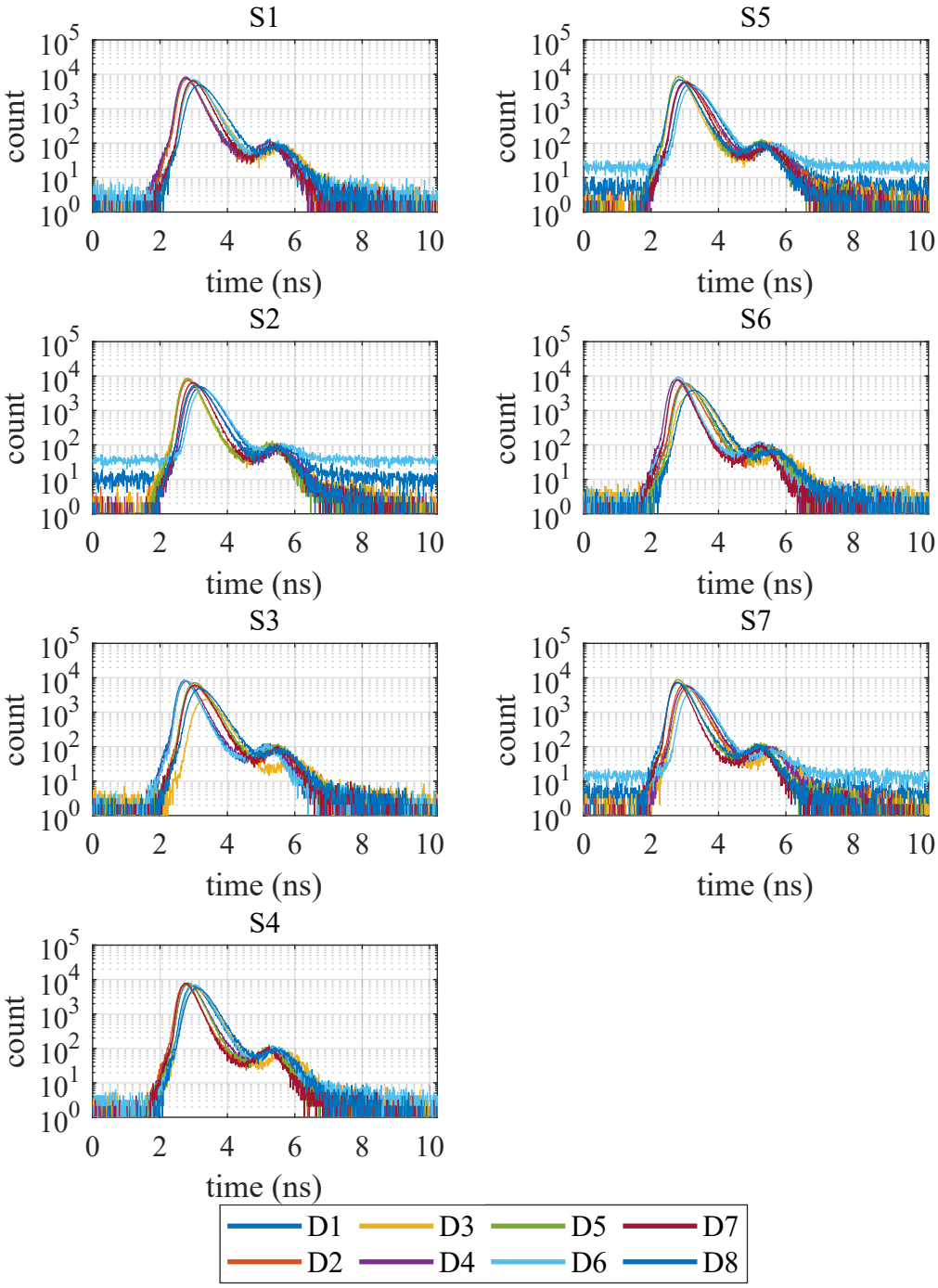

Figure 4.10. Time-of-flight distributions in the neck at 836 nm. S# and D# denotes the number of the source and detection fiber, respectively.

4.1.6 Image reconstruction of the neck

We performed the image reconstructions of absorption coefficients at each wavelength (763 nm, 801 nm, and 836 nm). Seven source-detection pairs of the TOF distribution were excluded for further analysis due to insufficient SNR. The parameter $H_{i,j} = 0$ or 1 in Equation (2.25) controls whether certain source-detection pair of the TOF distribution is available or not. When (i, j) is (2, 1), (2, 6), (3, 3), (3, 8), (5, 1), (5, 6), and (7, 6), $H_{i,j} = 0$. And when (i, j) is others, $H_{i,j} = 1$.

In the initial condition, we set the hyper parameter $\tau = 50$. The initial absorption and reduced scattering coefficients are $\mu_{\mathrm{a}} = 0.027\,\mathrm{mm}^{-1}$ and $\mu'_{\mathrm{s}} = 0.95\,\mathrm{mm}^{-1}$ at all nodes in the grids shown in Figures 4.5B,C. The initial values were taken from [14]. The refractive index of the neck assumed to be 1.37.

4.1.7 Calculation of tissue oxygen saturation

The thyroid is a richly vascular organ and consists of a large number of thyroid follicles of which walls are made up of a large number of cells, mainly follicular cells. Follicles are filled with colloid (thyroglobulin). Thyroglobulin contributes to the absorption coefficients in the three wavelengths used in this study [33]. Since, however, it is difficult to estimate its contributions quantitatively, treating thyroglobulin as water, it is assumed that Hb and water are main chromophores of the thyroid.

Here is a brief explanation how to calculate tissue oxygen saturation $\mathrm{StO_2}$ from the absorption coefficients at 763 nm, 801 nm, and 836 nm ($\mu_{a,763\,\mathrm{nm}}$, $\mu_{a,801\,\mathrm{nm}}$, and $\mu_{a,836\,\mathrm{nm}}$). The value of $\mathrm{StO_2}$ is given as

$$\mathrm{StO_2} = \frac{[\text{oxy-Hb}]}{[\text{oxy-Hb}] + [\text{deoxy-Hb}]}, \tag{4.1}$$

where [oxy-Hb] and [deoxy-Hb] are the molar concentration of tissue oxygenated hemoglobin

(oxy-Hb) and deoxygenated hemoglobin (deoxy-Hb), respectively. The [oxy-Hb] and [deoxy-Hb] are calculated from the $\mu_{a,763\,\mathrm{nm}}$, $\mu_{a,801\,\mathrm{nm}}$, and $\mu_{a,836\,\mathrm{nm}}$ since the molar extinction coefficients $\varepsilon_{\text{oxy-Hb}}$ and $\varepsilon_{\text{deoxy-Hb}}$ of oxy-Hb and deoxy-Hb have been already known. Moreover, the reconstructed values ($\mu_{a,763\,\mathrm{nm}}$, $\mu_{a,801\,\mathrm{nm}}$, and $\mu_{a,836\,\mathrm{nm}}$) include not only the absorption of oxy-Hb and deoxy-Hb, but also water (Figures 4.11, 4.12). Therefore, the form to calculated the [oxy-Hb] and [deoxy-Hb] is given as

$$\begin{cases} \varepsilon_{\text{oxy-Hb},763\,\mathrm{nm}}[\text{oxy-Hb}] + \varepsilon_{\text{deoxy-Hb},763\,\mathrm{nm}}[\text{deoxy-Hb}] & = \mu_{a,763\,\mathrm{nm}} - \eta\mu_{a,\text{Water},763\,\mathrm{nm}}, \\ \varepsilon_{\text{oxy-Hb},801\,\mathrm{nm}}[\text{oxy-Hb}] + \varepsilon_{\text{deoxy-Hb},801\,\mathrm{nm}}[\text{deoxy-Hb}] & = \mu_{a,801\,\mathrm{nm}} - \eta\mu_{a\text{Water},801\,\mathrm{nm}}, \\ \varepsilon_{\text{oxy-Hb},836\,\mathrm{nm}}[\text{oxy-Hb}] + \varepsilon_{\text{deoxy-Hb},836\,\mathrm{nm}}[\text{deoxy-Hb}] & = \mu_{a,836\,\mathrm{nm}} - \eta\mu_{a\text{Water},836\,\mathrm{nm}}, \end{cases} \tag{4.2}$$

where η is the contribution (percentage) of water in the absorption coefficient. In the thyroid, we assumed the $\eta = 78\%$ [34]. Figure 4.11 shows the molar extinction coefficients of oxy-Hb and deoxy-Hb ($\varepsilon_{\text{oxy-Hb}}$ and $\varepsilon_{\text{deoxy-Hb}}$), which are referred to [35]. Figure 4.12 shows $\mu_{a\text{Water}}$ in the near infrared region [36].

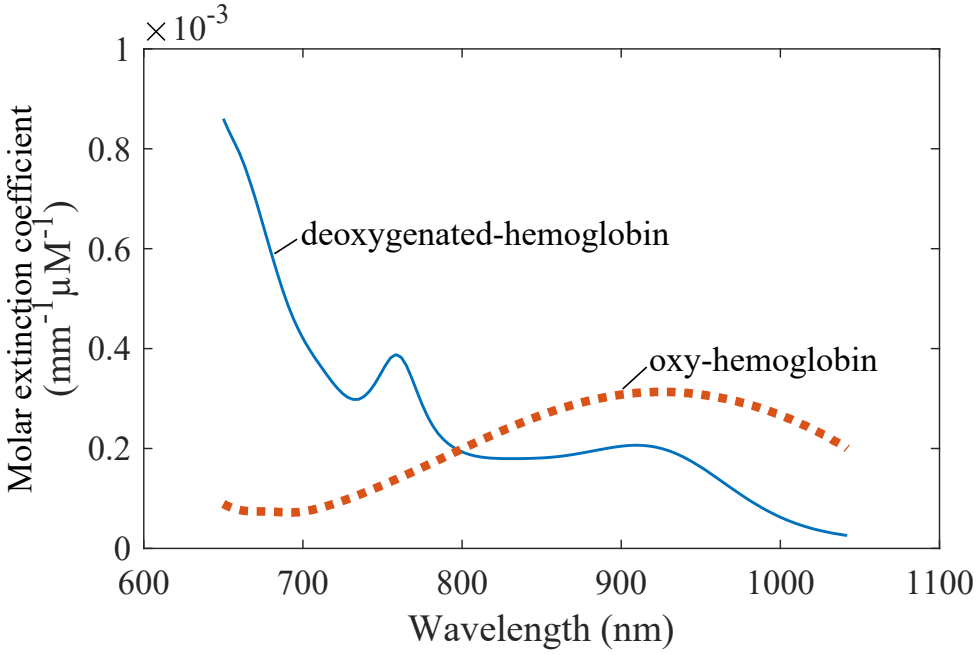

Figure 4.11. Molar extinction coefficients of oxygenated-hemoglobin (blue line) and deoxygenated-hemoglobin (dashed orange line) from 650 nm to 1042 nm [35].

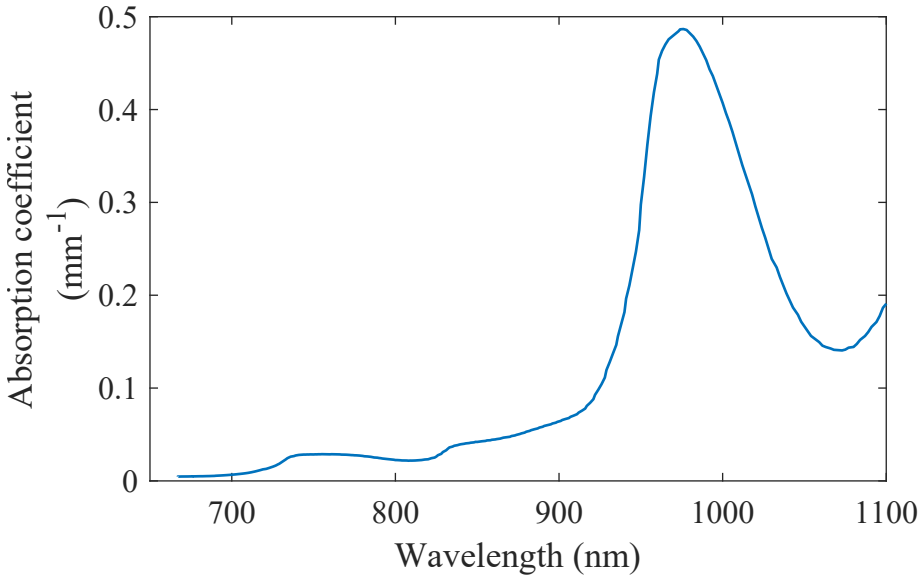

Figure 4.12. Absorption coefficient of water from 667 nm to 1100 nm [36].

4.2 Tomographic images of the human neck

4.2.1 Tomographic images with the trachea-tissue boundary grid

Figures 4.13-4.15 show horizontal sections of NIROT images of μ_a at 763 nm, 801 nm, 836 nm , respectively. These Figures are at the 15th iteration by the trachea-tissue boundary grid (Figure 4.5B) at different slices. The NIROT images are shown on the T2-weighted MR images. Figures 4.13B, 4.14B, 4.15B show the section at the middle of the isthmus of the thyroid. Figures 4.13A, 4.14A, 4.15A are sections 3 mm above the middle of the isthmus of the thyroid. Figures 4.13C, 4.14C, 4.15C are sections 3 mm below the middle of the isthmus of the thyroid. The trachea-tissue boundary grid region is shown in Figures 4.13-4.15 (dashed white line). The color bar shows the reconstructed μ_a values. In Figures 4.13-4.15, the outline of the thyroid is denoted by white lines. The shape of the thyroid in Figure 4.14, where the μ_a values were about 0.075 mm^{-1}, is reconstructed in the NIROT images, while the position of the reconstructed thyroid shifts slightly towards the skin. The μ_a values of the background tissue (muscles) were about 0.02 mm^{-1}. Although the right

IJV was included in the grid, it was not reconstructed in the image because the optical fibers were arranged far from the IJV. Actually, the μ_a values in the IJV were not updated but remained the initial ones (0.027 mm^{-1}) during the iteration process.

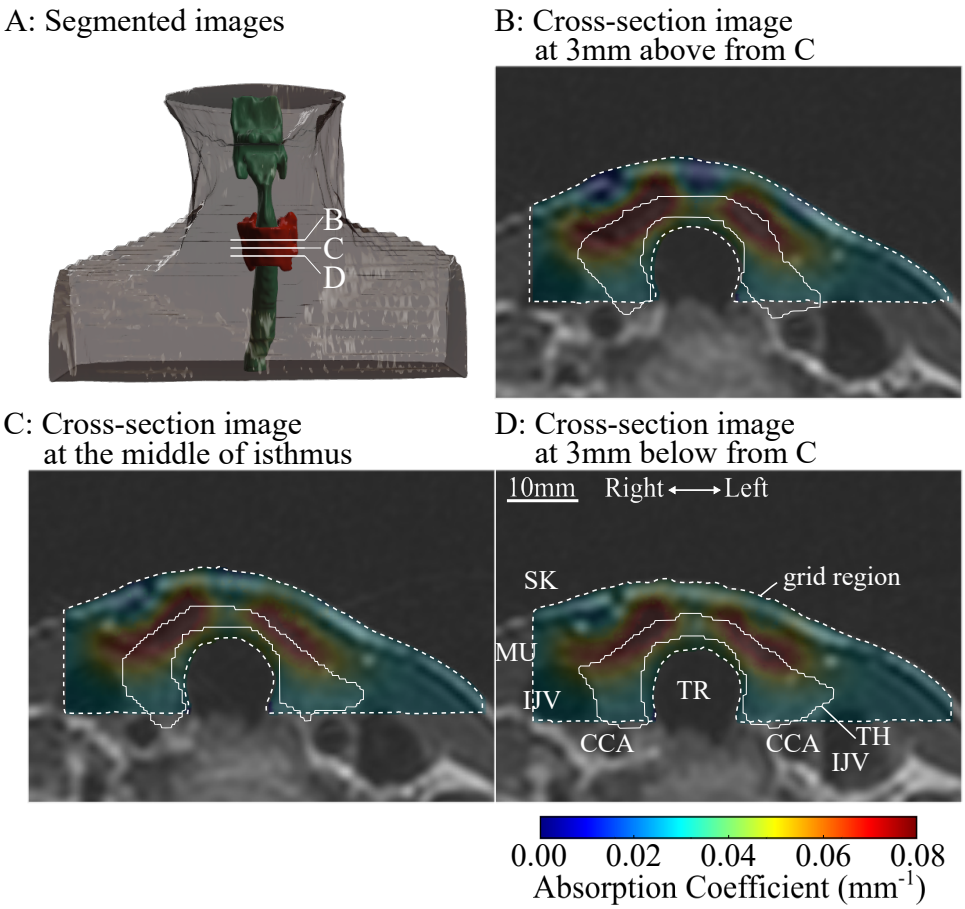

Figure 4.13. Tomographic images of the absorption coefficient at 763 nm by the trachea-tissue boundary grid on horizontal sections at (A) 3 mm above the middle of the thyroid isthmus, (B) the middle of the thyroid isthmus, and (C) 3 mm below the middle of the thyroid isthmus. The thyroid and the grid region are denoted by the white line and the dashed white line, respectively. Positions of the muscle (MU), internal jugular vein (IJV), common carotid artery (CCA), trachea (TR), thyroid (TH), and skin (SK) are shown in (D).

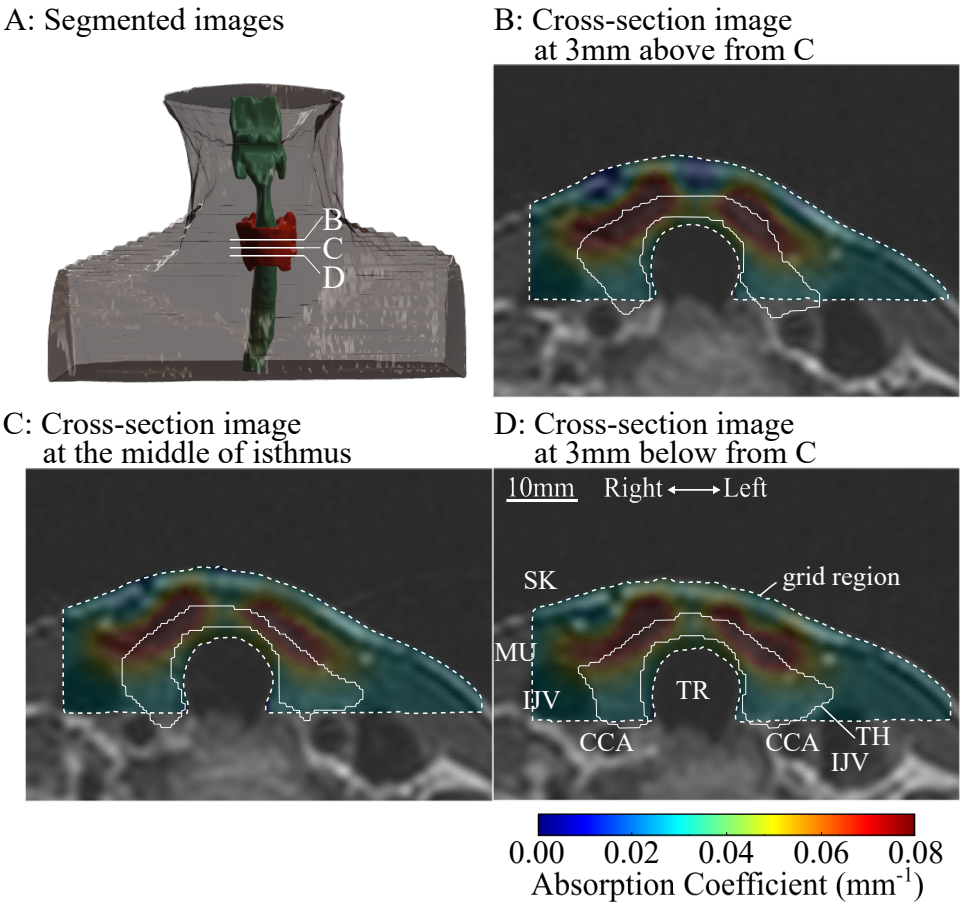

Figure 4.14. Tomographic images of the absorption coefficient at 801 nm by the trachea-tissue boundary grid on horizontal sections at (A) 3 mm above the middle of the thyroid isthmus, (B) the middle of the thyroid isthmus, and (C) 3 mm below the middle of the thyroid isthmus. The thyroid and the grid region are denoted by the white line and the dashed white line, respectively. Positions of the muscle (MU), internal jugular vein (IJV), common carotid artery (CCA), trachea (TR), thyroid (TH), and skin (SK) are shown in (D).

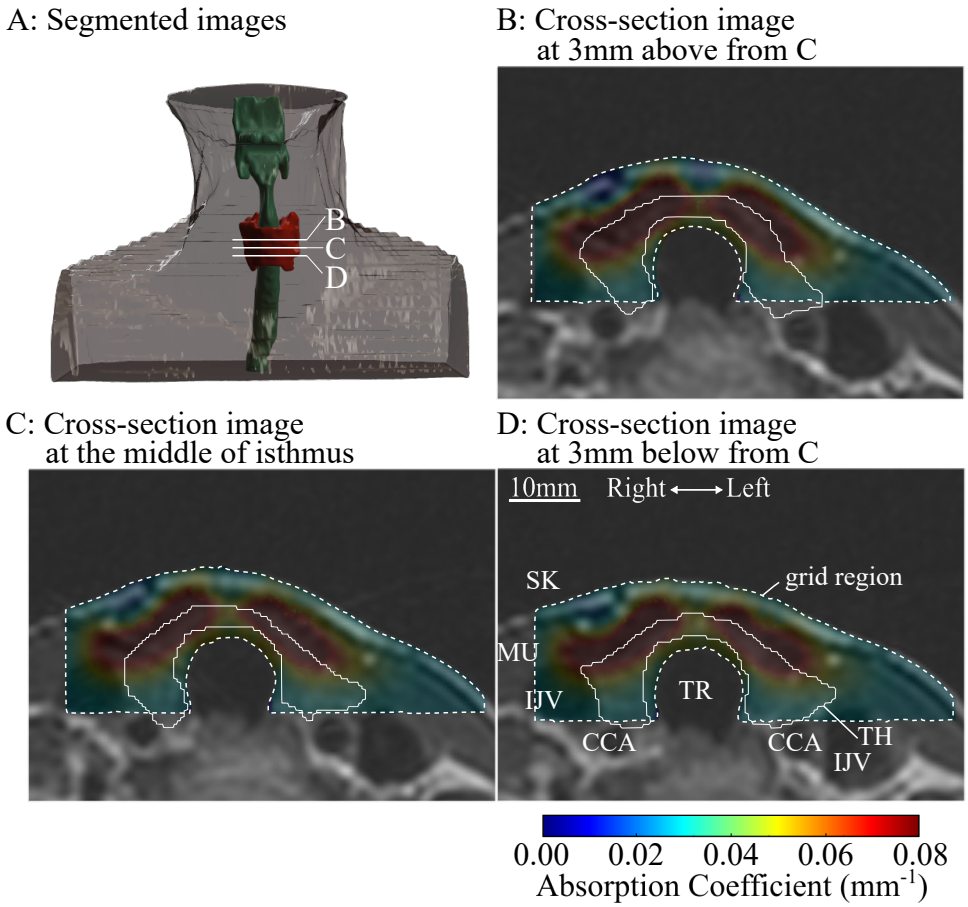

Figure 4.15. Tomographic images of the absorption coefficient at 836 nm by the trachea-tissue boundary grid on horizontal sections at (A) 3 mm above the middle of the thyroid isthmus, (B) the middle of the thyroid isthmus, and (C) 3 mm below the middle of the thyroid isthmus. The thyroid and the grid region are denoted by the white line and the dashed white line, respectively. Positions of the muscle (MU), internal jugular vein (IJV), common carotid artery (CCA), trachea (TR), thyroid (TH), and skin (SK) are shown in (D).

Figure 4.16 shows tomographic images of StO_2 calculated from the μ_a values at the three wavelengths. There are high StO_2 (around 90%) regions were observed, which corresponded approximately to the reconstructed thyroid regions in Figures 4.13-4.15. The StO_2 in the background tissues, mainly muscles, was around 65%. Although the μ_a values at the isthmus of the thyroid were much smaller than those in the bilateral lobes, the StO_2 distribution was relatively homogeneous and StO_2 of the thyroid was 82% to 92%. As a result, the isthmus of the thyroid was more clearly imaged compared to Figures 4.13-4.15.

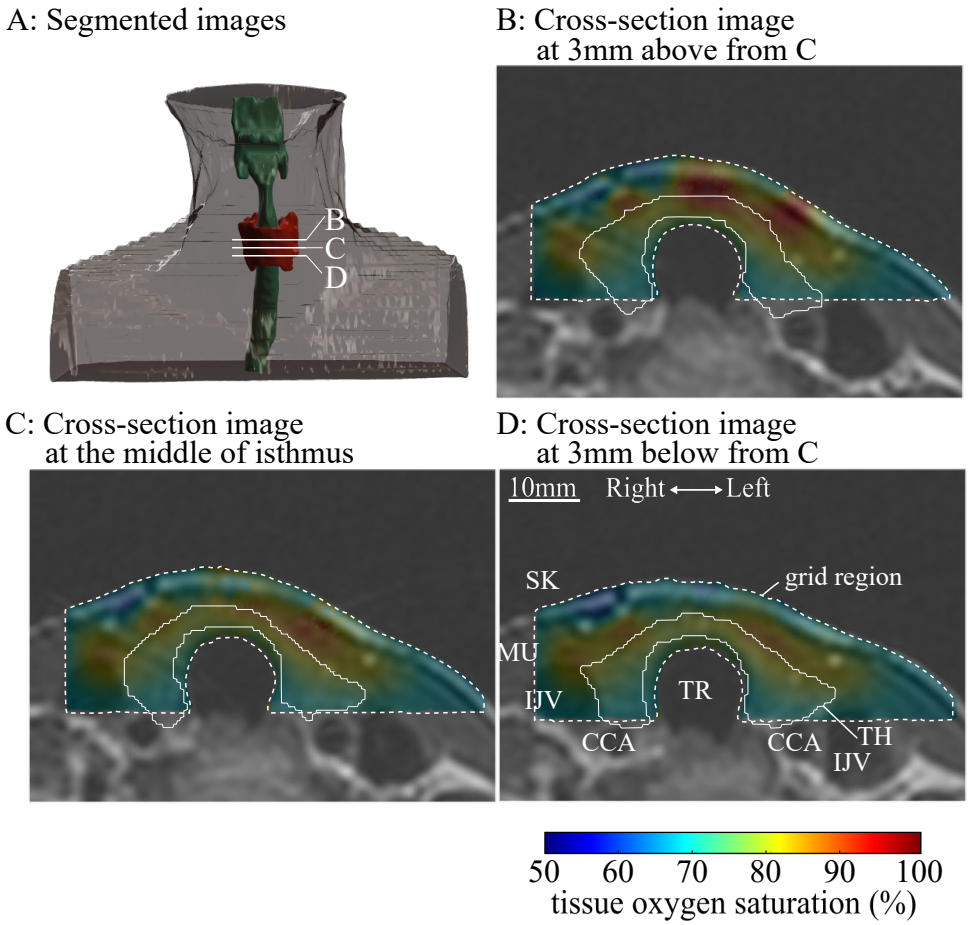

Figure 4.16. Tomographic images of StO_2 by the trachea-tissue boundary grid on horizontal sections at (A) 3 mm above the middle of the thyroid isthmus, (B) the middle of the thyroid isthmus, and (C) 3 mm below the middle of the thyroid isthmus. The thyroid and the grid region are denoted by the white line and the dashed white line, respectively. Positions of the muscle (MU), internal jugular vein (IJV), common carotid artery (CCA), trachea (TR), thyroid (TH), and skin (SK) are shown in (D).

4.2.2 Tomographic images with the homogeneous grid

Figures 4.17-4.19 show horizontal sections of NIROT images of μ_a at 763 nm, 801 nm, and 836 nm, respectively. These figures are the image at the 35th iteration by the homogeneous grid (Figure 4.5C). Although the existence of the thyroid may be read from these reconstructed images, the shape of the thyroid is not correctly reconstructed.

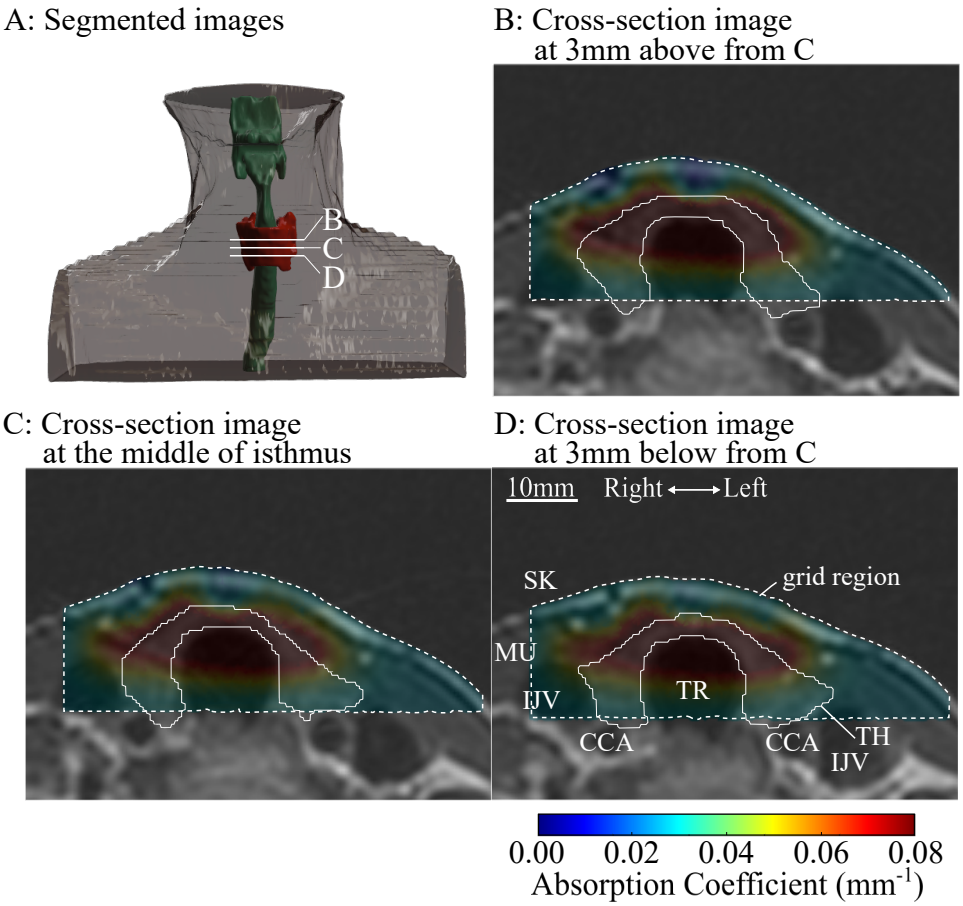

Figure 4.17. Tomographic images of the absorption coefficient at 763 nm by the trachea homogeneous grid on horizontal sections at (A) 3 mm above the middle of the thyroid isthmus, (B) the middle of the thyroid isthmus, and (C) 3 mm below the middle of the thyroid isthmus. The thyroid and the grid region are denoted by the white line and the dashed white line, respectively. Positions of the muscle (MU), internal jugular vein (IJV), common carotid artery (CCA), trachea (TR), thyroid (TH), and skin (SK) are shown in (D).

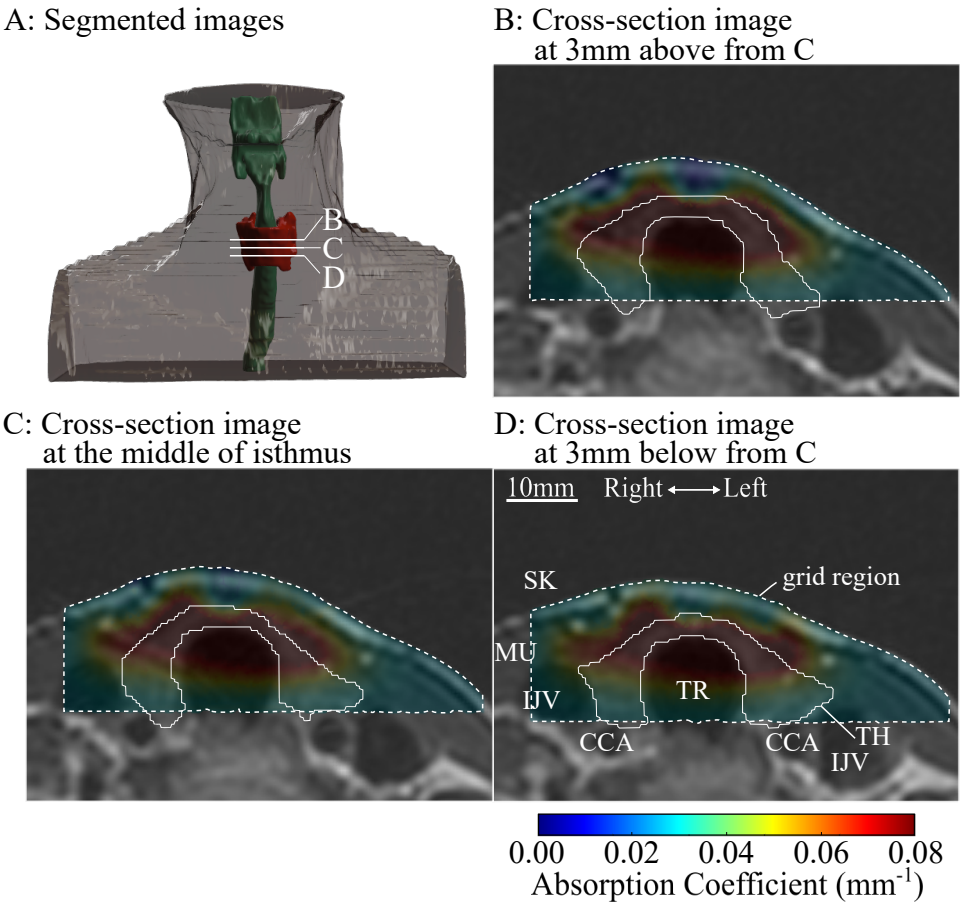

Figure 4.18. Tomographic images of the absorption coefficient at 801 nm by the trachea homogeneous grid on horizontal sections at (A) 3 mm above the middle of the thyroid isthmus, (B) the middle of the thyroid isthmus, and (C) 3 mm below the middle of the thyroid isthmus. The thyroid and the grid region are denoted by the white line and the dashed white line, respectively. Positions of the muscle (MU), internal jugular vein (IJV), common carotid artery (CCA), trachea (TR), thyroid (TH), and skin (SK) are shown in (D).

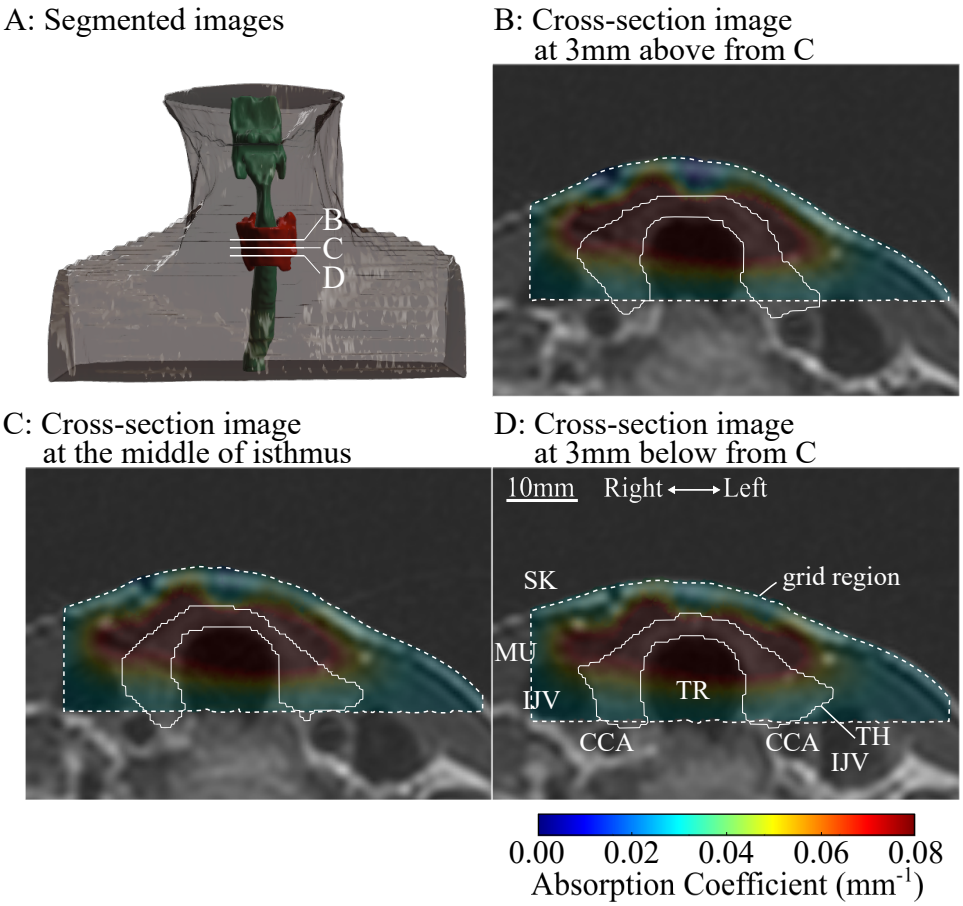

Figure 4.19. Tomographic images of the absorption coefficient at 836 nm by the trachea homogeneous grid on horizontal sections at (A) 3 mm above the middle of the thyroid isthmus, (B) the middle of the thyroid isthmus, and (C) 3 mm below the middle of the thyroid isthmus. The thyroid and the grid region are denoted by the white line and the dashed white line, respectively. Positions of the muscle (MU), internal jugular vein (IJV), common carotid artery (CCA), trachea (TR), thyroid (TH), and skin (SK) are shown in (D).

4.3 Discussion

This is the first study reporting the reconstructing the spatial distribution of μ_a and StO_2 in the human whole thyroid with NIROT. The neck is composed of various organs and the refractive index inside the neck is heterogeneous. Especially, between the tissue and the trachea there is a strong refractive index mismatch. So far, it has been a seriously nontrivial question whether the thyroid can be imaged accurately by NIROT, however in this paper, we have shown that the whole shape of the thyroid can be reconstructed if the grid for

the calculations excludes the trachea void region. However, the reentrance of light which propagates through the trachea was not taken into account in the present study. It is expected that reconstructed images will be improved if the reentrant light is taken into account [32].

In this paper, the thyroid was reconstructed at a position closer to the skin than its actual position. This can be understood from the structure of the objective function used in our numerical reconstruction. Since the diffuse fluence of near-infrared light decays exponentially with increased depth in biological tissue, measurement sensitivity decreases along the depth direction. Spatially variant regularization has been proposed to compensate for this [37], [38]. However, we did not employ depth-dependent regularization, which is one reason why the position of the reconstructed thyroid shifted slightly towards the skin.

The obtained μ_a values in the present study were much larger than the published values that have been obtained with time-domain measurements. In a study preceding this, the μ_a values were estimated by fitting the TOF distribution derived from the analytical solution of the DE for a semi-infinite homogeneous medium to the measured TOF distribution [14]. However, it is hardly acceptable to assume the human neck to be homogeneous, and the thyroid is covered by muscles, it is likely that the published μ_a values should be partly attributed to the μ_a of muscle tissue. Here the present study indicates the possibility of selectively measuring the μ_a of the thyroid, and the μ_a values in the present paper may also be assumed to deviate from the true situation, to some extent because the reduced scattering coefficient was not updated during the iterations of the nonlinear conjugate-gradient method. An accurate quantification of μ_a requires the simultaneous reconstruction of both μ_a and μ_s' [39], which will be subjected to artifacts caused by cross-talk between the two parameters. To suppress cross-talk artifacts, the use of multiple data sets for the objective functions, such as a combination of skew and Laplace transform of the TOF distribution (Equation (2.3)), has been proposed [40].

The present NIROT is still insufficient to measure optical properties and hemoglobin concentrations quantitatively, the map of StO_2 (Figure 4.16) indicates that the thyroid is

distinguishable from the background tissue (muscles): the StO_2 of the thyroid was around 90%, while that of the muscles was around 65%. The reconstructed thyroid StO2 was higher than expected, which was close to arterial blood oxygen saturation. This might be attributable to the fact that the contribution of thyroglobulin to the absorption coefficient values was not considered. However, the thyroid has well-developed capillaries and its color is bright red like arterial blood, which supports the present results. A high StO_2 is the more favorable to detecting cancer hypoxia because the difference in StO_2 between normal and cancerous tissue is thought to be larger than that when the StO_2 of the thyroid is the lower. Cytochrome c oxidase is a more sensitive indicator for cell hypoxia than StO_2 [17]. However, TRS-80 with three wavelengths cannot measure the redox state of cyt. ox. and an instrument with four or more wavelengths will be required.

Regarding treatment of thyroid diseases, it is important that the shape and size of the thyroid are tracked over time, which can be conducted by ultrasound scan. Hence, several 2-dimensional (2D) segmentation algorithms for thyroid ultrasound images have been developed, and 3D segmentation is now possible [41], [42]. Three-dimensional visualizations of the thyroid are also crucial for surgical intervention [43]. Recent advances in segmentation and image processing techniques have enabled 3D thyroid reconstruction from 2D ultrasound slices [44], [45].

To detect early-stage FTC, of which size is small, improvements of spatial resolution and quantitative measurements are required. As described earlier, for this aim, multiple data types of the TOF distribution need to be used and simultaneous reconstruction of the absorption and reduced scattering coefficients should be performed.

The present study has the three main limitations described above, but it has still paved the way to functional optical imaging of the human thyroid. Moreover, in the future, it had better demonstrates that changes due to FTC or other forms of thyroid cancer are detectable in tomographic images in the clinical study. Combination of NIROT with ultrasound scan will be complementary in the course of diagnosis and treatment of thyroid cancers.

Chapter 5

Conclusions

We developed the NIROT for thyroid diagnosis and demonstrated the clinical study of one healthy person. This clinical study presents the *in situ* tomographic images of absorption coefficient and tissue oxygen saturation in the neck. The whole shape of the thyroid can be reconstructed if the grid for the numerical calculations excludes the trachea void region.

To improve the quantity of the tomographic images, we suggested three followings. First is to estimate the value of the absorption coefficient by the simultaneous reconstruction of absorption and reduced scattering coefficients. Second is to calculate the reentrant light from the void region of the trachea in light propagation model. Third is to add the depth dependent regularization term in the object function. These leads to quantitative absorption coefficient and tissue oxygen saturation imaging of thyroid.

This study needs to evaluate additional phantom and clinical studies to validate whether the tomographic images are correctly reconstructing thyroid metabolism. We have to demonstrate the changes FTC or other forms of thyroid cancer are detectable in the near infrared optical tomography in the future.

It has been a seriously nontrivial question whether the thyroid can be imaged accurately by NIROT, however in this paper, we have shown that the whole shape of the thyroid. This

would make NIROT available for use in thyroid cancer diagnosis. It can be expected that NIROT has the potential to visualize the tissue hypoxia of the thyroid cancer.

Appendix A

Near infrared light propagation in biological tissues

A.1 Light scattering and absorption

Near infrared light propagates randomly scattered and absorbed in biological tissues. The scattering and the absorption is defined followings. Since it is difficult to know the size and shape of all scattering and absorbing particles in biological tissues, the statistical approach is used. Consider a situation in which there are N_s scattered particles with an average radius of R_s in a volume V in Figure A1.

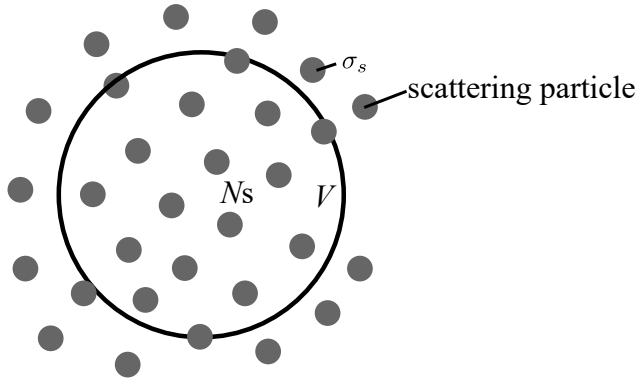

Figure A1. Schematic view of the situation in which there are N_s scattered particles with a scattering cross section σ_s in a volume V.

Let $\sigma_s(R)$ be the scattering cross section of a single scattered particle. $\xi_s(R)$ is a probability distribution of scattered particles with a radius of R. $\xi_s(R)\,dR$ represents the number of scattered particles of a radius of dR in a unit volume, and it satisfies the relationship given as

$$\int_0^\infty \xi_s(R)\,dR = \frac{N_s}{V}. \tag{A.1}$$

The scattering coefficient $\mu_s\left(\mathrm{mm}^{-1}\right)$ is defined as the total cross section per a unit volume, and it is given as

$$\mu_s = \int_0^\infty \xi_s(R)\,\sigma_s(R)\,dR. \tag{A.2}$$

If the radius of all the scattered particles are the same (R_s), $\xi_s(R) = \delta(R - R_s)\,N_s/V$ and μ_s is given as

$$\mu_s = \sigma_s N_s/V. \tag{A.3}$$

In Figure A2, the probability of scattering from a direction $\hat{\mathbf{s}}'$ to a direction $\hat{\mathbf{s}}$ is termed as the phase function $p(\hat{\mathbf{s}}, \hat{\mathbf{s}}')$, of which the integration in all angle (4π) is given as

$$\int_{4\pi} p(\hat{\mathbf{s}}, \hat{\mathbf{s}}')\,d\omega = 1, \tag{A.4}$$

where the solid angle $d\omega = \sin\theta\,d\theta\,d\varphi$ is shown in Figure A3.

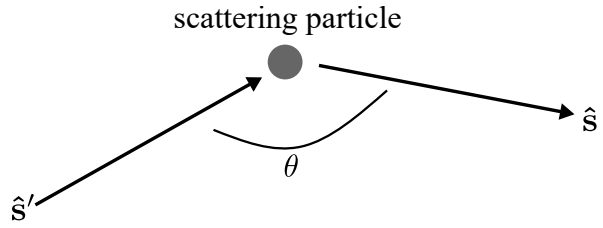

Figure A2. Schematic view of the light scattered from a direction of $\hat{\mathbf{s}}'$ to a direction of $\hat{\mathbf{s}}$.

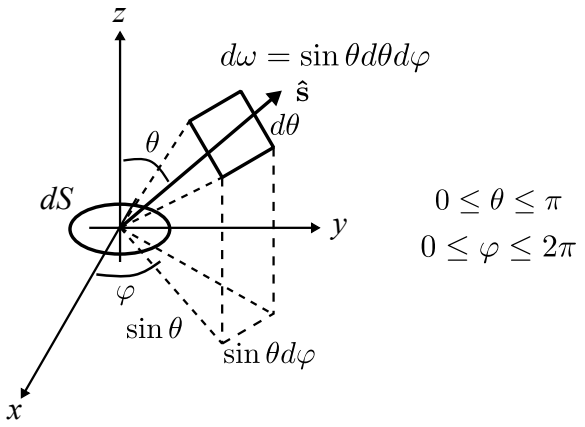

Figure A3. Schematic view of the solid angle.

The anisotropy of the phase function is expressed by the anisotropic factor

$$\begin{aligned} g &= <\cos\theta>, \\ &= <\hat{\mathbf{s}}\cdot\hat{\mathbf{s}}'>, \\ &= \int_{4\pi} (\hat{\mathbf{s}}\cdot\hat{\mathbf{s}}')\, p\,(\hat{\mathbf{s}},\hat{\mathbf{s}}')\, d\omega, \qquad (-1 \leq g \leq 1)\,, \end{aligned} \tag{A.5}$$

where < > denotes the average. The anisotoropic factor describes the full forward scattering when $g = 1$, isotropic scattering when $g = 0$, and full back scattering when $g = -1$. Generally, in the biological tissues, the typical value of g is range from 0.8 to 0.95 [46]. To express anisotropic scattering phenomena, the reduced scattering coefficient $\mu_{\mathrm{s}}'\left(\mathrm{mm}^{-1}\right)$ is given as

$$\mu_{\mathrm{s}}' = \mu_{\mathrm{s}}\,(1-g)\,. \tag{A.6}$$

The absorption coefficient is defined as the same manner as scattering. Consider a situation in which there are N_{a} absorbed particles with an average radius of R_{a} in a volume V. Let $\sigma_{\mathrm{a}}(R)$ be the absorption cross section of a single absorbed particle. $\xi_{\mathrm{a}}(R)$ is a probability distribution of absorbed particles with a radius of R. $\xi_{\mathrm{a}}(R)\,dR$ represents the number of absorbed particles of a radius of dR in a unit volume, and it satisfies the

relationship given as

$$\int_0^\infty \xi_\mathrm{a}(R)\, dR = \frac{N_\mathrm{a}}{V}. \tag{A.7}$$

The absorption coefficient $\mu_\mathrm{a}\left(\mathrm{mm}^{-1}\right)$ is defined as the total cross section per a unit volume, it is given as

$$\mu_\mathrm{a} = \int_0^\infty \xi_\mathrm{a}(R)\, \sigma_\mathrm{a}(R)\, dR, \tag{A.8}$$

where $\mu_\mathrm{a}\left(\mathrm{mm}^{-1}\right)$ is termed as absorption coefficient. If the radius of all the absorbed particles are the same (R_a), $\xi_\mathrm{a}(R) = \delta(R - R_\mathrm{a})\, N_\mathrm{a}/V$ and μ_a is given as

$$\mu_\mathrm{a} = \sigma_\mathrm{a} N_\mathrm{a}/V. \tag{A.9}$$

The typical value of μ_s' is about two orders of magnitude larger than that of μ_a in biological tissues. The transport mean free path L is given as $L = 1/\left(\mu_\mathrm{a} + \mu_\mathrm{s}'\right)$. As an example, $L \approx 1\,\mathrm{mm}$ when $\mu_\mathrm{a} = 0.01\,\mathrm{mm}^{-1}$ and $\mu_\mathrm{s}' = 1.0\,\mathrm{mm}^{-1}$. If light travel distance is beyond the L, the light scatters many times, which is described by radiative transport equation.

A.2 Specific intensity, fluence rate, and flux

The amount of power of light that passes through the small area dS in a direction of $\hat{\mathbf{s}}$ at the position $\mathbf{r}$ within a unit solid angle at a certain time t is termed as specific intensity $I\left(\mathrm{J}\cdot\mathrm{s}^{-1}\cdot\mathrm{mm}^{-2}\cdot\mathrm{sr}^{-1}\right)$. In Figure A4, the radiant energy propagating from a small area dS in a direction of $\hat{\mathbf{s}}$ in time of dt is given as

$$I(\mathbf{r}, \hat{\mathbf{s}}, t)\; dS\, d\omega\, dt, \tag{A.10}$$

where $\hat{\mathbf{s}}$ is a unit direction vector in Figure A5 and $d\omega$ is the solid angle in Figure A3.

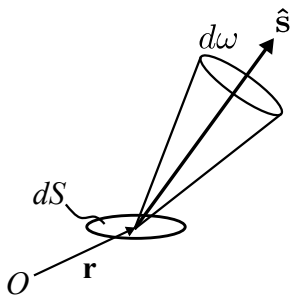

Figure A4. Representation of the radiant energy propagating from a small area dS in the $\hat{\mathbf{s}}$ direction over a time interval of dt.

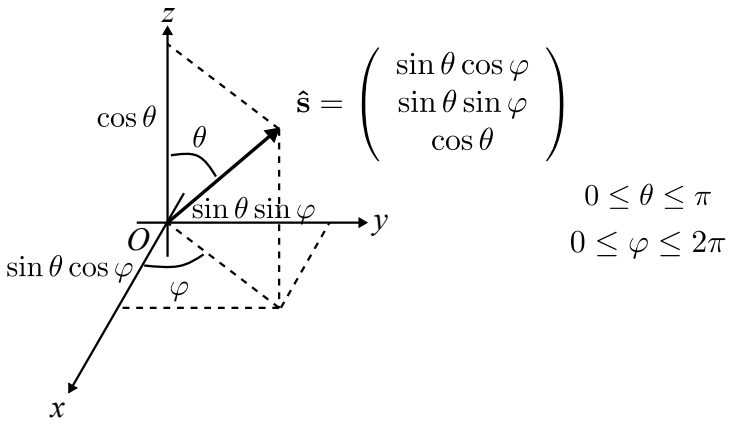

Figure A5. Representation of an unit direction vector $\hat{\mathbf{s}}$.

The integration of the specific intensity over all angle (4π) is termed as fluence rate $\phi\left(\mathrm{J}\cdot\mathrm{s}^{-1}\cdot\mathrm{mm}^{-2}\right)$, which is given as

$$\phi\left(\mathbf{r},t\right)=\int_{4\pi} I\left(\mathbf{r},\hat{\mathbf{s}},t\right)d\omega. \tag{A.11}$$

However, there is no information about the direction that the light flows on average. The overall energy flow is termed as flux $\mathbf{J}\left(\mathrm{J}\cdot\mathrm{s}^{-1}\cdot\mathrm{mm}^{-2}\right)$ as

$$\mathbf{J}=\int_{4\pi} I\left(\mathbf{r},\hat{\mathbf{s}},t\right)\hat{\mathbf{s}}\,d\omega. \tag{A.12}$$

Consider a flux J_{n} passing perpendicular to a small area dS in Figure A6. Let $\hat{\mathbf{n}}$ be the unit vector perpendicular to dS. J_{n} is the sum of $J_{\mathrm{n+}}$ passing in a direction toward + and

J_{n-} passing in a direction toward –. $(2\pi+)$ and $(2\pi-)$ express the integration interval of $0 \leq \theta \leq \pi/2$ and $\pi/2 \leq \theta \leq \pi$, respectively.

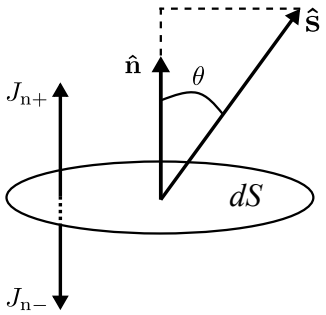

Figure A6. Schematic view of the flux passing perpendicular to a small area dS. J_{n+} and J_{n-} is the flux passing perpendicular to the small area dS in the direction toward + and the direction toward –, respectively.

Thus, the flux J_n is

$$\begin{aligned}
J_n &= J_{n+} - J_{n-}, \\
&= \int_{2\pi+} I(\mathbf{r}, \hat{\mathbf{s}}, t)\, \hat{\mathbf{s}} \cdot \hat{\mathbf{n}}\, d\omega - \int_{2\pi-} I(\mathbf{r}, \hat{\mathbf{s}}, t)\, \hat{\mathbf{s}} \cdot (-\hat{\mathbf{n}})\, d\omega, \\
&= \int_0^{2\pi} \int_0^{\pi/2} I(\mathbf{r}, \hat{\mathbf{s}}, t)\, \hat{\mathbf{s}} \cdot \hat{\mathbf{n}}\, \sin\theta\, d\theta\, d\varphi \\
&\quad - \int_0^{2\pi} \int_{\pi/2}^{\pi} I(\mathbf{r}, \hat{\mathbf{s}}, t)\, \hat{\mathbf{s}} \cdot (-\hat{\mathbf{n}}) \sin\theta\, d\theta\, d\varphi, \\
&= \int_0^{2\pi} \int_0^{\pi} I(\mathbf{r}, \hat{\mathbf{s}}, t)\, \hat{\mathbf{s}} \cdot \hat{\mathbf{n}}\, \sin\theta\, d\theta\, d\varphi, \\
&= \int_{4\pi} I(\mathbf{r}, \hat{\mathbf{s}}, t)\, \hat{\mathbf{s}} \cdot \hat{\mathbf{n}}\, d\omega, \\
&= \mathbf{J} \cdot \hat{\mathbf{n}}.
\end{aligned} \tag{A.13}$$

A.3 Radiative transport equation

Consider the energy balance of light passing through a thin slab within Ω, bounded by a surface $\partial\Omega$ in Figure A7.

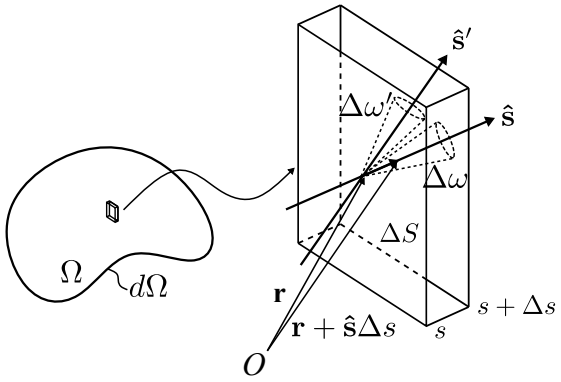

Figure A7. Schematic view of the light passing through a thin slab in a direction of $\hat{\mathbf{s}}$ within Ω, bounded by a surface $\partial\Omega$.

The amount of light that passed through the thin slab is given as

$$\begin{aligned} I\left(\mathbf{r}+\hat{\mathbf{s}}\Delta s, \hat{\mathbf{s}}, t+\Delta t\right) \Delta S \Delta\omega \Delta t = I\left(\mathbf{r}, \hat{\mathbf{s}}, t\right) \Delta S \Delta\omega \Delta t \\ - \left(\mu_{\mathrm{a}} \Delta s + \mu_{\mathrm{s}} \Delta s\right) I\left(\mathbf{r}, \hat{\mathbf{s}}, t\right) \Delta S \Delta\omega \Delta t \\ + \mu_{\mathrm{s}} \Delta s \sum_{\Delta\omega'} I\left(\mathbf{r}, \hat{\mathbf{s}}', t\right) p\left(\hat{\mathbf{s}}, \hat{\mathbf{s}}'\right) \Delta S \Delta\omega \Delta t \\ + \varepsilon\left(\mathbf{r}, \hat{\mathbf{s}}, t\right) \Delta S \Delta\omega \Delta t \Delta s, \end{aligned} \tag{A.14}$$

where Δs is the thickness of the volume; $\Delta\omega, \Delta\omega'$ is the small solid angle at the surface s, and $\varepsilon\left(\mathrm{J}\cdot\mathrm{s}^{-1}\cdot\mathrm{m}^{-3}\cdot\mathrm{sr}^{-1}\right)$ is the source term. The meaning of left hand side (LHS) and right hand side (RHS) of Equation (A.14) is

LHS: the amount passing thorough the surface $s + \Delta s$ at time $t + \Delta t$,

First term of RHS: the amount coming in the surface s,

Second term of RHS: the attenuation term caused by the absorption and scattering,

Third term of RHS: the amount that change the direction to $\hat{\mathbf{s}}$ after entering the surface s from various angles,

Fourth term of RHS: the amount of the source in the thin slab.

If we divide both sides by $\Delta S \Delta\omega \Delta t \Delta s$, the form is given as

$$\begin{aligned}\frac{I\left(\mathbf{r}+\hat{\mathbf{s}}\Delta s, \hat{\mathbf{s}}, t+\Delta t\right)-I\left(\mathbf{r}, \hat{\mathbf{s}}, t\right)}{\Delta s} = & -\left(\mu_{\mathrm{a}}+\mu_{\mathrm{s}}\right) I\left(\mathbf{r}, \hat{\mathbf{s}}, t\right) \\ & +\mu_{\mathrm{s}} \sum_{\Delta \omega^{\prime}} I\left(\mathbf{r}, \hat{\mathbf{s}}^{\prime}, t\right) p\left(\hat{\mathbf{s}}, \hat{\mathbf{s}}^{\prime}\right)+\varepsilon\left(\mathbf{r}, \hat{\mathbf{s}}, t\right) .\end{aligned} \tag{A.15}$$

The LHS is given as

$$\begin{aligned}\frac{I\left(\mathbf{r}+\hat{\mathbf{s}}\Delta s, \hat{\mathbf{s}}, t+\Delta t\right)-I\left(\mathbf{r}, \hat{\mathbf{s}}, t\right)}{\Delta s} & =\frac{\Delta t}{\Delta s} \frac{I\left(\mathbf{r}+\hat{\mathbf{s}}\Delta s, \hat{\mathbf{s}}, t+\Delta t\right)-I\left(\mathbf{r}+\hat{\mathbf{s}}\Delta s, \hat{\mathbf{s}}, t\right)}{\Delta t} \\ & \quad+\frac{I\left(\mathbf{r}+\hat{\mathbf{s}}\Delta s, \hat{\mathbf{s}}, t\right)-I\left(\mathbf{r}, \hat{\mathbf{s}}, t\right)}{\Delta s}, \\ & \approx \frac{1}{c} \frac{\partial I\left(\mathbf{r}, \hat{\mathbf{s}}, t\right)}{\partial t}+\frac{\partial I\left(\mathbf{r}, \hat{\mathbf{s}}, t\right)}{\partial s} .\end{aligned} \tag{A.16}$$

where c is light velocity in the medium. Therefore, radiative transport equation [47], [48] is given as

$$\begin{aligned}\frac{1}{c} \frac{\partial I\left(\mathbf{r}, \hat{\mathbf{s}}, t\right)}{\partial t}+\frac{\partial I\left(\mathbf{r}, \hat{\mathbf{s}}, t\right)}{\partial s} = & -\left(\mu_{\mathrm{a}}+\mu_{\mathrm{s}}\right) I\left(\mathbf{r}, \hat{\mathbf{s}}, t\right) \\ & +\mu_{\mathrm{s}} \int_{4 \pi} I\left(\mathbf{r}, \hat{\mathbf{s}}^{\prime}, t\right) p\left(\hat{\mathbf{s}}, \hat{\mathbf{s}}^{\prime}\right) d \omega^{\prime}+\varepsilon\left(\mathbf{r}, \hat{\mathbf{s}}, t\right) ,\end{aligned} \tag{A.17}$$

where

$$\frac{\partial I\left(\mathbf{r}, \hat{\mathbf{s}}, t\right)}{\partial s}=\hat{\mathbf{s}} \cdot \operatorname{grad}\left[I\left(\mathbf{r}, \hat{\mathbf{s}}, t\right)\right]=\operatorname{div}\left[I\left(\mathbf{r}, \hat{\mathbf{s}}, t\right) \hat{\mathbf{s}}\right] . \tag{A.18}$$

A.4 P_1 approximation

Assuming that the light intensity in a highly scattering medium is almost isotropic and the energy flows in a certain direction, the specific intensity is approximated as

$$I\left(\mathbf{r}, \hat{\mathbf{s}}, t\right) \approx f_0\left(\mathbf{r}, t\right)+f_1\left(\mathbf{r}, t\right)\left(\hat{\mathbf{s}} \cdot \hat{\mathbf{s}}\right) . \tag{A.19}$$

This corresponds to the first-order term in the spherical harmonic expansion of the specific intensity. First we find f_0. Using the relation in Equations (A.40), (A.42), we have

$$\begin{aligned}\int_{4\pi} I(\mathbf{r},\hat{\mathbf{s}},t)\,d\omega &= \int_{4\pi} f_0(\mathbf{r},t)\,d\omega + \int_{4\pi} f_1(\mathbf{r},t)\,(\hat{\mathbf{s}}\cdot\hat{\mathbf{s}})\,d\omega,\\ &= 4\pi f_0(\mathbf{r},t)\,,\\ &= \phi(\mathbf{r},t)\,.\end{aligned} \tag{A.20}$$

Then we obtain $f_0 = \phi(\mathbf{r},t)/4\pi$. Next, we find f_1. Using the relation in Equations (A.42), (A.44), we have

$$\begin{aligned}\int_{4\pi} I(\mathbf{r},\hat{\mathbf{s}},t)\,(\hat{\mathbf{s}}\cdot\hat{\mathbf{s}})\,d\omega &= \int_{4\pi} f_0(\mathbf{r},t)\,(\hat{\mathbf{s}}\cdot\hat{\mathbf{s}})\,d\omega + \int_{4\pi} f_1(\mathbf{r},t)\,(\hat{\mathbf{s}}\cdot\hat{\mathbf{s}})^2\,d\omega,\\ &= \frac{4\pi}{3} f_1(\mathbf{r},t)\,,\\ &= \mathbf{J}(\mathbf{r},t)\cdot\hat{\mathbf{s}}.\end{aligned} \tag{A.21}$$

Then we obtain $f_1 = 3/4\pi\,[\mathbf{J}(\mathbf{r},t)\cdot\hat{\mathbf{s}}]$. Therefore, the specific intensity is approximated as

$$I(\mathbf{r},\hat{\mathbf{s}},t) \approx \frac{1}{4\pi}\phi(\mathbf{r},t) + \frac{3}{4\pi}\mathbf{J}(\mathbf{r},t)\cdot\hat{\mathbf{s}}, \tag{A.22}$$

and the schematic view is shown in Figure A8.

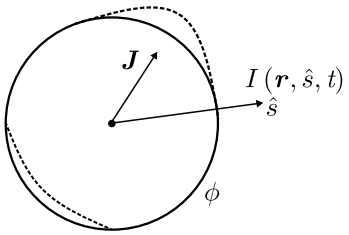

Figure A8. Schematic figure of the P_1 approximation. Solid line and dashed line denote ϕ and $\mathbf{J}$, respectively.

A.5 Fick's law

Consider the specific intensity, which travels to the direction of $\hat{\mathbf{s}}$. If we integrate Equation (A.17) over $d\omega$, after we substitute Equation (A.22) into Equation (A.17) and then multiply both sides by $\hat{\mathbf{s}}$, using the relation in Equations (A.5), (A.41), and (A.43), the form is given as

$$\begin{aligned}
\text{LHS} &= \frac{1}{c}\int_{4\pi}\left\{\frac{\partial}{\partial t}\left[\frac{1}{4\pi}\phi\left(\mathbf{r},t\right)+\frac{3}{4\pi}\mathbf{J}\left(\mathbf{r},t\right)\cdot\hat{\mathbf{s}}\right]\right\}\hat{\mathbf{s}}\,d\omega \\
&\quad+\int_{4\pi}\left(\hat{\mathbf{s}}\cdot\text{grad}\left\{\frac{1}{4\pi}\phi\left(\mathbf{r},t\right)+\frac{3}{4\pi}\left[\mathbf{J}\left(\mathbf{r},t\right)\cdot\hat{\mathbf{s}}\right]\right\}\right)\hat{\mathbf{s}}\,d\omega, \\
&= \frac{1}{c}\frac{\partial\mathbf{J}\left(\mathbf{r},t\right)}{\partial t}+\frac{1}{3}\text{grad}\,\phi\left(\mathbf{r},t\right), \\
\text{RHS} &= \int_{4\pi}\left(-\left(\mu_{\text{a}}+\mu_{\text{s}}'\right)\left\{\frac{1}{4\pi}\phi\left(\mathbf{r},t\right)+\frac{3}{4\pi}\left[\mathbf{J}\left(\mathbf{r},t\right)\cdot\hat{\mathbf{s}}\right]\right\}\hat{\mathbf{s}}\right)d\omega \\
&\quad+\int_{4\pi}\left(\mu_{\text{s}}\int_{4\pi}p\left\{\frac{1}{4\pi}\phi\left(\mathbf{r},t\right)+\frac{3}{4\pi}\left[\mathbf{J}\left(\mathbf{r},t\right)\cdot\hat{\mathbf{s}}'\right]\right\}d\omega'\right)\hat{\mathbf{s}}\,d\omega \\
&\quad+\int_{4\pi}\varepsilon\left(\mathbf{r},\hat{\mathbf{s}},t\right)\hat{\mathbf{s}}\,d\omega, \\
&= -\left(\mu_{\text{a}}+\mu_{\text{s}}\right)\mathbf{J}\left(\mathbf{r},t\right)+\mu_{\text{s}}g\mathbf{J}\left(\mathbf{r},t\right)+\int_{4\pi}\varepsilon\left(\mathbf{r},\hat{\mathbf{s}},t\right)\hat{\mathbf{s}}\,d\omega, \\
&= -\left[\mu_{\text{a}}+\left(1-g\right)\mu_{\text{s}}\right]\mathbf{J}\left(\mathbf{r},t\right)+\int_{4\pi}\varepsilon\left(\mathbf{r},\hat{\mathbf{s}},t\right)\hat{\mathbf{s}}\,d\omega, \\
&= -\left(\mu_{\text{a}}+\mu_{\text{s}}'\right)\mathbf{J}\left(\mathbf{r},t\right)+\int_{4\pi}\varepsilon\left(\mathbf{r},\hat{\mathbf{s}},t\right)\hat{\mathbf{s}}\,d\omega.
\end{aligned} \tag{A.23}$$

Hence we obtain

$$\frac{1}{c}\frac{\partial\mathbf{J}\left(\mathbf{r},t\right)}{\partial t}+\frac{1}{3}\text{grad}\,\phi\left(\mathbf{r},t\right)=-\left(\mu_{\text{a}}+\mu_{\text{s}}'\right)\mathbf{J}\left(\mathbf{r},t\right)+\int_{4\pi}\varepsilon\left(\mathbf{r},\hat{\mathbf{s}},t\right)\hat{\mathbf{s}}\,d\omega. \tag{A.24}$$

If there are not the light source in the medium, the form is

$$\frac{1}{c}\frac{\partial\mathbf{J}\left(\mathbf{r},t\right)}{\partial t}+\frac{1}{3}\text{grad}\,\phi\left(\mathbf{r},t\right)=-\left(\mu_{\text{a}}+\mu_{\text{s}}'\right)\mathbf{J}\left(\mathbf{r},t\right). \tag{A.25}$$

Assume that $\frac{\partial \mathbf{J}(\mathbf{r},t)}{\partial t}$ is small, the form is

$$\begin{aligned} \mathbf{J}(\mathbf{r},t) &= \frac{1}{3\left(\mu_{\mathrm{a}}+\mu_{\mathrm{s}}'\right)}\operatorname{grad}\phi(\mathbf{r},t), \\ &= -\kappa \operatorname{grad}\phi(\mathbf{r},t), \end{aligned} \tag{A.26}$$

where κ is diffusion coefficient defined as $\kappa = 1/\left[3\left(\mu_{\mathrm{a}}+\mu_{\mathrm{s}}'\right)\right]$. Equation (A.26) is the Fick's law.

A.6 Diffusion equation

The diffusion equation describes the isotropic near infrared light propagation. If we integrate Equation (A.17) over the solid angle, the form is given as

$$\begin{aligned} \mathrm{LHS} &= \frac{1}{c}\frac{\partial}{\partial t}\int_{4\pi} I(\mathbf{r},\hat{\mathbf{s}},t)\,d\omega + \int_{4\pi}\operatorname{div}\left[I(\mathbf{r},\hat{\mathbf{s}},t)\,\hat{\mathbf{s}}\right]d\omega, \\ &= \frac{1}{c}\frac{\partial\phi(\mathbf{r},t)}{\partial t} + \operatorname{div}\mathbf{J}(\mathbf{r},t). \\ \mathrm{RHS} &= -\left(\mu_{\mathrm{a}}+\mu_{\mathrm{s}}\right)\int_{4\pi} I(\mathbf{r},\hat{\mathbf{s}},t)\,d\omega \\ &\quad + \mu_{\mathrm{s}}\int_{4\pi}\int_{4\pi} I(\mathbf{r},\hat{\mathbf{s}}',t)\,p(\hat{\mathbf{s}},\hat{\mathbf{s}}')\,d\omega' d\omega + \int_{4\pi}\varepsilon(\mathbf{r},\hat{\mathbf{s}},t)\,d\omega, \\ &= -\left(\mu_{\mathrm{a}}+\mu_{\mathrm{s}}\right)\int_{4\pi} I(\mathbf{r},\hat{\mathbf{s}},t)\,d\omega \\ &\quad + \mu_{\mathrm{s}}\int_{4\pi} I(\mathbf{r},\hat{\mathbf{s}}',t)\left[\int_{4\pi} p(\hat{\mathbf{s}},\hat{\mathbf{s}}')\,d\omega\right]d\omega' + \int_{4\pi}\varepsilon(\mathbf{r},\hat{\mathbf{s}},t)\,d\omega, \\ &= -\mu_{\mathrm{a}}\phi(\mathbf{r},t) + q(\mathbf{r},t), \end{aligned} \tag{A.27}$$

where $q(\mathbf{r},t) = \int_{4\pi}\varepsilon(\mathbf{r},\hat{\mathbf{s}},t)\,d\omega$ is the source term. Therefore, the diffusion equation is given as

$$\frac{1}{c}\frac{\partial\phi(\mathbf{r},t)}{\partial t} + \operatorname{div}\mathbf{J}(\mathbf{r},t) = -\mu_{\mathrm{a}}\phi(\mathbf{r},t) + q(\mathbf{r},t). \tag{A.28}$$

If we substitute Fick's law in Equation (A.26) into Equation (A.28), we obtain the time-dependent diffusion equation given as

$$\left(\frac{1}{c}\frac{\partial}{\partial t} - \nabla \cdot \kappa \nabla + \mu_{\mathrm{a}}\right) \phi\left(\mathbf{r}, t\right) = q\left(\mathbf{r}, t\right), \tag{A.29}$$

where $\mathrm{div}\left(\kappa\, \mathrm{grad}\, \phi\right) = \nabla \cdot \kappa \nabla \phi$. Equation (A.29) corresponds to Equation (2.1).

A.7 Robin boundary condition

Consider the light reflection that travels from the direction of $\hat{\mathbf{s}}'$ to the direction of $\hat{\mathbf{s}}$ at the boundary $\partial\Omega$ in Figure A9.

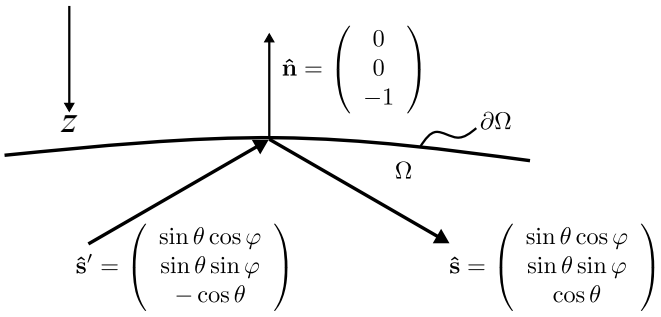

Figure A9. Schematic figure of the light reflection at a boundary.

Assuming the diffuse surface reflection at the boundary, the specific intensity is given as

$$I\left(\mathbf{r}, \hat{\mathbf{s}}, t\right) = r_{\mathrm{d}} I\left(\mathbf{r}, \hat{\mathbf{s}}', t\right) + \varepsilon_{\mathrm{b}}\left(\mathbf{r}, \hat{\mathbf{s}}, t\right), \tag{A.30}$$

where r_{d} is the internal reflectance and ε_{b} is the light source at the boundary. Integrating

Equation (A.30) over the solid angle with P_1 approximation in Equation (A.22), we have

$$\begin{aligned}\int_0^{2\pi}\int_0^{\pi/2}\left[\frac{1}{4\pi}\phi\left(\mathbf{r},t\right)+\frac{3}{4\pi}\mathbf{J}\left(\mathbf{r},t\right)\cdot\hat{\mathbf{s}}\right]\cos\theta\sin\theta\,d\theta\,d\varphi \\ = r_{\mathrm{d}}\int_0^{2\pi}\int_0^{\pi/2}\left[\frac{1}{4\pi}\phi\left(\mathbf{r},t\right)+\frac{3}{4\pi}\mathbf{J}\left(\mathbf{r},t\right)\cdot\hat{\mathbf{s}}'\right]\cos\theta\sin\theta\,d\theta\,d\varphi \\ +\int_0^{2\pi}\int_0^{\pi/2}\varepsilon_{\mathrm{b}}\left(\mathbf{r},\hat{\mathbf{s}},t\right)\cos\theta\sin\theta\,d\theta\,d\varphi.\end{aligned} \tag{A.31}$$

We can calculate the integrals as

$$\frac{1}{4}\phi\left(\mathbf{r},t\right)+\frac{J_z\left(\mathbf{r},t\right)}{2}=r_{\mathrm{d}}\left[\frac{1}{4}\phi\left(\mathbf{r},t\right)-\frac{J_z\left(\mathbf{r},t\right)}{2}\right]+\int_0^{2\pi}\int_0^{\pi/2}\varepsilon_{\mathrm{b}}\left(\mathbf{r},\hat{\mathbf{s}},t\right)\cos\theta\sin\theta\,d\theta\,d\varphi. \tag{A.32}$$

The Fick's law in Equation (A.26) is given as

$$\begin{aligned}J_z&=-\kappa\frac{\partial}{\partial z}\phi\left(\mathbf{r},t\right),\\&=\kappa\,\hat{\mathbf{n}}\cdot\nabla\phi\left(\mathbf{r},t\right).\end{aligned} \tag{A.33}$$

Then, Equation (A.32) is given as

$$\phi\left(\mathbf{r},t\right)+2\frac{1+r_{\mathrm{d}}}{1-r_{\mathrm{d}}}\kappa\,\hat{\mathbf{n}}\cdot\nabla\phi\left(\mathbf{r},t\right)=\frac{4}{1-r_{\mathrm{d}}}\int_0^{2\pi}\int_0^{\pi/2}\varepsilon_{\mathrm{b}}\left(\mathbf{r},\hat{\mathbf{s}},t\right)\cos\theta\sin\theta\,d\theta\,d\varphi. \tag{A.34}$$

Hence,

$$\phi\left(\mathbf{r},t\right)+\zeta\left(c\right)\kappa\,\hat{\mathbf{n}}\cdot\nabla\phi\left(\mathbf{r},t\right)=q\left(\mathbf{r},t\right), \tag{A.35}$$

where

$$\zeta\left(c\right)=2\frac{1+r_{\mathrm{d}}}{1-r_{\mathrm{d}}}, \tag{A.36}$$

$$q\left(\mathbf{r},t\right)=\frac{4}{1-r_{\mathrm{d}}}\int_0^{2\pi}\int_0^{\pi/2}\varepsilon_{\mathrm{b}}\left(\mathbf{r},\hat{\mathbf{s}},t\right)\cos\theta\sin\theta\,d\theta\,d\varphi, \tag{A.37}$$

where $r_{\mathrm{d}}=-1.4399n^{-2}+0.7099n^{-1}+0.6681+0.0636n$ [49]. We derived the Robin boundary condition in Equation (2.2) which corresponds to Equation (A.35) when $q\left(\mathbf{r},t\right)=0$.

A.8 Detected light

Consider the light $P_{\mathrm{D}}\left(\mathrm{J}\cdot\mathrm{s}^{-1}\right)$ entering the detection fiber in Figure A10. Let the area of the detection fiber and the NA be $S=\int dS$ and NA_{D}, respectively. Since $\mathrm{NA}_{\mathrm{D}}=n\sin\theta_{\mathrm{D}}$ and $\sin^2\theta_{\mathrm{D}}+\cos^2\theta_{\mathrm{D}}=1$, $\cos\theta_{\mathrm{D}}=\sqrt{1-\left(\mathrm{NA}_{\mathrm{D}}/n\right)^2}$, where n is refractive index in fiber.

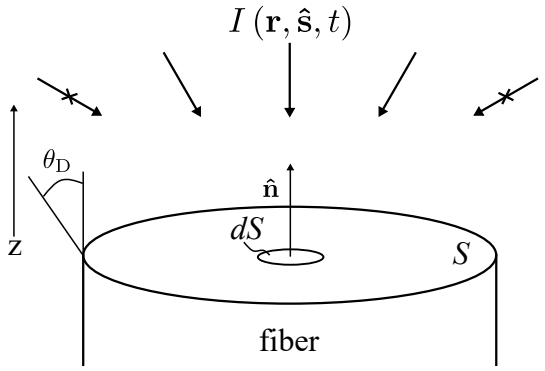

Figure A10. Schematic view of the direction fiber.

The model for the acceptance angle distribution is defined as $f_{\mathrm{D}}\left(\theta\right)$, e.g. Heavy-side step function, Gaussan function, and Hanning function. Let $dP_{\mathrm{D}}\left(\mathrm{J}\cdot\mathrm{s}\cdot\mathrm{mm}^{-2}\right)$ be the P_{D} per unit area, and using the P_1 approximation in Equation (A.22), Fick's law in Equation (A.26), and the Robin boundary condition in Equation (A.35), dP_{D} is expressed in

$$
\begin{aligned}
dP_{\mathrm{D}}\left(\mathbf{r},t\right) &= \int_{2\pi-} f_{\mathrm{D}}\left(\theta\right) I\left(\mathbf{r},\hat{\mathbf{s}},t\right) d\omega, \\
&= \int_0^{2\pi}\int_{\pi/2}^{\pi} f_{\mathrm{D}}\left(\theta\right)\left[\frac{1}{4\pi}\phi\left(\mathbf{r},t\right)+\frac{3}{4\pi}\mathbf{J}\cdot\left(-\hat{\mathbf{n}}\right)\right] d\theta\, d\varphi, \\
&= \int_0^{2\pi}\int_{\pi/2}^{\pi} f_{\mathrm{D}}\left(\theta\right)\left\{\frac{1}{4\pi}\phi\left(\mathbf{r},t\right)+\frac{3}{4\pi}\left[\kappa\,\hat{\mathbf{n}}\cdot\operatorname{grad}\phi\left(\mathbf{r},t\right)\right]\right\} d\theta\, d\varphi, \\
&= \int_0^{2\pi}\int_{\pi/2}^{\pi} f_{\mathrm{D}}\left(\theta\right)\left\{\frac{1}{4\pi}\phi\left(\mathbf{r},t\right)+\frac{3}{4\pi}\left[-\frac{1}{\zeta}\phi\left(\mathbf{r},t\right)\right]\right\} d\theta d\varphi, \\
&= \left[\left(\frac{1}{2}-\frac{3}{2\zeta}\right)\int_{\pi/2}^{\pi} f_{\mathrm{D}}\left(\theta\right) d\theta\right]\phi\left(\mathbf{r},t\right), \\
&= -\left[\left(\frac{1}{2}-\frac{3}{2\zeta}\right)\int_{\pi/2}^{\pi} f_{\mathrm{D}}\left(\theta\right) d\theta\right]\zeta\kappa\,\hat{\mathbf{n}}\cdot\nabla\phi\left(\mathbf{r},t\right).
\end{aligned}
\tag{A.38}
$$

If the area of the fiber is S, then P_{D} is given as

$$P_{\mathrm{D}}(t) = -\left[\left(\frac{1}{2} - \frac{3}{2\zeta}\right)\int_{\pi/2}^{\pi} f_{\mathrm{D}}(\theta)\, d\theta\right]\zeta \int_{\mathrm{S}} \kappa\, \hat{\mathbf{n}} \cdot \nabla\phi(\mathbf{r}, t)\, dS. \tag{A.39}$$

Since the measurement results of TRS-80 contains unknown constants from the measurement setup, it cannot be compared with the absolute value of P_{D} . Therefore, the Equation (A.38) without the term $\left[\left(\frac{1}{2} - \frac{3}{2\zeta}\right)\int_{\pi/2}^{\pi} f_{\mathrm{D}}(\theta)\, d\theta\right]\zeta$ is Equation (2.3).

A.9 Formula

The unit direction vector represents $\hat{\mathbf{s}}$ in Figure A11. The arbitrary vector represents $\mathbf{a}$ and $\mathbf{b}$. The following relationships hold.

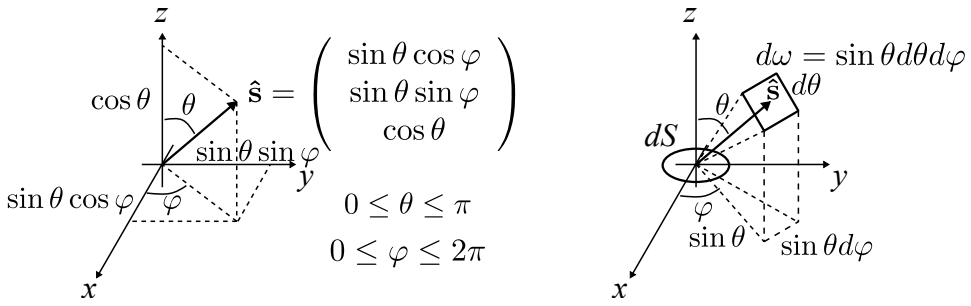

Figure A11. Schematic view of the unit direction vector and the solid angle.

$$\int_{4\pi} d\omega = \int_0^{2\pi}\int_0^{\pi} \sin\theta\, d\theta\, d\varphi = 4\pi. \tag{A.40}$$

$$\int_{4\pi} \hat{\mathbf{s}}\, d\omega = \int_0^{2\pi}\int_0^{\pi} \hat{\mathbf{s}} \sin\theta\, d\theta\, d\varphi = 0. \tag{A.41}$$

$$\int_{4\pi} \hat{\mathbf{s}} \cdot \mathbf{a}\, d\omega = \int_0^{2\pi}\int_0^{\pi} \hat{\mathbf{s}} \cdot \mathbf{a} \sin\theta\, d\theta\, d\varphi = 0. \tag{A.42}$$

$$\int_{4\pi} (\hat{\mathbf{s}} \cdot \mathbf{a})\, \hat{\mathbf{s}}\, d\omega = \int_0^{2\pi}\int_0^{\pi} (\hat{\mathbf{s}} \cdot \mathbf{a})\, \hat{\mathbf{s}} \sin\theta\, d\theta\, d\varphi = \frac{4}{3}\pi\mathbf{a}. \tag{A.43}$$

$$\int_{4\pi} (\hat{\mathbf{s}} \cdot \mathbf{a})\, (\hat{\mathbf{s}} \cdot \mathbf{b})\, d\omega = \int_0^{2\pi}\int_0^{\pi} (\hat{\mathbf{s}} \cdot \mathbf{a})\, (\hat{\mathbf{s}} \cdot \mathbf{b}) \sin\theta\, d\theta\, d\varphi = \frac{4}{3}\pi\mathbf{a} \cdot \mathbf{b}. \tag{A.44}$$

Bibliography

[1] L. Wartofsky, "Increasing world incidence of thyroid cancer: Increased detection or higher radiation exposure?" *Hormones*, vol. 9, no. 2, pp. 103–108, 2010. DOI: 10.14310/horm.2002.1260.

[2] Y. J. Deng, H. T. Li, M. Wang, N. Li, T. Tian, Y. Wu, P. Xu, S. Yang, Z. Zhai, L. H. Zhou, Q. Hao, D. L. Song, T. B. Jin, J. Lyu, and Z. J. Dai, "Global Burden of Thyroid Cancer From 1990 to 2017," *JAMA network open*, vol. 3, no. 6, e208759, 2020. DOI: 10.1001/jamanetworkopen.2020.8759.

[3] L. Davies and H. G. Welch, "Increasing Incidence of Thyroid Cancer in the United States, 1973-2002," *JAMA*, vol. 295, no. 18, p. 2164, 2006. DOI: 10.1001/jama.295.18.2164.

[4] J. P. Shah, "Thyroid Carcinoma: Epidemiology, histology, and diagnosis," *Clinical Advances in Hematology and Oncology*, vol. 13, no. 4, pp. 3–6, 2015.

[5] Z. W. Baloch and V. A. LiVolsi, "Follicular-patterned lesions of the thyroid: The bane of the pathologist," *American Journal of Clinical Pathology*, vol. 117, no. 1, pp. 143–150, 2002. DOI: 10.1309/8VL9-ECXY-NVMX-2RQF.

[6] N. A. Cipriani, S. Nagar, S. P. Kaplan, M. G. White, T. Antic, P. M. Sadow, B. Aschebrook-Kilfoy, P. Angelos, E. L. Kaplan, and R. H. Grogan, "Follicular Thyroid Carcinoma: How Have Histologic Diagnoses Changed in the Last Half-Century and What Are the Prognostic Implications?" *Thyroid*, vol. 25, no. 11, pp. 1209–1216, 2015. DOI: 10.1089/thy.2015.0297.

[7] A. D. King, "Imaging for staging and management of thyroid cancer," *Cancer Imaging*, vol. 8, no. 1, pp. 57–69, 2008. DOI: 10.1102/1470-7330.2008.0007.

[8] C. Marcus, P. W. Whitworth, D. S. Surasi, S. I. Pai, and R. M. Subramaniam, "PET/CT in the management of thyroid cancers," *American Journal of Roentgenology*, vol. 202, no. 6, pp. 1316–1329, 2014. DOI: 10.2214/AJR.13.11673.

[9] M. V. Sprindzuk, "Angiogenesis in Malignant Thyroid Tumors," *World Journal of Oncology*, vol. 1, no. 6, pp. 221–231, 2010. DOI: 10.4021/wjon263e.

[10] K. Cho Mar, T. Eimoto, H. Tateyama, Y. Arai, Y. Fujiyoshi, and M. Hamaguchi, "Expression of matrix metalloproteinases in benign and malignant follicular thyroid lesions," *Histopathology*, vol. 48, no. 3, pp. 286–294, 2006. DOI: 10.1111/j.1365-2559.2005.02325.x.

[11] N. Burrows, J. Resch, R. L. Cowen, R. Von Wasielewski, C. Hoang-Vu, C. M. West, K. J. Williams, and G. Brabant, "Expression of hypoxia-inducible factor 1α in thyroid carcinomas," *Endocrine-Related Cancer*, vol. 17, no. 1, pp. 61–72, 2010. DOI: 10.1677/ERC-08-0251.

[12] M. Yang, L. Zhao, X. He, N. Su, C. Zhao, H. Tang, T. Hong, W. Li, F. Yang, L. Lin, B. Zhang, R. Zhang, Y. Jiang, and C. Li, "Photoacoustic/ultrasound dual imaging of human thyroid cancers: an initial clinical study," *Biomedical Optics Express*, vol. 8, no. 7, p. 3449, 2017. DOI: 10.1364/boe.8.003449.

[13] J. Levi, S. R. Kothapalli, S. Bohndiek, J. K. Yoon, A. Dragulescu-Andrasi, C. Nielsen, A. Tisma, S. Bodapati, G. Gowrishankar, X. Yan, C. Chan, D. Starcevic, and S. S. Gambhir, "Molecular photoacoustic imaging of follicular thyroid carcinoma," *Clinical Cancer Research*, vol. 19, no. 6, pp. 1494–1502, 2013. DOI: 10.1158/1078-0432.CCR-12-3061.

[14] C. Lindner, M. Mora, P. Farzam, M. Squarcia, J. Johansson, U. M. Weigel, I. Halperin, F. A. Hanzu, and T. Durduran, "Diffuse optical characterization of the healthy human thyroid tissue and two pathological case studies," *PLoS ONE*, vol. 11, no. 1, pp. 1–22, 2016. DOI: 10.1371/journal.pone.0147851.

[15] K. Mahkamova, N. Latar, S. Aspinall, and A. Meeson, "Hypoxia Increases Thyroid Cancer Stem Cell-Enriched Side Population," *World Journal of Surgery*, vol. 42, no. 2, pp. 350–357, 2018. DOI: 10.1007/s00268-017-4331-x.

[16] S. R. Arridge, "Optical tomography in medical imaging," *Inverse Problems*, vol. 15, no. 2, R41–R93, 1999. DOI: 10.1088/0266-5611/15/2/022.

[17] Y. Hoshi, O. Hazeki, Y. Kakihana, and M. Tamura, "Redox behavior of cytochrome oxidase in the rat brain measured by near- infrared spectroscopy," *Journal of Applied Physiology*, vol. 83, no. 6, pp. 1842–1848, 1997. DOI: 10.1152/jappl.1997.83.6.1842.

[18] Y. Hoshi and Y. Yamada, "Overview of diffuse optical tomography and its clinical applications," *Journal of Biomedical Optics*, vol. 21, no. 9, p. 091 312, 2016. DOI: 10.1117/1.jbo.21.9.091312.

[19] N. Yoshizawa, Y. Ueda, T. Mimura, E. Ohmae, K. Yoshimoto, H. Wada, H. Ogura, and H. Sakahara, "Factors affecting measurement of optic parameters by time-resolved near-infrared spectroscopy in breast cancer," *Journal of Biomedical Optics*, vol. 23, no. 02, p. 1, 2018. DOI: 10.1117/1.JBO.23.2.026010.

[20] S. R. Arridge and M. Schweiger, "Direct calculation of the moments of the distribution of photon time of flight in tissue with a finite-element method.," *Applied optics*, vol. 34, no. 15, pp. 2683–2687, 1995. DOI: 10.1364/AO.34.002683.

[21] E. M. Hillman, J. C. Hebden, F. E. Schmidt, S. R. Arridge, M. Schweiger, H. Dehghani, and D. T. Delpy, "Calibration techniques and datatype extraction for time-resolved optical tomography," *Review of Scientific Instruments*, vol. 71, no. 9, pp. 3415–3427, 2000. DOI: 10.1063/1.1287748.

[22] N. Jorge and S. Wright, *Numerical Optimization*, 2nd ed., ser. Springer Series in Operations Research and Financial Engineering. Springer New York, 2006, p. 664. DOI: 10.1007/978-0-387-40065-5.

[23] S. R. Arridge and M. Schweiger, "A gradient-based optimisation scheme for optical tomography," *Optics Express*, vol. 2, no. 6, p. 213, 1998. DOI: 10.1364/OE.2.000213.

[24] M. Schweiger and S. Arridge, "The Toast++ software suite for forward and inverse modeling in optical tomography," *Journal of Biomedical Optics*, vol. 19, no. 4, p. 040 801, 2014. DOI: 10.1117/1.jbo.19.4.040801.

[25] M. L. Vernon, J. Fréchette, Y. Painchaud, S. Caron, and P. Beaudry, "Fabrication and characterization of a solid polyurethane phantom for optical imaging through scattering media," *Applied Optics*, vol. 38, no. 19, pp. 4247–4251, 1999. DOI: 10.1364/AO.38.004247.

[26] J.-P. Bouchard, I. Veilleux, R. Jedidi, I. Noiseux, M. Fortin, and O. Mermut, "Reference optical phantoms for diffuse optical spectroscopy. part 1 – error analysis of a time resolved transmittance characterization method," *Optics Express*, vol. 18, no. 11, pp. 11 495–11 507, 2010. DOI: 10.1364/OE.18.011495.

[27] C. Geuzaine and J. F. Remacle, "Gmsh: A 3-D finite element mesh generator with built-in pre- and post-processing facilities," *International Journal for Numerical Methods in Engineering*, vol. 79, no. 11, pp. 1309–1331, 2009. DOI: 10.1002/nme.2579.

[28] F. Gao, H. Zhao, and Y. Yamada, "Improvement of image quality in diffuse optical tomography by use of full time-resolved data," *Applied Optics*, vol. 41, no. 4, pp. 778–791, 2002. DOI: 10.1364/AO.41.000778.

[29] A. Fedorov, R. Beichel, J. Kalpathy-Cramer, J. Finet, J.-C. Fillion-Robin, S. Pujol, C. Bauer, D. Jennings, F. Fennessy, M. Sonka, J. Buatti, S. Aylward, J. V. Miller, S. Pieper, and R. Kikinis, "3d slicer as an image computing platform for the quantitative imaging network," *Magnetic Resonance Imaging*, vol. 30, no. 9, pp. 1323–1341, 2012. DOI: https://doi.org/10.1016/j.mri.2012.05.001.

[30] H. Dehghani, S. R. Arridge, M. Schweiger, and D. T. Delpy, "Optical tomography in the presence of void regions," *Journal of the Optical Society of America A*, vol. 17, no. 9, p. 1659, 2000. DOI: 10.1364/josaa.17.001659.

[31] J. Riley, H. Dehghani, M. Schweiger, S. R. Arridge, J. Ripoll, and M. Nieto-Vesperinas, "3D optical tomography in the presence of void regions," *Optics Express*, vol. 7, no. 13, p. 462, 2000. DOI: 10.1364/oe.7.000462.

[32] H. Fujii, Y. Yamada, K. Kobayashi, M. Watanabe, and Y. Hoshi, "Modeling of light propagation in the human neck for diagnoses of thyroid cancers by diffuse optical tomography," *International Journal for Numerical Methods in Biomedical Engineering*, vol. 33, no. 5, pp. 1–12, 2017. DOI: 10.1002/cnm.2826.

[33] S. Konugolu Venkata Sekar, A. Farina, A. Dalla Mora, C. Lindner, M. Pagliazzi, M. Mora, G. Aranda, H. Dehghani, T. Durduran, P. Taroni, and A. Pifferi, "Broadband (550–1350 nm) diffuse optical characterization of thyroid chromophores," *Scientific Reports*, vol. 8, no. 1, p. 10 015, 2018. DOI: 10.1038/s41598-018-27684-8.

[34] D. R. White, H. Q. Woodard, and S. M. Hammond, "Average soft-tissue and bone models for use in radiation dosimetry," *The British Journal of Radiology*, vol. 60, no. 717, pp. 907–913, 1987. DOI: 10.1259/0007-1285-60-717-907.

[35] S. Matcher, C. Elwell, C. Cooper, M. Cope, and D. Delpy, "Performance comparison of several published tissue near-infrared spectroscopy algorithms," *Analytical biochemistry*, vol. 227, no. 1, pp. 54–68, 1995. DOI: 10.1006/abio.1995.1252.

[36] L. Kou, D. Labrie, and P. Chylek, "Refractive indices of water and ice in the 0.65- to 2.5-μm spectral range," *Applied Optics*, vol. 32, no. 19, pp. 3531–3540, 1993. DOI: 10.1364/AO.32.003531.

[37] B. W. Pogue, T. O. McBride, J. Prewitt, U. L. Österberg, and K. D. Paulsen, "Spatially variant regularization improves diffuse optical tomography," *Applied Optics*, vol. 38, no. 13, p. 2950, 1999. DOI: 10.1364/ao.38.002950.

[38] A. Corlu, R. Choe, T. Durduran, K. Lee, M. Schweiger, S. R. Arridge, E. M. C. Hillman, and A. G. Yodh, "Diffuse optical tomography with spectral constraints and wavelength optimization," *Applied Optics*, vol. 44, no. 11, p. 2082, 2005. DOI: 10.1364/AO.44.002082.

[39] F. Gao, P. Poulet, and Y. Yamada, "Simultaneous mapping of absorption and scattering coefficients from a three-dimensional model of time-resolved optical tomography," *Applied Optics*, vol. 39, no. 31, p. 5898, 2000. DOI: 10.1364/ao.39.005898.

[40] M. Schweiger and S. R. Arridge, "Application of temporal filters to time resolved data in optical tomography," *Physics in Medicine and Biology*, vol. 44, no. 7, pp. 1699–1717, 1999. DOI: 10.1088/0031-9155/44/7/310.

[41] P. Poudel, C. Hansen, J. Sprung, and M. Friebe, "3d segmentation of thyroid ultrasound images using active contours," *Current Directions in Biomedical Engineering*, vol. 2, no. 1, pp. 467–470, 2016. DOI: doi:10.1515/cdbme-2016-0103.

[42] P. Poudel, A. Illanes, D. Sheet, and M. Friebe, "Evaluation of commonly used algorithms for thyroid ultrasound images segmentation and improvement using machine learning approaches," *Journal of Healthcare Engineering*, vol. 2018, 2018. DOI: 10.1155/2018/8087624.

[43] B. Preim, "Clinical Impact of the Tumor Therapy Manager," *VISWeek '10*, no. January, 2010.

[44] B. Thiering, J. Nagarajah, and H. G. Lipinski, "Spatial reconstruction of human thyroid based on ultrasound and ct image data fusion," vol. 58, no. SI-1-Track-L, 2013. DOI: doi:10.1515/bmt-2013-4284.

[45] R. A. Ciora, B. Neamţu, C. Şofariu, C. Dospinescu, A. Barbu, and D. D. Banciu, "A simple method for 3d thyroid reconstruction from 2d ultrasound slices," in *2019 E-Health and Bioengineering Conference (EHB)*, 2019, pp. 1–4. DOI: 10.1109/EHB47216.2019.8970083.

[46] S. L. Jacques, "Optical properties of biological tissues: A review," *Physics in Medicine and Biology*, vol. 58, no. 11, R37–R61, 2013. DOI: 10.1088/0031-9155/58/11/r37.

[47] S. Chandrasekhar, *Radiative Transfer*, 1st ed. Dover Publications, Inc, 1950. DOI: https://doi.org/10.1007/978-3-319-14929-5.

[48] J. R. Lorenzo, *Principles of Diffuse Light Propagation*. WORLD SCIENTIFIC, 2012. DOI: 10.1142/7609.

[49] W. G. Egan and T. W. Hilgeman, *Optical Properties of Inhomogeneous Materials*. Academic Press, 1979. DOI: https://doi.org/10.1016/B978-0-12-232650-9.50013-8.

List of Publications

Journal papers

T. Mimura, S. Okawa, H. Kawaguchi, Y. Tanikawa, and Y. Hoshi, "Imaging the human thyroid using three-dimensional diffuse optical tomography: a preliminary study," *Applied Sciences*, vol. 11, no. 4, pp. 2076-3417, 2021.

E. Ohmae, N. Yoshizawa, K. Yoshimoto, M. Hayashi, H. Wada, **T. Mimura**, Y. Asano, H. Ogura, Y. Yamashita, H. Sakahara, and Y. Ueda, "Comparison of lipid and water contents by time-domain diffuse optical spectroscopy and dual-energy computed tomography in breast cancer patients," *Applied Sciences*, vol. 9, no. 7, pp. 2076-3417, 2019.

Y. Asano, N. Yoshizawa, Y. Ueda, K. Yoshimoto, **T. Mimura**, E. Ohmae, H. Wada,S. Ueda, T. Saeki, H. Ogura, N. Shiiya, and H. Sakahara, "Correction by the skin-to-chest wall distance in near-infrared spectroscopy and assessment of breast cancer responses to neoadjuvant chemotherapy," *Optical Review*, vol. 26, no. 1, pp. 111–117, 2019.

M. Hayashi, N. Yoshizawa, Y. Ueda, **T. Mimura**, E. Ohmae, K. Yoshimoto, H. Wada,H. Nasu, H. Ogura, and H. Sakahara, "Effect of Source-detector distance on the measurement of hemoglobin using near-infrared spectroscopy in breast cancer," *Technology in Cancer Research & Treatment*, vol. 18, p. 153303381983041, 2019.

N. Yoshizawa, Y. Ueda, **T. Mimura**, E. Ohmae, K. Yoshimoto, H. Wada, H. Ogura, and H. Sakahara, "Factors affecting measurement of optic parameters by time-resolved near-infrared spectroscopy in breast cancer," *Journal of Biomedical Optics*, vol. 23,no. 2, pp. 1-6, 2018.

E. Ohmae, N. Yoshizawa, K. Yoshimoto, M. Hayashi, H. Wada, **T. Mimura**, H. Suzuki,S. Homma, N. Suzuki, H. Ogura, H. Nasu, H. Sakahara, Y. Yamashita, and Y. Ueda, "Sta-

ble tissue-simulating phantoms with various water and lipid contents for diffuse optical spectroscopy," *Biomedical Optics Express*, vol. 9, no. 11, pp. 5792-5808, 2018.

Conference proceedings

K. Yoshimoto, H. Wada, N. Yoshizawa, H. Ogura, E. Ohmae, H. Suzuki, S. Homma, **T. Mimura**, N. Suzuki, Y. Asano, S. Goshima, and Y. Ueda, "Time-domain reflectance diffuse optical tomography for imaging breast cancer," in *Optical Tomography and Spectroscopy of Tissue XIV*, International Society for Optics and Photonics, vol. 11639, SPIE, 2021, pp. 165–170.

S. Okawa, **T. Mimura**, H. Fujii, H. Kawaguchi, Y. Tanikawa, M. Machida, E. Okada,and Y. Hoshi, "Time-domain diffuse optical tomography with lp sparsity regularization for thyroid cancer imaging," in *Diffuse Optical Spectroscopy and Imaging VII*, International Society for Optics and Photonics, vol. 11074, SPIE, 2019, pp. 17–20.

H. Suzuki, E. Ohmae, K. Yoshimoto, H. Wada, S. Homma, N. Suzuki, **T. Mimura**, Y.Yamashita, and Y. Ueda, "Water and lipid contents measured at various parts of the human body with a six-wavelength time-resolved spectroscopy system," in *Optical Tomography and Spectroscopy of Tissue XIII*, International Society for Optics andPhotonics, vol. 10874, SPIE, 2019, pp. 37–42.

E. Ohmae, H. Suzuki, K. Yoshimoto, S. Homma, N. Suzuki, H. Wada, **T. Mimura**, N. Yoshizawa, H. Ogura, H. Nasu, H. Sakahara, Y. Yamashita, and Y. Ueda, "Evaluation of phantoms with various water and lipid contents by using a six-wavelength time-resolved spectroscopy system," in *Biophotonics Congress: Biomedical Optics Congress 2018 (Microscopy/Translational/Brain/OTS)*, Optical Society of America, 2018, JTu3A.43.

K. Yoshimoto, E. Ohmae, D. Yamashita, H. Suzuki, S. Homma, **T. Mimura**, H.Wada, T. Suzuki, N. Yoshizawa, H. Nasu, H. Ogura, H. Sakahara, Y. Yamashita, andY. Ueda, "Development of time-resolved reflectance diffuse optical tomography for breast cancer monitoring," in *Optical Tomography and Spectroscopy of Tissue XII*, International Society for Optics and Photonics, vol. 10059, SPIE, 2017, pp. 41–50.

Acknowledgements

This three years for working on my PhD have been very wonderful time, and I have learned and grown a lot, both intellectually and personally. I would like to thank many people who supported me and provided me with many opportunities during this time.

I would like to thank my supervisors Prof. Yoko Hoshi for her patient support, encouragement and guidance throughout this PhD. I am indebted to Prof. Yoko Hoshi for originally inspiring me to pursue a career in Medical Photonics. I am also indebted to Prof. Tetsumei Urano and Dr Masatsugu Niwayama, who discussed me about medical and photonics insights.

I would also like to thank Dr Tsutomu Hara, Dr Yutaka Yamashita, and Dr Yukio Ueda, who gave me a great opportunity for this three years to learn medical science and pursue my PhD while working on Hamamatsu Photonics K.K.

I would also particularly like to thank Dr Manabu Machida, who give me much time in the discussions and the many resulted idea are introduced in this thesis. I was challenged and motivated by his encouragement and determination to strive for perfection.

This thesis would not have been possible without the contribution of the discussions and the fabrication of the holder by Dr Yukari Tanikawa, Dr Hiroshi Kawaguchi, and Dr Shinpei Okawa.

I would like to thank members of seventh research group in central research laboratory in Hamamatsu Photonics K.K., without their generosity, kindness, and the discussions, I

can not have sufficient time to pursue my PhD.

I must express my gratitude to Dr Samuel Powell, Prof. Martin Schweiger and Prof. Simon Arridge for their previous works and maintaining the TOAST++ image reconstruction algorithm.

I would like to thank my dear wife, without her unwavering support, I would have been impossible to pursue my PhD. She also supported my family during my PhD. Along with her, I would like to thank my daughter and two sons. I got peace and much energy from them. I also thank my mother and father, who provided me with every opportunity.

This work was generously supported by Japan Agency for Medical Research and Development. Additional funding was contributed by Hamamatsu University School of Medicine and the Uehara Memorial Foundation.